



3 1293 01046 8597

This is to certify that the

dissertation entitled

Transport and Dielectric Breakdown in Composites
with Complex Inclusion Microstructures.

presented by

Heungjin Bak

has been accepted towards fulfillment
of the requirements for

Ph.D. degree in Physics / Astronomy

Peter A. Schroeder

Major professor

Date Sep. 7 1994

**LIBRARY
Michigan State
University**

PLACE IN RETURN BOX to remove this checkout from your record.
TO AVOID FINES return on or before date due.

DATE DUE	DATE DUE	DATE DUE
_____	_____	_____
_____	_____	_____
_____	_____	_____
_____	_____	_____
_____	_____	_____
_____	_____	_____
_____	_____	_____

MSU is An Affirmative Action/Equal Opportunity Institution

ct/circ/datedue.pm3-p.1

Transport and Dielectric Breakdown in Composites with Complex Inclusion Microstructures

By

Heungjin Bak

A DISSERTATION

Submitted to

Michigan State University

in partial fulfillment of the requirements

for the degree of

DOCTOR OF PHILOSOPHY

Department of Physics and Astronomy

1994

ABSTRACT

Transport and Dielectric Breakdown in Composites with Complex Inclusion Microstructures

by
Heungjin Bak

A series of experiments have been performed on the dielectric and breakdown properties of random continuum composites. The experiments are divided into two categories: those performed on samples with static interfaces(e.g. steel balls in paraffin wax) and those with dynamic interface(e.g. polystyrene microspheres in suspension). The critical parameter for the stainless steel spheres in wax departed considerably from the predicted parameter. Since the theory is based on the intrinsic conductivity of the metal being infinite, the departures for the stainless steel spheres were ascribed to this cause. The higher conductivity Cu "spheres" gave better values, but the critical concentration of the spheres was much lower than anticipated, possibly due to large departures from sphericity for the Cu "spheres".

The dielectric breakdown measurements were performed for similar samples stainless steel particles in wax and compared with theory. The effect of a conducting defect is more drastic in dielectric breakdown than in capacitance. The statistics describing the dielectric and breakdown data are different. For the breakdown data the modified Gumbel distribution and the Weibull distribution have been suggested as possible distributions. 300 failure tests indicated that at least two breakdown mechanisms were present, and that the part ascribed to intrinsic breakdown is better described by the modified Gumbel distribution.

Attempts were made to measure the dielectric properties of colloidal suspensions of polystyrene spheres. Several methods designed to reduce or correct for electrode polarization were performed. In a study of the effect of electrode material, we found that bare Pt electrodes were superior to conventionally recommended Pt black and sand blasted Pt electrodes.

The experimental results for the real part of the dielectric constant still exhibited electrode polarization effects below 1 KHz. Other serious problems included time variation and the separation of AC and DC conductivities necessary for the extraction of the imaginary part of the dielectric constant.

The experimental results were compared with the theory developed by Sen and Chew. Large discrepancies in the real part of the dielectric constant seemingly stemmed from the electrode polarization effect. The results for the imaginary part yielded characteristic frequencies proportional to the inverse square of the particle radius as expected from theory.

To my parents

ACKNOWLEDGEMENTS

I wish to thank professor Peter Schroeder for his support and patient guidance throughout my thesis work. Without his help it would not have been possible to finish this thesis.

I would like to thank professors J. Cowen, P. Duxbury, T. Pinnavaia and J. Pumphin for their service as my doctoral guidance committee. I am thankful to Dr. B. Cukier for his commitment as a substitute for P. Duxbury during his sabbatical leave.

I am also thankful to Dr. M. Dubson for letting me use HP Impedance Analyzer. I am also indebted to R. Loloee, R. Joy and P. Kaviratna for their help and advice.

I would also like to thank Dr. A. Rudin, the Professor of Chemistry at University of Waterloo, Canada and his graduate student, G. Shouldice, for providing the polystyrene samples.

My special thank goes to my parents for their prayer and support. Most of all I would like to thank my wife, Junghee, and daughter, Jihae, for their love, prayer and encouragement.

Contents

Motivation.....	1
1. Capacitance.....	4
1.1 Introduction.....	4
1.2 Theory.....	4
1.2.1 Low loading limit.....	6
1.2.2 High loading limit.....	6
1.2.3 Frequency dependence.....	11
1.3 Experiments and discussion.....	12
2. Dielectric breakdown.....	29
2.1 Introduction.....	29
2.2 Theory.....	29
2.3 Experiments and discussion.....	32
3. Comparison of capacitance and dielectric breakdown.....	38
3.1 Introduction.....	38
3.2 Local field distribution.....	38
3.3 Statistics.....	41
4. Dielectric properties of colloidal suspensions	
- Theoretical reviews.....	47
4.1 Introduction.....	47

4.2 Complex permittivity.....	47
4.2a Debye equations.....	49
4.3 Maxwell-Wagner theory.....	50
4.4 Thin double layer approximation.....	57
 5. Dielectric properties of colloidal suspensions	
- Experimental attempts.....	64
5.1 Introduction.....	64
5.2 Electrode polarization.....	64
5.3 Review of other experiments.....	72
5.4 Experimental setup.....	76
5.4.1 Capacitance cell.....	76
5.4.2 Electrodes.....	77
5.4.3 Microsphere samples.....	79
5.4.4 Measurement setup.....	82
5.5 Experiments and discussion.....	82
5.5.1 Long cell.....	82
5.5.1a Effect of electrode material.....	84
5.5.2 Small cell.....	90
5.5.2a Results using Pt black electrode.....	95
5.5.2b Variation of measurement with time.....	99
5.5.2c Sand blasted electrode.....	105
5.5.2d Results with Pt electrode.....	111
 6. Summary.....	121
6.1 Capacitance and dielectric breakdown.....	121
6.2 Dielectric properties of polystyrene latex suspensions.....	122

Appendix 1: Derivation of Eqs. (2.2.1) and (2.2.2).....	127
Appendix 2: Derivation of equations in Sec.4.4.....	132

List of Tables

1.1 Conversion table of each equivalent circuit mode.....	18
5.1 Comparison of the previous experimental results.....	76
5.2 The quality factor of 1 mM KCl.....	89
5.3 Comparison of conductivity values obtained from direct measurement(Gm) and from using analysis(G).....	96

List of Figures

1.1	Two-dimensional examples of model microstructures: (a) a regular array of metal particles in a continuum background; (b) a site percolation model composed of metal spheres and insulating spheres and (c) a random configuration of metal particles in a continuum background.....	5
1.2	(a) Cross section of a cubic array of conducting spheres of radius a with distance c between centers. The dotted line is the cross section of a cube of side c . (b) Enlarged view of the gap between a plane midway between two spheres, and one of the spheres.....	8
1.3	Critical behaviors of Eqs.(1.2.12)(\square) and (1.2.13)(Δ). Using $f_*=0.6$	10
1.4	Cell used to make paraffin disks.....	14
1.5	(a) and (b) Optical photographs of cross sections of metal loaded paraffin discs. (d) Copper particles. (d) Stainless steel particles.....	15
1.6	(a) Principle of guard ring to assure uniform sample field. (b) Block diagram of HP4192A impedance analyzer.....	16
1.7	Capacitances of paraffin wax containing (a) copper particles and (b) stainless steel particles against their volume concentrations. Error bars indicate minimum and maximum values.....	19
1.8	The capacitance ratio, $C(0)/C(f)$ as a function of the volume fraction of metal inclusions. Experimental values using stainless steel(\square) and using copper(\circ). Numerical simulations(+) calculated using a simple cubic lattice.....	21
1.9	Test of Eq.(1.3.3) for large f . If the Eq.(1.3.3) is correct the data plotted	

	here should be linear. f_s 's used are 0.65 for stainless steel(\square) and 0.41 for copper(Δ). The solid lines are a guide to the eye.....	22
1.10	If Eq.(1.3.3) is correct the data plotted here should be linear. The best fitting parameters are $f_s=0.65$ and $\alpha=-0.15$ for stainless steel(\square), and $f_s=0.41$ and $\alpha=-0.86$ for copper(Δ). The solid lines are guide to the eye...	23
1.11	(a) Real part and (b) imaginary part of the dielectric constant of paraffin wax containing stainless particles. Numbers in the legend are the concentrations of stainless particles.....	25
1.12	The frequency dependence of stainless steel particles.....	26
2.1	A field-enhancing cluster of conducting bonds(—) in a background of insulating bonds(----).....	31
2.2	A schematic digram of breakdown experiment.....	33
2.3	(a) The dielectric breakdown field ratio of experimental results on samples of paraffin wax containing stainless steel balls. (b) The dielectric breakdown field ratio calculated using the square lattice dielectric breakdown model[2]. Each point is an average over at least 50 configurations of 100 x 100 lattices. Solid lines are a guide to the eye.....	35
2.4	A test of Eq.(2.2.5) with $\alpha=3/2(+)$ and $\alpha=1(\square)$. (a) Experimental data same as that in Fig.2.3(a). (b) Numerical simulation data same as that in Fig.2.3(b). The full curves are a guide to the eyes.	36
3.1	The capacitance ratio $C(0)/C(f)$, (\square and Δ) and the dielectric breakdown field ratio $E_b(f)/E_b(f)$, (+). (a) The results calculated using the square lattice dielectric breakdown model. Each point is an average over at least 50 configurations of 100 x 100 lattices[3]. (b) Experimental results on samples of paraffin wax containing stainless steel balls(\square) and copper particles(Δ). The full curves are a guide to the eye.....	40
3.2	A cumulative probability of failure of paraffin discs against breakdown	

voltage.....	43
3.3 Tests of breakdown statistics. (a) If the modified Gumbel distribution (Eq.(3.3.3)) is correct the data as plotted here should be linear; (b) If the Weibull distribution (Eq.(3.3.2)) is correct this way of plotting the data should yield a linear relationship. The full curves are a guide to the eye. The data are from 300 samples of pure paraffin(0.3mm thick).....	44
4.1 Real (ϵ') and imaginary (ϵ'') parts of the complex dielectric constant of a suspension of polystyrene particles as a function of frequency: particle diameter 0.188 μm , particle concentration 30%.....	48
4.2 (a) The model of a binary heterogeneous system. (b) The equivalent circuit of the system.....	51
4.3 Real part(\square) and imaginary part(Δ) of dielectric behavior of Eq.(4.3.4). In this plot $\epsilon_a = 80\epsilon_0$, $\epsilon_b = 2\epsilon_0$, $k_a = 1 \times 10^{-5}$, $k_b = 1.5 \times 10^{-9}$, and $f=3/500$ are used.....	53
4.4 Wagner's model for a dilute suspension of spherical particles.....	55
4.5 (a) A negatively charged particle in ionic solution acquires positively charged counterions in the absence of an external electric field. (b) In the presence of an external electric field E_0 the charge distribution in the double layer changes and polarization charges develop within the particle...	58
4.6 Dielectric behavior of Eq.(4.4.9).....	62
5.1 Idealized view of the polarization due to dipoles and ions: (a) unpolarized; (b) orientation and conduction begins; (c) fully polarized. In actual materials, both processes can occur simultaneously.....	66
5.2 The apparent dielectric constants of several liquids which are different in conductivity.....	67
5.3 (a) Equivalent circuit of dielectric cell. (b) Equivalent circuit of the total measured admittance.....	68

5.4	Cylindrical teflon sample cell S with metallic coaxial shield M.....	70
5.5	Components of the apparent dielectric constant as function of electrode distance.....	73
5.6	Dielectric properties(real part(\square) and imaginary part(Δ)) from (a) Springer and Lyklema and (b) Lim and Franses (c) Myers and Saville.....	75
5.7	Long cylindrical dielectric cell. H and L are the high and low terminal. G is ground. E_U and E_L are the upper and low electrodes. M is the micrometer.....	78
5.8	Titration data of (a) 213.8nm (b) 364.1nm (c) 367.7nm (d) 624.3nm suspensions.....	81
5.9	(a) Four terminal pair measurement principle. (b) Actual four terminal pair connections.....	83
5.10	Apparent dielectric constants of (a) distilled water and (b) 1mM KCl solution using brass electrode.....	85
5.11	Apparent dielectric constants(\square). (a) Real dielectric constant(\circ) after subtraction of stray effects of distilled water at 100KHz. (b) Real dielectric constant(∇) after subtraction of electrode effects of 1mM KCl at 1KHz. (c) Real dielectric constant($+$) after subtraction of stray effects of 1mM KCl at 10KHz.....	86
5.12	Apparent dielectric constants of distilled water at (a) 1KHz and (b) 100KHz using brass(\square), platinum(\bullet), and platinum black(Δ) electrodes, respectively.....	87
5.13	Conductance vs. $1/l$ of 1mM KCl solution using Pt(Δ) and Pt black(\circ) electrodes at 100KHz. The solid line is a guide to the eye.....	91
5.14	Dielectric cell with guard ring arrangement. H and L are the high and low terminals respectively. G is ground, and E_U and E_L are the upper and lower electrodes.....	92

5.15	(a) A detailed electric circuit of the cell. (b) A measured equivalent circuit. The subscripts r, e, m stand for residual, electrode and measure, respectively. R_l is lead wire resistance.....	93
5.16	Real part(\square) and imaginary part(Δ) of dielectric constants of (a) distilled water and (b) 624.3nm suspensions with platinum black electrode.....	97
5.17	Real part(\square) and imaginary part(Δ) of dielectric constants of (a)367.7nm, (b)364.1nm and (c) 213.8nm suspensions with platinum black electrode.....	98
5.18	Real part(\square) and imaginary part(Δ) of dielectric constant of (a) distilled water and (b) 1mM KCl solution with brass electrode covered with tape....	100
5.19	Real part(\square) and imaginary part(Δ) of dielectric constants of (a) 367.7 nm and (b) 364.1nm suspensions with brass electrode covered tape.....	101
5.20	Time variation of dielectric behavior of 1mM KCl solution using small cell with Pt electrodes.....	102
5.21	Time variation of capacitance of 624.3nm suspensions at (a) 5mm and (b) 7.6mm using Pt electrodes. For clarity only the data for 3 of the 5 frequencies studied are shown.....	103
5.22	Time variation of the conductance of 624nm suspensions at (a) 5mm and (b) 7.6mm using Pt electrodes. For clarity only the data for 3 of 5 frequencies studied are shown.....	104
5.23	Time variation of 213.8nm suspensions with sand blasted electrodes at 1.9mm separation. For clarity only the data for 3 of the 5 frequencies studied are shown.....	106
5.24	Time variation of capacitance of 624.3nm suspensions at (a) 0.6mm and (b) 1.9mm using sand-blasted Pt electrodes. For clarity only the data for 3 of the 5 frequencies studied are shown.....	107
5.25	Time variation of conductance of 624.3nm suspensions at (a) 0.6mm and (b) 1.9mm using sand-blasted Pt electrodes. For clarity only the data for 3	

of the 5 frequencies studied are shown.....	108
5.26 Time variation of the capacitances of suspensions of (a) 213.8nm, (b) 364.1nm, (c) 367.7nm and (d) 624.3nm using sand-blasted Pt electrodes at 0.05" separations.....	109
5.27 Time variation of the conductances of suspensions of (a) 213.8nm, (b) 364.1nm, (c) 367.7nm and (d) 624.3nm using sand-blasted Pt electrodes at 0.05" separations.....	110
5.28 (a) Real parts , (b) conductivities and (c) imaginary parts of suspensions using sand-blasted Pt electrodes.....	112
5.29 (a) The conductivity of 367.7nm suspensions vs. frequency. (b) The imaginary part of 367.7nm suspensions with choice of different DC conductivity. The numbers in the legend correspond to the frequencies where the DC conductivity was taken.....	113
5.30 Dielectric behavior of 624.3nm suspension using small cell with Pt electrodes.....	115
5.31 Dielectric behavior of 367.7nm suspension using small cell with Pt electrodes.....	116
5.32 Dielectric behavior of 364.1nm suspension using small cell with Pt electrodes.....	117
5.33 Dielectric behavior of 213.8nm suspension using small cell with Pt electrodes.....	118
5.34 The characteristic frequencies vs. reciprocals of the square of the particle diameter.....	119

Motivation

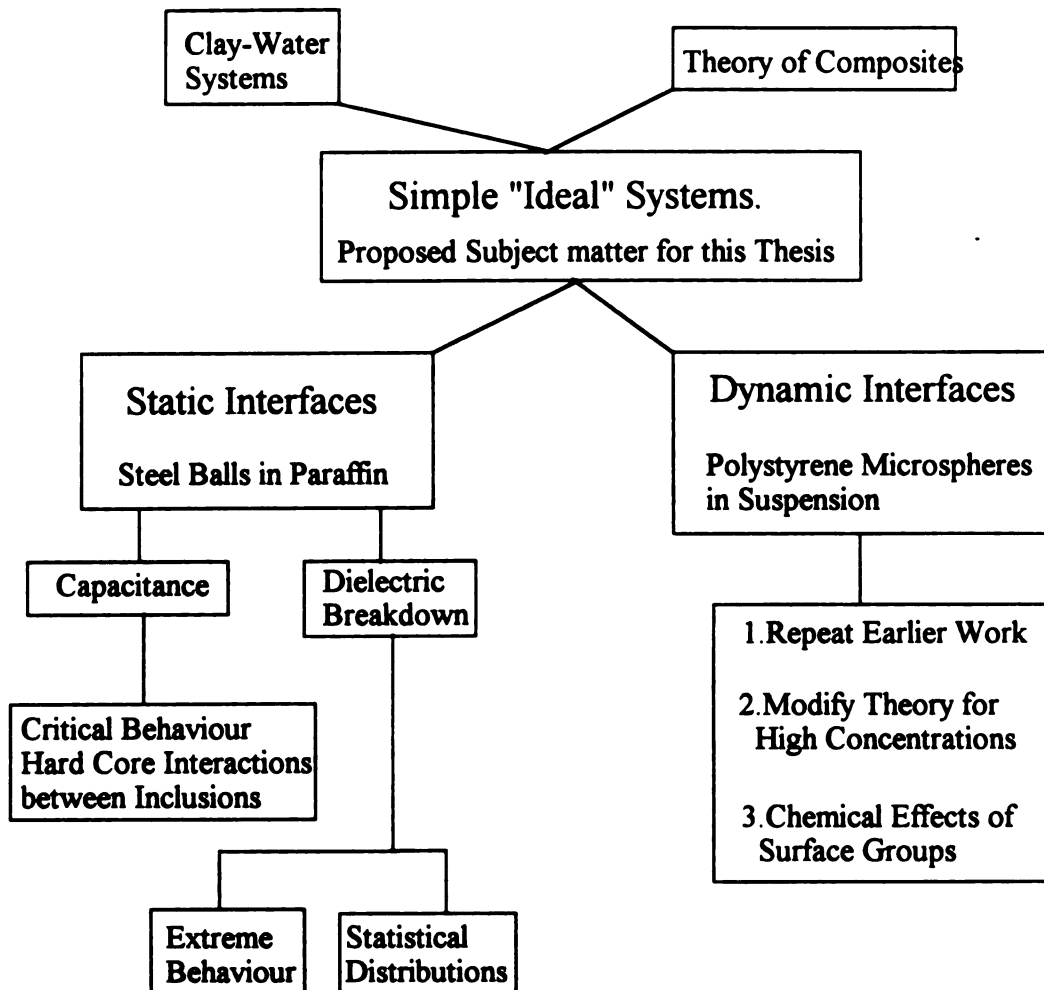
In the accompanying flow diagram we give the original sources of interest in the work of this thesis. On one side there was the interest in the clay-water system originating from prior work in the chemistry and physics departments, and on the other the theoretical interest of Dr. Duxbury. The explanation of the dielectric behavior of the clay water system is not easy because the platelet shape of the clay particle is difficult to deal with mathematically. Thus it is better to study simple ideal systems which are mathematically tractable. The lessons learned from these systems may be then be applied to the complicated systems. We consider two interface systems.

First for a static interface system, where there is no mass transport involved, we made metal loaded dielectric samples. Microspheres in a continuum background constitute the simplest system to deal with mathematically. In contrast with percolation theory, in which mathematical inclusions can overlap, real systems have a hard core repulsion between inclusions. The object was to study the effect of such hard core repulsion on the capacitance of metal particles in a pure dielectric. In dielectric breakdown the concern is with low concentrations where the difference between percolation theory and hard core repulsion is minimal. The dependence on local field distribution provides a great contrast with the capacitance treatment. The object was to study the contrasting relations using the guidance of Duxbury theory.

Second for a dynamic interface system we studied the properties of polystyrene spheres in ionic solution. This is a prototypical model for the effect of dynamic interfaces on dielectric response. Surprisingly despite recent theoretical interest, the only comprehensive measurement on this system dates from 1962. Our experimental program

is to first control the polarization effect at the electrodes, and then to measure the dielectric response of the polystyrene system as a function of frequency, ionic strength of the solution and type of polystyrene surface functional group.

Structure-Property Relationships in Random Continuum Composites.



Chapter 1

Capacitance

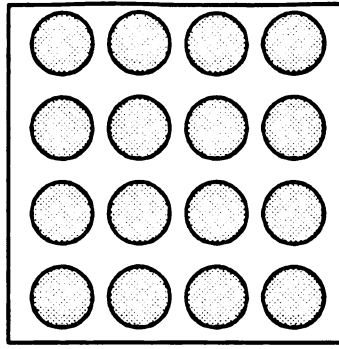
1.1 Introduction

There is an enormous variety of physical systems in which random inhomogeneities occur. It is not therefore surprising that the electrical properties of randomly inhomogeneous materials have been of interest for a long time. One way of studying the electrical properties of random systems is to investigate the capacitance of such a system. Dielectrics which contain metal inclusions are useful for this purpose.

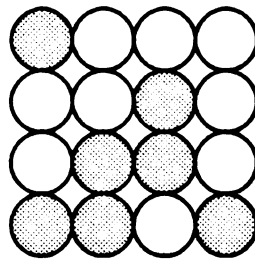
In this chapter we review the theoretical predictions regarding the capacitance of such dielectrics. To test the theoretical predictions we describe experiments on discs of paraffin wax which contained stainless steel particles and copper spherical particles.

1.2 Theory

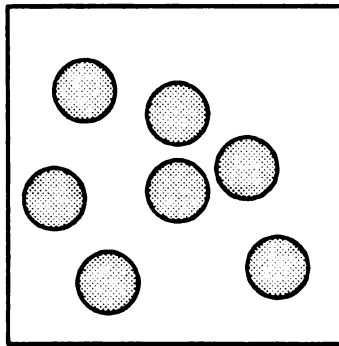
When a metal inclusion is added to a simple insulator the capacitance of the system is increased. Fig.1.1 shows three models of microstructures we consider. Fig.1.1(a) illustrates a regular array of metal particles. Fig.1.1(b) shows a mixture of two different kinds of particles, which can randomly occupy the available sites. A crystalline random alloy fits in this category. Fig.1.1(c) depicts a random distribution of inclusions in a continuum host. We consider the capacitance of a system consisting of metal spheres embedded in paraffin wax, so that a model of the form shown in Fig.1.1(c) is appropriate.



(a)



(b)



(c)

Fig.1.1: Two-dimensional examples of model microstructures: (a) a regular array of metal particles in a continuum background; (b) a site percolation model composed of metal spheres and insulating spheres and (c) a random configuration of metal particles in a continuum background.

The effective capacitance of a metal loaded dielectric is proportional to the dielectric constant of the background and depends upon f , the fractional volume occupied by the spheres.

1.2.1. Low loading limit

At a low concentration of inclusions, interactions between inclusions are negligible so the detailed form of the microstructure is not important. When an inclusion is embedded in a dielectric medium the effective dielectric constant can be obtained by using the Clausius-Mossotti approximation[1], i.e.,

$$\frac{\epsilon - \epsilon_1}{\epsilon + 2\epsilon_1} = f \frac{\epsilon_2 - \epsilon_1}{\epsilon_2 + 2\epsilon_1}, \quad (1.2.1)$$

where ϵ is the effective dielectric constant, ϵ_1 and ϵ_2 are the dielectric constants of the background and the inclusion respectively and f is the volume fraction of the inclusions. (This equation is identical to Maxwell-Wagner equation developed in Section 4.3.) In the case of conducting inclusions like metal, $\epsilon_2 \gg \epsilon_1$, and we can approximate Eq.(1.2.1) for the special case $\epsilon_2 \rightarrow \infty$, i.e.,[2]

$$\frac{\epsilon - \epsilon_1}{\epsilon + 2\epsilon_1} = f. \quad (1.2.2)$$

For small f the ratio of dielectric constants becomes

$$\frac{\epsilon_1}{\epsilon} \sim 1 - 3f. \quad (1.2.3)$$

This equation indicates that the ratio of dielectric constant varies linearly with the inclusion concentration.

1.2.2 High loading limit

As the volume fraction of metal particles is increased one must consider the interactions. This is especially important near the percolation point at which the inclusions first form a connecting path across the sample. Near that point the spheres are

very close to each other, and are separated by a very narrow neck. Duxbury argues that, if the neck size distribution is narrow, critical behavior in the same universality class as that of a regular array of spheres might be observed[3]. If this is true the critical behavior can be obtained in the following way.

We consider a cubic array of perfect conducting, identical spheres embedded in a continuum background as depicted in Fig.1.2(a). Fig.1.2(b) shows the enlargement of the critical part of a unit cell. The distance between the centers of two spheres is denoted by c and a is the radius of the sphere. When an external field is applied no current flows across the symmetry planes parallel to the field (dotted in Fig.1.2(a)). Since we consider the volume fraction of spheres near the random packing point, spheres are nearly touching. Therefore most of the current flows across the narrow gaps separating adjacent spheres along the z -axis. The capacitance between two spheres is like that between two plates of non-uniform separation.[4] If we neglect the charge in the region $r > a$ the capacitance can be obtained approximately from

$$C = \frac{1}{2} \int_0^a \epsilon \frac{2\pi r dr}{c/2 - \sqrt{a^2 - r^2}} \quad (1.2.4)$$

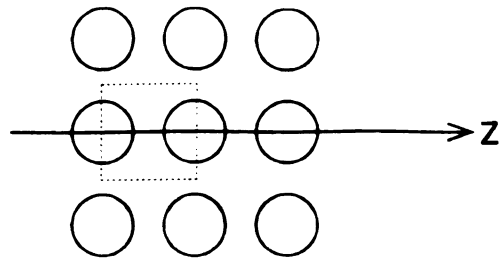
Near the random packing point the gap between spheres is very narrow so that the capacitance between two spheres is dominated by this narrow gap. Thus we may approximate

$$\begin{aligned} C &= \pi \epsilon \int_0^a \epsilon \frac{r dr}{c/2 - a + r^2/2a} \\ &\approx -\pi \epsilon a \ln[c/2a - 1] \end{aligned} \quad (1.2.5)$$

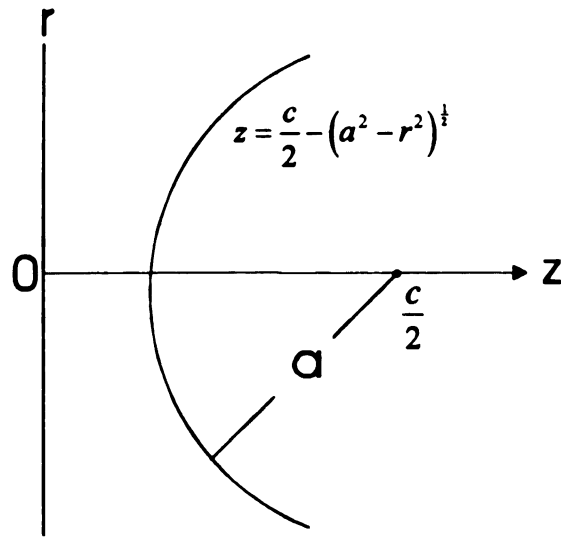
In the above equation we have neglected terms like $\ln a$ which remain finite when $c/2a$ approaches unity. The volume fraction is given by $f = (4\pi/3)(a/c)^3$. Eq.(1.2.5) can be rewritten as

$$C \approx -\pi \epsilon a \ln[\frac{1}{2}(4\pi/3f)^{\frac{1}{3}} - 1] \quad (1.2.6)$$

This equation diverges at $f = \pi/6$ so that we may write this



(a)



(b)

Fig.1.2: (a) Cross section of a cubic array of conducting spheres of radius a with distance c between centers. The dotted line is the cross section of a cube of side c . (b) Enlarged view of the gap between a plane midway between two spheres, and one of the spheres.

$$C = -\pi\epsilon a \ln[(\pi/6 - f)] \quad (1.2.7)$$

This last form is valid only when $\pi/6 - f \ll 1$. Similarly we can get the capacitance of the array of identical conducting discs. The diameter of each disc is a and the distance between two discs is c . We then calculate the capacitance between two adjacent discs like Eq.(1.2.4), i.e.,

$$C = \frac{1}{2} \int_{-a}^a \epsilon \frac{dx}{\sqrt{a^2 - x^2} + c/2} \quad (1.2.8)$$

This integral can be done by introducing new variable $x = a \cos \phi$ and we get

$$C \approx \epsilon \frac{c}{2a} \frac{2}{\sqrt{c^2/4 - a^2}} \tan^{-1} \sqrt{\frac{c/2 + a}{c/2 - a}} \quad (1.2.9)$$

When $c/2a$ approaches unity

$$C \approx \frac{\pi\epsilon}{\sqrt{c^2/4 - a^2}} \quad (1.2.10)$$

This equation can be rewritten in terms of volume fraction $f = \pi(a^2/c^2)$ as

$$C \approx \frac{\epsilon\pi^{\frac{1}{2}}}{c} \frac{1}{\sqrt{\pi/4 - f}} \quad (1.2.11)$$

The Eqs.(1.2.7) and (1.2.11) are valid only if $c/2a$ approaches unity. Thus we may express the critical behaviors:

two dimension

$$C(f) \approx C(0)(f_* - f)^{-1/2} \quad (1.2.12)$$

three dimension

$$C(f) \approx -C(0) \ln(|f_* - f|) \quad (1.2.13)$$

Here f_* is the volume fraction at which the capacitance diverges. The critical behaviors of these equations are illustrated in Fig.1.3. The two dimensional model gives more rapid divergence than does the three dimensional one near the critical point. But we will see that it is very difficult to verify these critical behaviors experimentally due to sample to sample variability in f_* . This is because the metal spheres do not achieve an equilibrium or liquid-like structure, but are in a random packing state. There are two extreme random

packing states, random close packing and random loose packing. The random close packing state

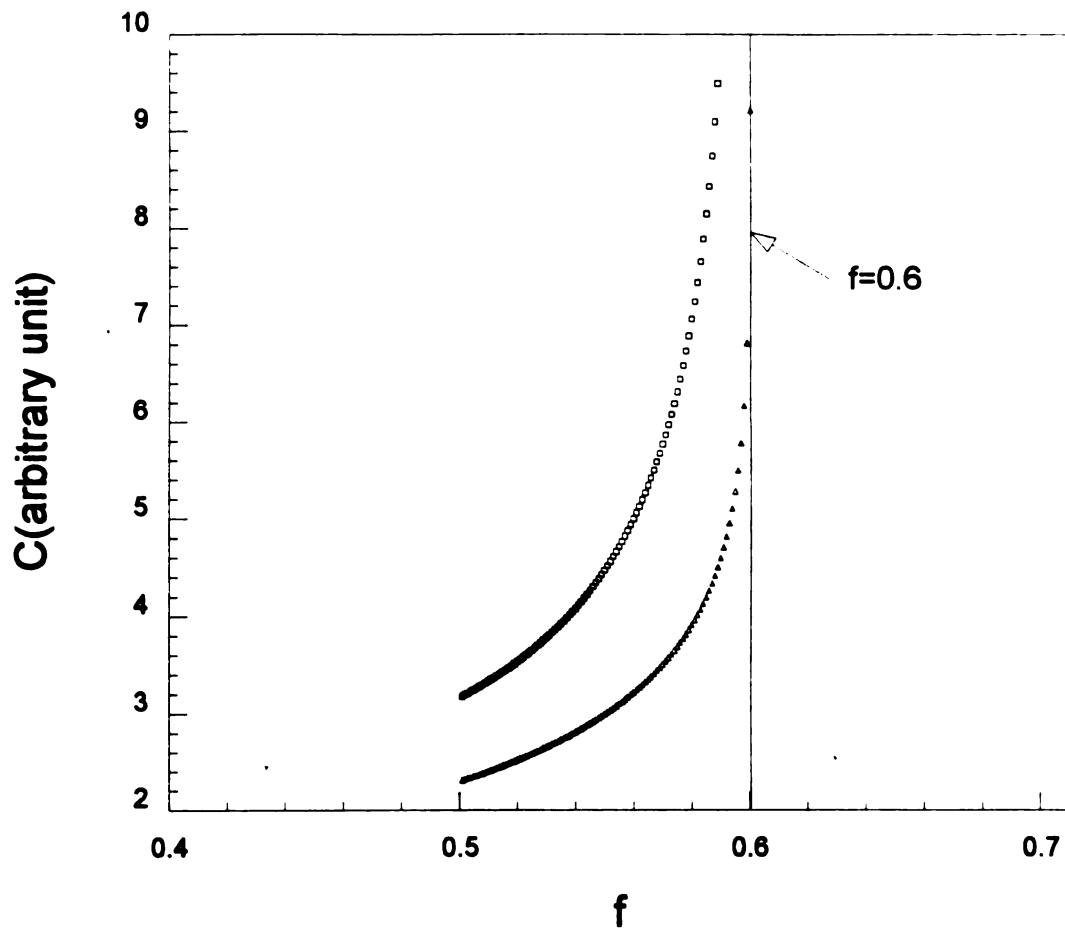


Fig. 1.3: Critical behaviors of Eqs.(1.2.12)(□) and (1.2.13)(Δ). Using $f_c=0.6$.

can be observed by pouring ball bearings into a container with shaking, while the random loose packing state occurs when the container is not shaken. We consider the random close packing state. Random close packing can be defined by the following two conditions[5]: (1) random packing, i.e., a packing containing no statistically significant short- or long-range order, is so dense that any increase in density can be achieved only by a statistically significant increase in short-range order; and (2) any decrease in density from the random close-packed density leads to ensembles of particles which need not be close packed, i.e., a given particle is not necessarily in contact with another particle in the absence of interparticle forces and gravitational potentials. Since the random close packing state is not an equilibrium state f_c does not approach a single limit value. The observed f_c is in the ranges $0.82 < f_c^{2d} < 0.89$ and $0.58 < f_c^{3d} < 0.66$ for identical spherical particles[6,7].

1.2.3 Frequency dependence

Eq.(1.2.1) does not include the interaction of inclusions so that the validity of the equation is for low concentration of inclusions. We can obtain the effective dielectric constant at high concentration using effective medium theory which is the most commonly invoked approximation in treating an inhomogeneous medium. Let us consider a two component medium with dielectric constants ϵ_1 and ϵ_2 respectively. Take one of the components type 1 and consider it as spherical, and assume it is embedded in a uniform medium with an effective dielectric constant ϵ_m . If the external electric field is E_0 then the induced dipole moment is[8]

$$P = \frac{3}{4\pi} V \frac{\epsilon_1 - \epsilon_m}{\epsilon_1 + 2\epsilon_m} E_0, \quad (1.2.14)$$

where V is the volume of the sphere. Thus the field inside a sphere is given by

$$E = E_0 - \frac{4\pi}{3} P$$

$$= E_0 - \left(\frac{\epsilon_1 - \epsilon_m}{\epsilon_1 + 2\epsilon_m} \right) E_0. \quad (1.2.15)$$

The second term is the depolarization field due to uniform polarization of a sphere. P is the polarization which is the electric dipole moment per unit volume. After the completion of the exchanges the average deviation of E must be zero. Therefore

$$(1-f) \frac{\epsilon_1 - \epsilon_m}{\epsilon_1 + 2\epsilon_m} + f \frac{\epsilon_2 - \epsilon_m}{\epsilon_2 + 2\epsilon_m} = 0, \quad (1.2.16)$$

where f is the volume fraction of the component 2. If the two components have complex dielectric constants then Eq.(1.2.16) can be rewritten by

$$(1-f) \frac{\epsilon_1^* - \epsilon_m^*}{\epsilon_1^* + 2\epsilon_m^*} + f \frac{\epsilon_2^* - \epsilon_m^*}{\epsilon_2^* + 2\epsilon_m^*} = 0. \quad (1.2.17)$$

Here the dielectric constant is defined by

$$\epsilon_i^* = \epsilon_i' - j \frac{\sigma_i}{\omega}, \quad i=1,2 \text{ or } m \text{ and } j = \sqrt{-1}. \quad (1.2.18)$$

The solutions of Eq.(1.2.17) was given by Springett[9] assuming ϵ_1 , ϵ_2 , σ_1 and σ_2 are independent of frequency and are

$$\epsilon_m = \epsilon \pm \epsilon_2 \left[(A^2 + B^2)^{1/2} - A \right]^{1/2} \tan \delta_2, \quad (1.2.19a)$$

$$\sigma_m = \sigma \pm \sigma_2 \left[(A^2 + B^2)^{1/2} + A \right]^{1/2}, \quad (1.2.19b)$$

where

$$A = \frac{1}{2} \left\{ \left(\frac{\sigma}{\sigma_2} \right)^2 + \frac{1}{2} \frac{\sigma_1}{\sigma_2} - \left[\left(\frac{\epsilon}{\epsilon_2} \right)^2 + \frac{1}{2} \frac{\epsilon_1}{\epsilon_2} \right] (\tan \delta_2)^{-2} \right\}, \quad (1.2.20a)$$

$$B = \left(\frac{1}{4} \frac{\sigma_1}{\sigma_2} + \frac{\epsilon \sigma}{\epsilon_2 \sigma_2} + \frac{1}{4} \frac{\epsilon_1}{\epsilon_2} \right) (\tan \delta_2)^{-1}, \quad (1.2.20b)$$

$$a = \frac{1}{4}(3f-1)a_2 + \frac{1}{4}(2-3f)a_1, \quad a = \sigma \text{ or } \epsilon, \quad (1.2.20c)$$

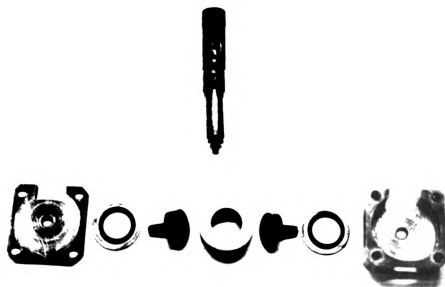
$$\tan \delta_2 = \sigma_2 / \omega \epsilon_2. \quad (1.2.20d)$$

According to effective medium theory the effect of frequency occurs through the factor $\tan \delta_2$, ϵ_1^* and ϵ_2^* .

1.3 Experiments and discussion

The metal loaded dielectric we have used is paraffin wax containing stainless steel particles and copper particles. The size of the steel particles which are manufactured by Duke Scientific Inc. ranges from 10 μm to 65 μm diameter. The copper particles (Aldrich Chemical Co.) range from 50 μm to 90 μm diameter. The cell used to make a mixture is depicted in Fig.1.4. First we weighed the particles and poured them into the cell. We heated the whole cell above the melting point of the paraffin wax. The cell was filled with molten paraffin wax and then the whole cell was pumped with a fore pump to make the sample without air bubbles. Finally it was sealed with a metal cylinder which contained paraffin wax. A 45 μm mesh sieve was used between the cell and the cylinder to prevent migration of the particles into the cylinder. High pressure was maintained inside the cylinder by a strong spring, so that high pressure liquid paraffin compensated the volume contraction due to cooling. The whole cell was rotated by a slow motor at about 60 rpm to ensure a random distribution of the steel particles while cooling. The capacitance samples were 3/4" in diameter and 5mm in thickness. Typical optical photomicrographs of a sample fabricated by this method are shown in Fig.1.5, from which it can be seen that the steel spheres are fairly well distributed. Fig.5 (c) and (d) indicate that the steel balls are spherical but the copper balls have gross departures from sphericity. Samples that contain stainless steel and copper particles were made with volume fractions ranging from 0 to 0.62 and from 0 to 0.41 respectively.

The cell used to measure the capacitance of the sample is a circular plane capacitor with the guard ring arrangement shown schematically in Fig.1.6(a). The guard ring arrangement can be used to get a uniform sample field by eliminating the edge effect provided that the total diameter of the electrode is large by comparison with the sample thickness d . In addition to this, the center electrode and the guard ring must be at the same potential. Thus a linear relationship between dielectric constant and capacitance, i.e.,



(a)



(b)

Fig 1.4: Cell used to make paraffin disks.

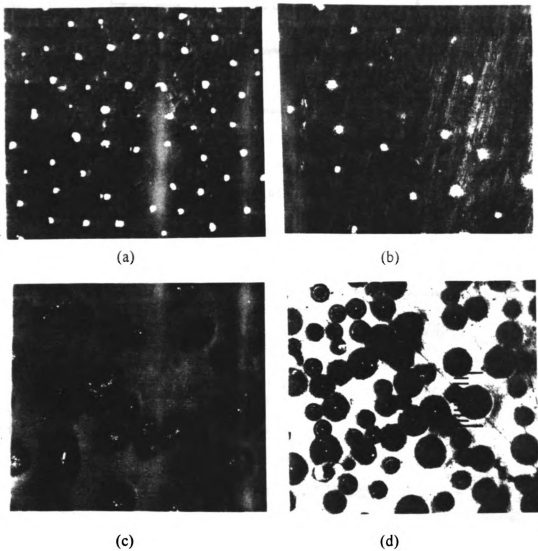


Fig. 1.5: (a) and (b) Optical photographs of cross section of metal loaded paraffin discs.
(c) Copper particles. (d) Stainless steel particles.

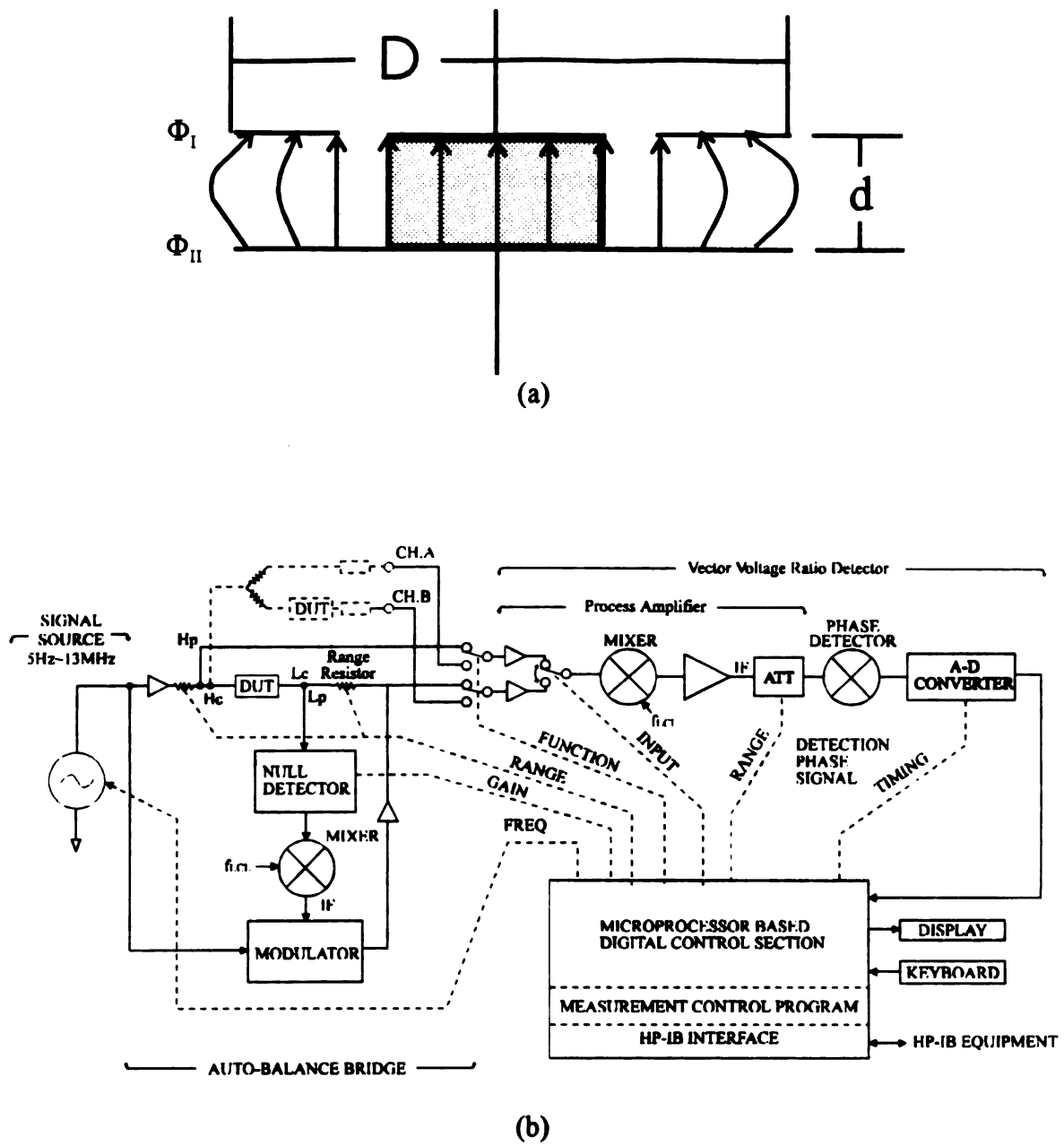


Fig.1.6: (a) Principle of guard ring to assure uniform sample field. (b) Block diagram of HP 4192A impedance analyzer.

$$C = \epsilon_0 \epsilon \frac{S}{d}, \quad (1.3.1)$$

can be achieved. Here ϵ_0 and ϵ are the absolute permittivity of free space and the relative permittivity of the sample respectively, S is the area of electrode and d is the sample thickness. There are two equivalent circuits we may consider, i.e., parallel and series equivalent circuits. Table 1.1 gives the relationship between the two circuit modes.

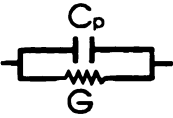

The capacitance was measured using a 4192A Hewlett Packard Impedance Analyzer. The analyzer is set to measure parallel capacitance. A schematic diagram of the measurement circuit is illustrated in Fig. 1.6(b). The HP4192A has three subsections (1) the signal source, (2) the auto-balance bridge and (3) the vector ratio detector. It measures the vector ratio between the applied test signal voltage and the current flowing through the DUT(device under test). The bold lines in the block diagram show the main test signal flow and the dashed lines show the balance control loop of the bridge circuit. In the auto-balance bridge the null detector detects the current difference between DUT and the range resistor. When it is not zero the modulator adjusts it to zero by applying a signal, V_r , of the same frequency as the test signal to the range resistor. The vector voltage ratio detector measures the vector voltage of a test signal V_s , and a signal applied to the range resistor. The impedance of the DUT, Z_x , can then be calculated by

$$\frac{V_s}{Z_x} = \frac{V_r}{R_r}, \quad (1.3.2)$$

where R_r is the resistance of the range resistor.

In actual measurement the guard ring is connected to ground and center electrode is connected to the low terminal. When the bridge is balanced no current flows through the detector so that the guard ring and the center electrode are kept at the same potential, which is essential if a uniform field is required.

Table 1.1 Conversion table of each equivalent circuit mode.

Circuit Mode	Dissipation Factor	Conversion to Other Modes
	$D = \frac{G}{\omega C_p}$	$C_s = (1 + D^2)C_p, \quad R = \frac{D^2}{1 + D^2} \cdot \frac{1}{G}$
	$D = \omega C_s R$	$C_p = \frac{1}{1 + D^2} C_s, \quad G = \frac{D^2}{1 + D^2} \cdot \frac{1}{R}$

The capacitance of the samples measured at 1KHz are presented in Fig.1.7. At each volume concentration 10 samples were tested. For the stainless steel samples the critical volume fraction f_c is consistent with the random packing point as discussed before. But for the copper samples the critical volume fraction f_c is not consistent with the random packing point because they are not exact spheres so that they made a percolation path before that point. Nevertheless capacitances of both samples diverge as f_c is approached. As the metal volume fraction is increased the capacitance values at each volume concentration spread widely. It means that a small change of structure causes a large change in the capacity of the sample. Capacitance change near the percolation point is much more rapid than that at low loading range. This change is more drastic for copper samples than for stainless steel samples because the conductivity of copper is much greater than that of stainless steel. In deriving Eq.(1.2.13) the assumption is made that the metals are perfect conductors. It turned out that the stainless steel particles are not good conductors and they are paramagnetic. The conductivity of the copper and stainless steel particles was studied by filling the cell with metal by itself. The total resistance of the cell filled with copper particles was the order of 1Ω but that with stainless steel particles was

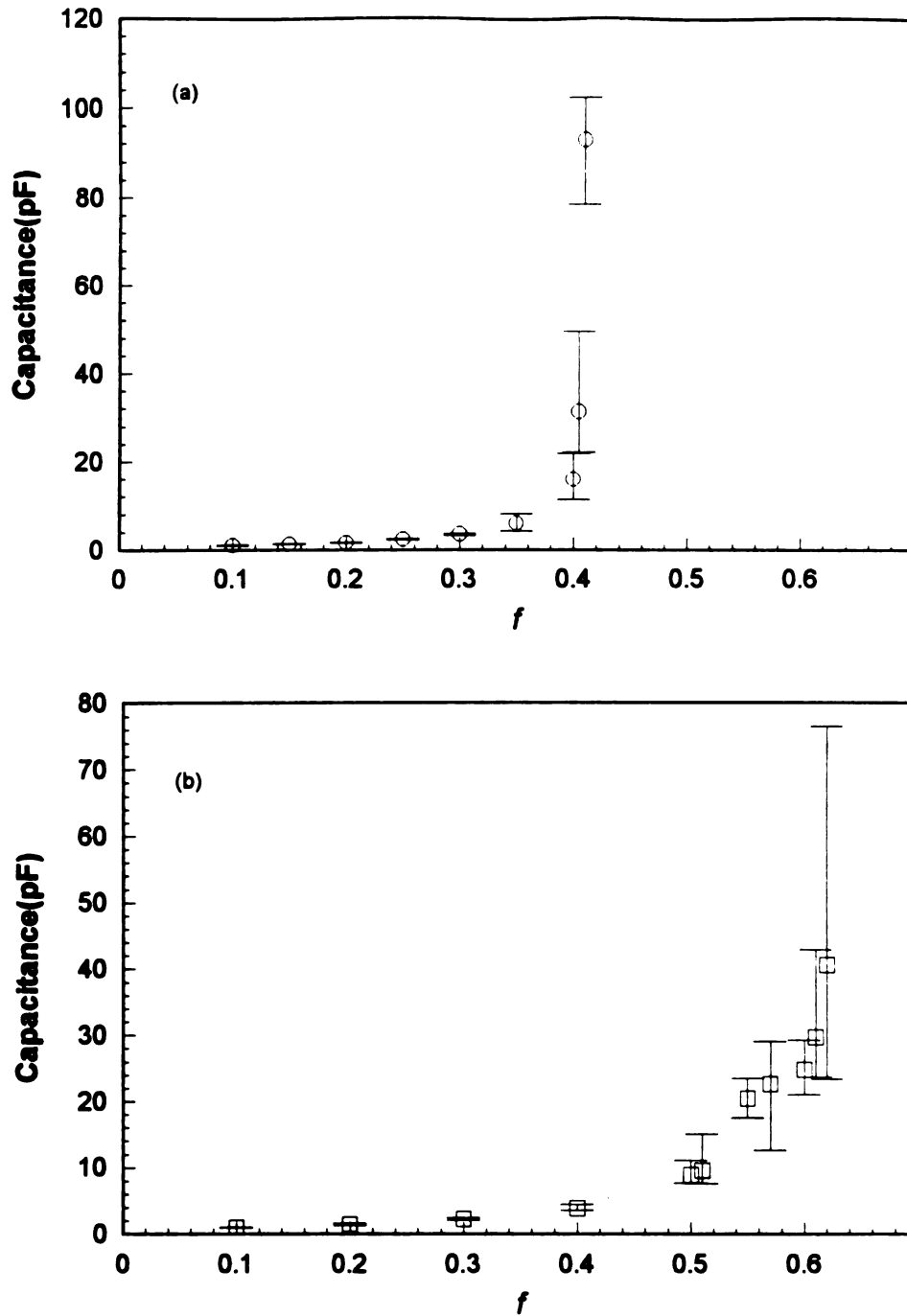


Fig.1.7: Capacitances of paraffin wax containing (a) copper particles and (b) stainless steel particles against their volume concentrations. Error bar indicates minimum and maximum values.

the order of $1\text{M}\Omega$ at 1KHz . In this test capacitance was out of the range of instrument (more than $10\mu\text{F}$) for the copper sample while it was still finite value for the stainless sample. Therefore a good conductor is great for this purpose. Even though the copper is good conductor it is hard to handle because it oxidizes easily. If the copper is oxidized it acts as bad conductor. To keep the copper particles from oxidation they had to be stored in a vacuum container after being cleaned by 20% diluted HCl.

Fig.1.8 shows capacitance ratio $C(0)/C(f)$ as a function of metal volume fraction. We also show numerical data calculated by McPhedran and McKenzie using a simple cubic lattice of conducting spheres[10]. At very low loading (below 0.1) all data are very close to each other but after that experimental capacitances are larger than those from numerical simulations. This is because at very low loading the probability of making a linear cluster in a random mixture is very low so that capacitance is not much increased.

When the metal fraction is increased the chance of making a linear cluster in a random mixture also increases. This cluster enhances the local field and increases the capacitance but in the simple cubic array metal inclusions do not touch each other up to f_c . Both experimental results below a volume fraction of 0.2 show linear behavior which is consistent with Eq.(1.2.3).

Fig. 1.9 shows capacitance ratio against $\ln(f_c - f)$ for large f . If Eq.(1.2.13) is correct the data should be linear. The f_c 's obtained from the least χ^2 fitting are 0.65 for stainless steel and 0.41 for copper. Eq.(1.2.13) can be rewritten by

$$C(f)/C(0) \approx \ln(f_c - f)^\alpha. \quad (1.3.3)$$

Analytical derivation gives $\alpha=-1$. For experimental data this exponent can be obtained by plotting $\ln[C(f)/C(0)]$ against $\ln[\ln(f_c - f)^\alpha]$ with α as a parameter. α 's obtained from the least χ^2 -fitting are -0.15 for stainless steel and -0.86 for copper (See Fig.1.10). Comparing Figs. 1.7(a) and (b) we see that the high conductivity Cu gives a much sharper rise near f_c than does the low conductivity stainless steel. We therefore suspect that the

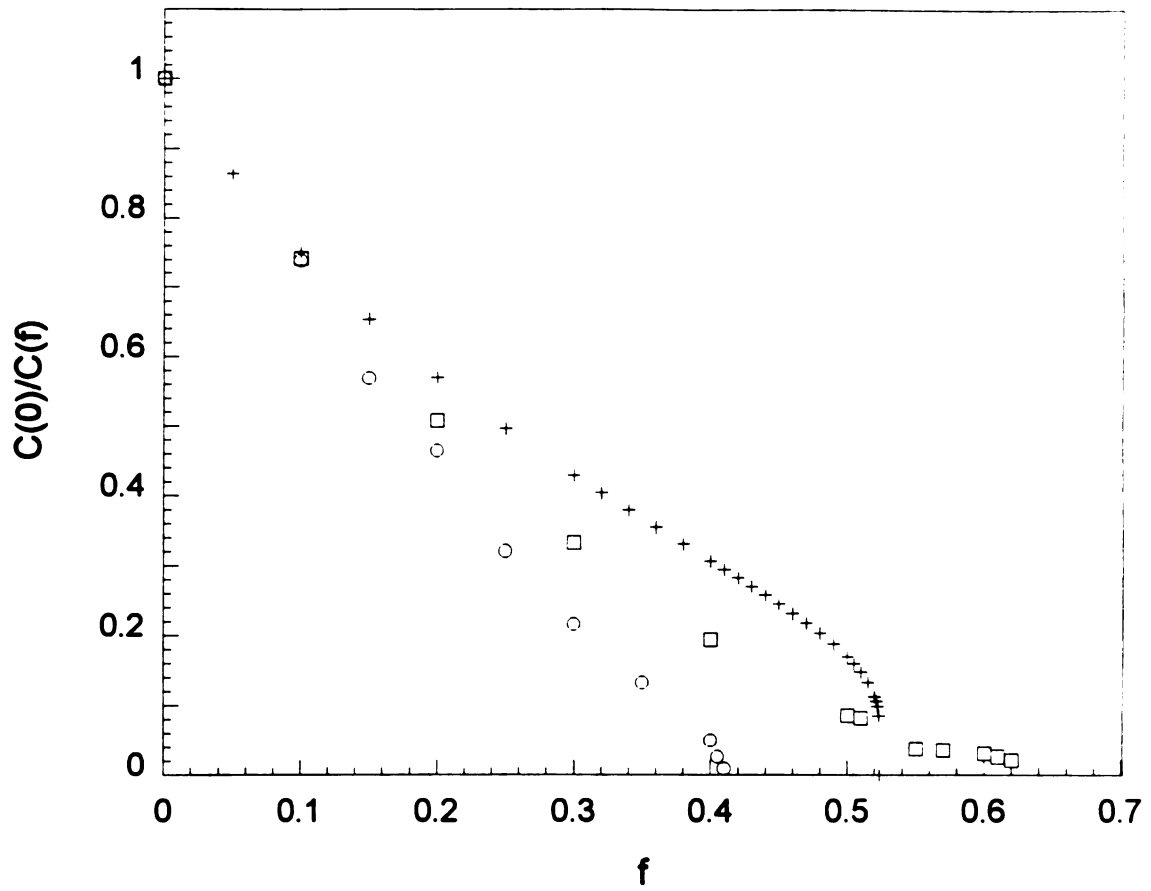


Fig.1.8: The capacitance ratio, $C(0)/C(f)$ as a function of the volume fraction of metal inclusions. Experimental values using stainless steel(\square) and using copper(\circ). Numerical simulations(+) calculated using a simple cubic lattice.

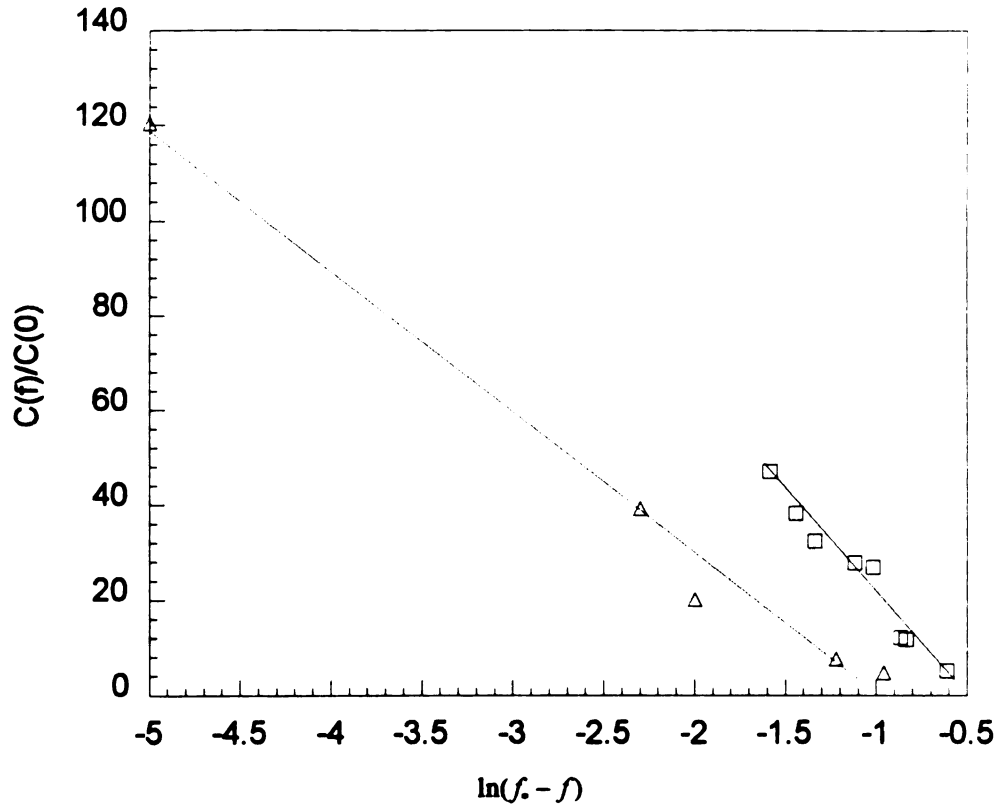


Fig. 1.9: Test of Eq.(1.3.3) for large f . If the Eq.(1.3.3) is correct the data plotted here should be linear. f^* 's used are 0.65 for stainless steel(\square) and 0.41 for copper(Δ). The solid lines are guide to the eye.

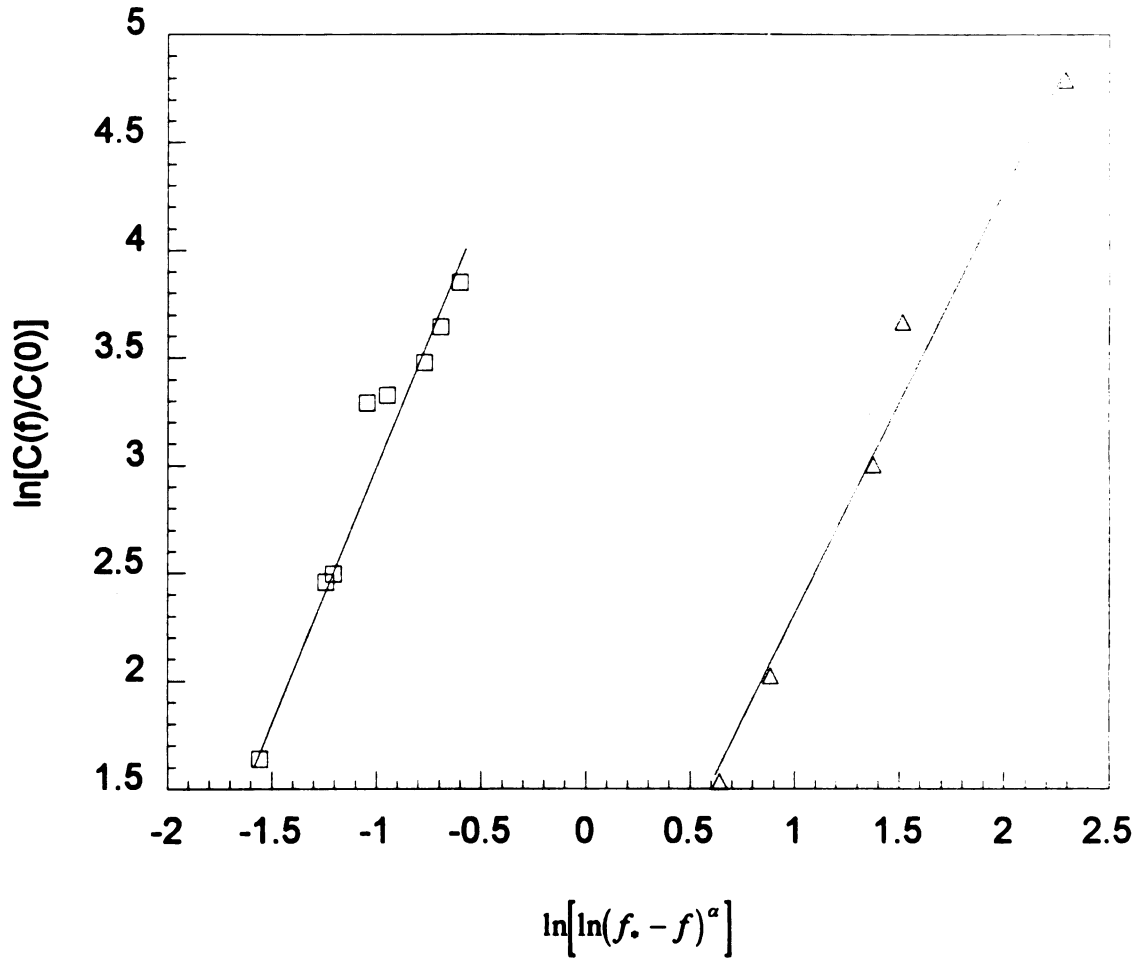


Fig.1.10: If Eq.(1.3.3) is correct the data plotted here should be linear. The best fitting parameters are $f_*=0.65$ and $\alpha=-0.15$ for stainless steel(□), and $f_*=0.41$ and $\alpha=-0.86$ for copper(Δ). The solid lines are guide to the eye.

value of $|\alpha_{ss}| < 1$ is indicative of the low conductivity of the stainless steel balls. Stainless steel particles do not obey the critical behavior represented by Eq.(1.2.13) due to their poor conductivity. Even though copper particles have good conductivity the behavior near f_* is not perfectly consistent with that predicted by Eq.(1.2.13) due to considerable sample to sample variability in f_* , and probably non-sphericity of the balls.

Fig.1.11 shows the frequency dependences of the sample contained stainless particles. At low loading the dielectric constants are not dependent on frequency but at high loading the dielectric constants are a function of frequency. For metal inclusions in the dielectric material, $\epsilon_2 \gg \epsilon_1$ and $\sigma_2 \gg \sigma_1$ and $\tan\delta_2$ cancels so that Eqs.(1.2.19) become

$$\epsilon_m \sim \frac{1}{2}(3f - 1)\epsilon_2, \quad (1.3.4a)$$

$$\sigma_m \sim \frac{1}{2}(3f - 1)\sigma_2. \quad (1.3.4b)$$

Thus according to effective medium theory the complex dielectric constant of a metal loaded dielectric is not a function of frequency (Remember f is the volume fraction of balls not the frequency). To ascertain whether the frequency dependence was a property of the balls by themselves, or whether it was property of the mixture we measured the frequency dependence of the cell filled with stainless steel particles by themselves. The surprising results are shown in Fig.1.12. For a homogeneous metal one would expect a very high dielectric constant independent of frequency up to \sim I.R. region. On the other hand, the Duxbury picture of high capacitance regions in narrow necks would apply if the stainless steel balls were coated with an insulating oxide layer. Duxbury does not ascribe any frequency dependence in his theory.

Since Eqs.(1.2.19) are based on the mixture of elements whose dielectric properties do not depend on frequencies, the results in Fig.1.12 indicate that the theory is not appropriate for this mixture. There is no obvious relationship between the frequency dependencies in Figs.1.11 and 1.12.

One might also consider the stainless steel ball- oxide-stainless steel ball system as a Maxwell-Wagner system(See section 4.3) in which case one might anticipate a frequency

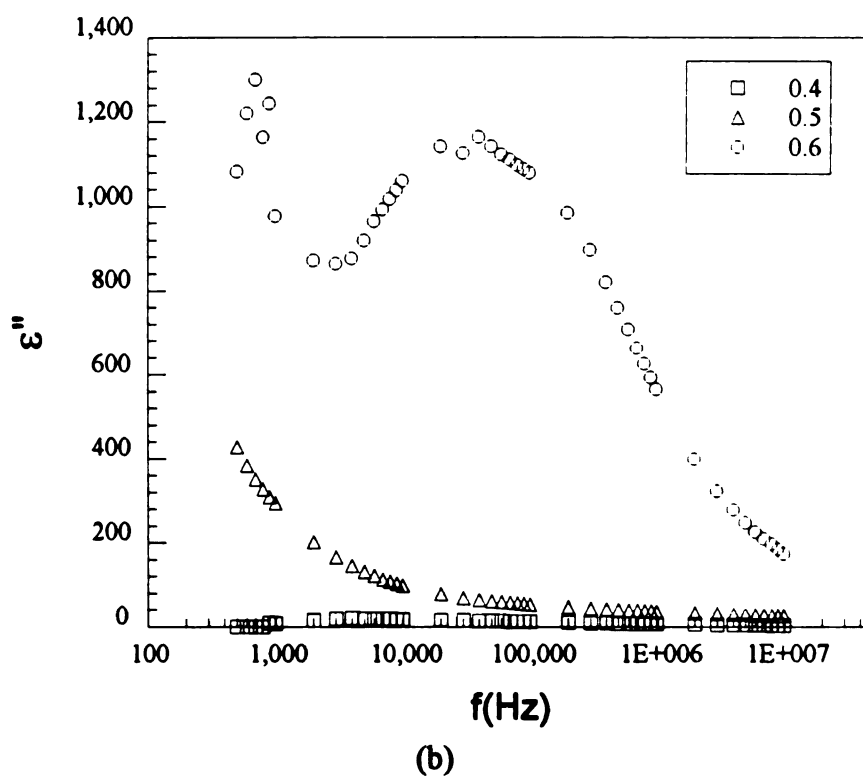
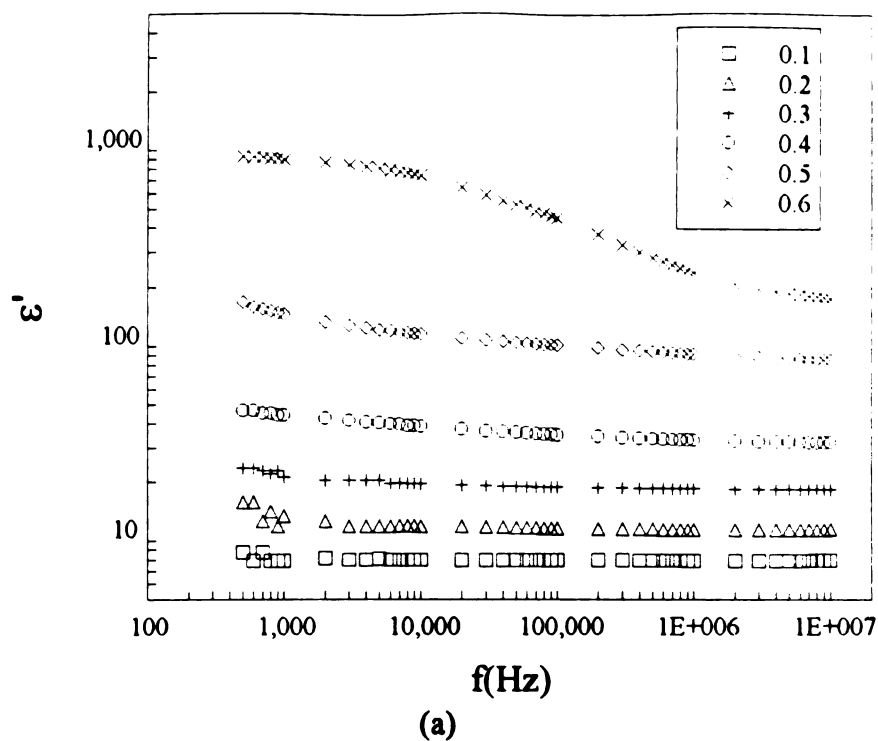


Fig. 1.11: (a) Real part and (b) imaginary part of the dielectric constant of paraffin wax containing stainless steel particles. Numbers in the legend are the concentrations of stainless steel particles.

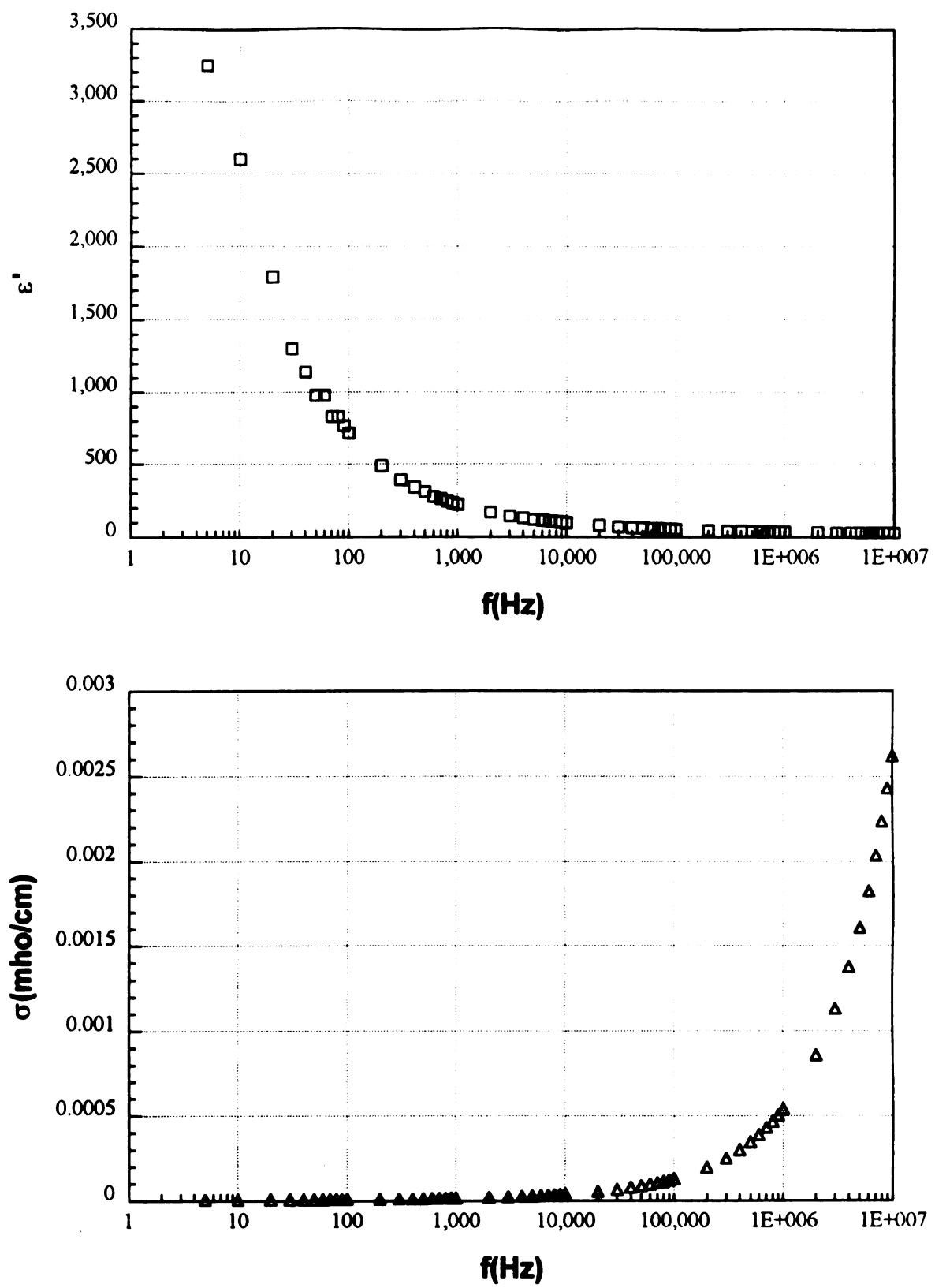


Fig.1.12: The frequency dependence of stainless steel particles.

dependence similar to that in Fig.4.3. This is not observed, but the results suggest that the next improvement on Duxbury theory would be to incorporate a Maxwell-Wagner component.

Bibliography

- [1] J. C. Garland and D. B. Tanner eds., Electrical Transport and Optical Properties of Inhomogeneous Media, AIP Conf. Proc. **40** (1978)
- [2] L. K. H. Van Beek, Progress in Dielectrics, **7**, 69 (1967)
- [3] P. M. Duxbury, P. D. Beale, H. Bak and P. A. Schroeder, J. Phys. D. Appl. Phys. **23**, 1546(1990)
- [4] J. B. Keller, J. Appl. Phys. **34**, 991 (1962)
- [5] J. G. Berryman, Phys. Rev. A. **27**, 1053 (1983)
- [6] W. M. Visscher and M. Bolsterli, Nature, **239**, 504 (1972)
- [7] G. Y. Onoda and E. G. Liniger, Phys. Rev. Lett. **64**, 2727 (1990)
- [8] J. D. Jackson, Classical Electrodynamics, 2nd Ed. pp151 (1975)
- [9] B. E. Springett, Phys. Rev. Lett. **31**, 1463 (1973)
- [10] R. C. McPhedran and D. R. McKenzie, Proc. R. Soc. Lond. A. **359**, 45 (1978)

Chapter 2

Dielectric breakdown

2.1 Introduction

A metal particle in an electric field increases the local electric field. If the metal particle has a sharp tip the enhancement of the local field is very large and a sharp metal tip acts as a nucleation site for dielectric breakdown. Therefore such a flaw in the material lowers its dielectric strength.

In this chapter the theoretical predictions of Duxbury are reviewed and experiments performed using paraffin wax containing stainless steel spheres are described. Duxbury proposed that in a metal loaded dielectric, metal particles can form a linear cluster which acts as a sharp tip.[1-3] Increasing the volume fraction of metal particles increase the probability of finding a large cluster which reduces the dielectric breakdown field. The theory predicts the field near the sharp metal tip as a function of metal volume fraction. Experimental results supported this theoretical prediction.

2.2 Theory

The theory is based on these premises:

- (1) Dielectric breakdown is directly related to flaws.
- (2) In the metal loaded dielectric the flaws consists of linear clusters of particles which act as a sharp tip.

(3) A long linear chain of metal particles can be regarded as a thin ellipse in two dimensions or as a thin prolate spheroid in three dimensions. If we ignore space charge effects solving the Laplace's equation gives the electric field near a metal inclusion of length, α , and tip curvature, κ .

(4) The breakdown is calculated using a square lattice dielectric breakdown model. The derivation of the electric field near a thin prolate spheroid is given in Appendix 1.

The resulting electric field near the metal tip and the important asymptotic behaviors are summarized below[4].

In these equations r is the distance from the metal tip in the direction of the applied field, $\kappa = b^2/2a$ is the tip curvature, and b and a are the minor and major axes of the ellipse(or spheroid). The applied electric field, E_o , is in the z direction.

Two dimensions

$$E_z/E_o \equiv \begin{cases} 1 + \alpha_{2d}/r^2 & \text{for } r > a \\ 1 + \{a/(a-b)\}(a/2r)^{1/2} & \text{for } \kappa < r < a \\ 1 + \sqrt{2}(a/2\kappa)^{1/2} & \text{for } r < \kappa \end{cases} \quad (2.2.1)$$

Three dimensions

$$E_z/E_o \equiv \begin{cases} 1 + \alpha_{3d}/r^3 & \text{for } r > a \\ \{\ln(r/2a) + a/2r\}/B & \text{for } \kappa < r < a \\ 1 + (a/b)^2/\ln(2a/b) & \text{for } r < \kappa \end{cases} \quad (2.2.2)$$

Here the coefficients are

$$\alpha_{2d} = a(a-b)/2,$$

$$\alpha_{3d} = 2c^3/3B,$$

$$B = \ln\left(\frac{b}{c+a}\right) + \frac{c}{a}.$$

Even when the metal particles are randomly placed in the material, there is finite probability that somewhere in the material, several metal particles will be close to each other. Within a lattice model, such a defect configuration is shown in Fig.2.1. For f small,

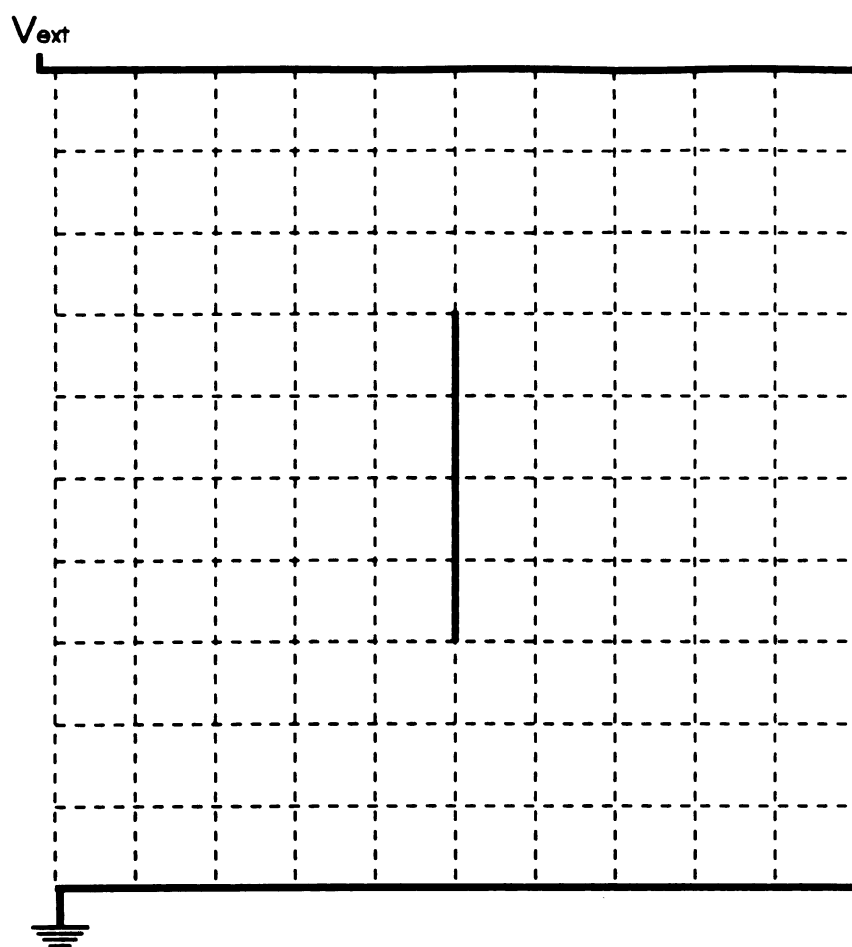


Fig.2.1: A field-enhancing cluster of conducting bonds(—) in a background of insulating bonds(-----).

the number of times a defect cluster of size n will occur in a sample of size $L^d = N$, is approximated by, Nf^n (here L is the linear dimension of the lattice). The electric field is largest near the largest such cluster, and the typical size of this largest defect cluster is estimated from [5]

$$Nf^{n_{\max}} \sim 1 \text{ which implies } n_{\max} \sim \ln N / (-\ln f). \quad (2.2.3)$$

From Eqs. (2.2.2) and (2.2.3), the electric field near the end of this defect cluster is found to scale as

$$E_{np} \sim E_0 (1 + n_{\max}^\alpha) \quad (2.2.4)$$

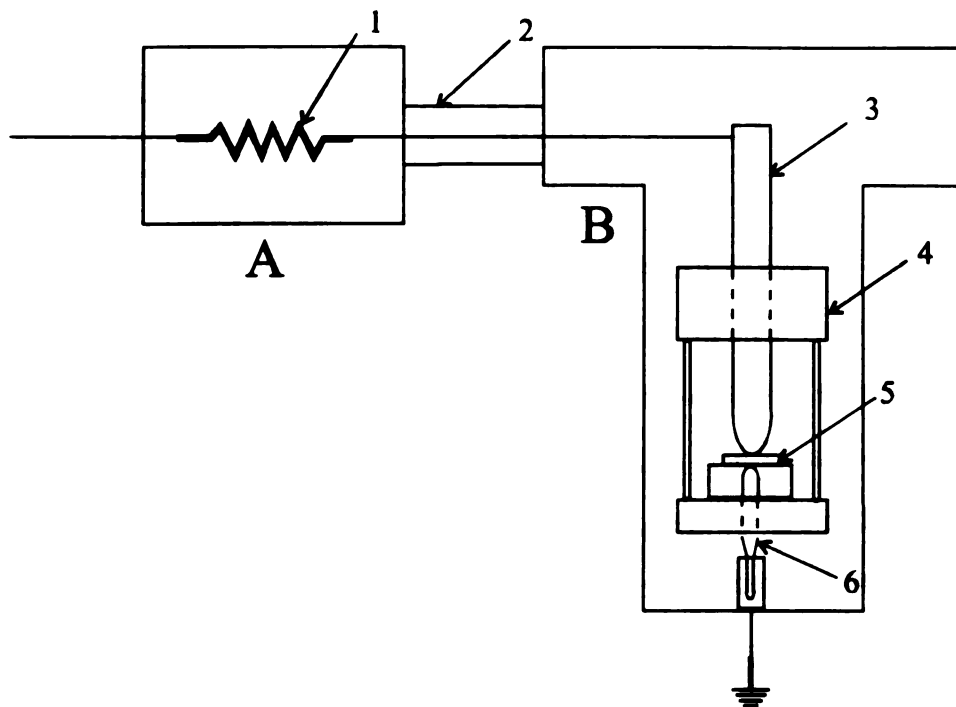
for n_{\max} large, where $\frac{1}{2} < \alpha < 1$ in two dimensions and $\alpha = 1$ in three dimensions. If we assume that the dielectric breakdown field, $E_b(f)$, scales as the inverse of the size of the largest local electric field, $E_{np}(f)$, then,

$$\begin{aligned} E_b(f)/E_b(0) &\sim E_{np}(0)/E_{np}(f) \\ &\sim 1 / \left[1 + k_c (\ln N / |\ln f|)^\alpha \right] \end{aligned} \quad (2.2.5)$$

where k_c is an undetermined constant.

2.3 Experiment and discussion

The samples we have used to measure the dielectric strength are paraffin waxes containing stainless steel spheres which are similar to those used in the capacitance experiments. The paraffin discs are fabricated by the method discussed in section 1.3. Thick samples were used in the capacitance measurement but we used thin samples (thickness 1mm, diameter 19mm) in the measurement of dielectric strength because the dielectric breakdown voltage is too high for the thicker samples. The power supply we used is manufactured by Gamma High Voltage Research Inc. (max. 100KV). The experimental setup is illustrated in Fig. 2.2. At very low loading the dielectric breakdown field of the sample is very high, so we must keep the ambient of the experimental setup



1. $3\text{M}\Omega$ Resistor
2. Teflon Rod
3. Upper Brass Electrode
4. Plastic Guide for Electrode
5. Sample
6. Lower Brass Electrode

Fig.2.2: A schematic diagram of breakdown experiment.

highly insulated in order to prevent unwanted discharge before the sample breaks. The entire system shown in Fig. 2.2 is, therefore immersed in silicon oil (Dow 550 Fluid) which has a very high dielectric strength (about 440KV/cm) so that the dielectric breakdown process occurs only through the sample. Furthermore, three $1\text{M}\Omega$ resistors were used to protect the power supply from a huge current just after a sample breakdown. The applied voltage was increased by 2KV steps every 30 seconds, until failure[6]. 10 samples were tested for each concentration.

Fig.2.3(a) shows the measured dielectric breakdown field as a function of volume fraction and Fig.2.3(b) shows the dielectric breakdown field calculated using the square lattice dielectric breakdown model. It is seen that the dielectric strength can be affected by a very small volume fraction of conducting defects. Fig.2.4(a) is the test of Eq.(2.2.5) using experimental results and Fig.2.4(b) is the result of numerical simulations done by Duxbury. From both results $\alpha = \frac{3}{2}$ is the best fitting parameter rather than $\alpha=1$ which is the analytical result. However the linearity with $\alpha = \frac{3}{2}$ for both experimental and simulated systems suggest that Eq.(2.2.5) is the correct form. This discrepancy may result from finite size effect[5]. The analytical calculation was derived in the limit of large sample size while the numerical simulation and the experiment were done on relatively small sample sizes. But both results give the α as a free parameter in Eq.(2.2.5) is correct.

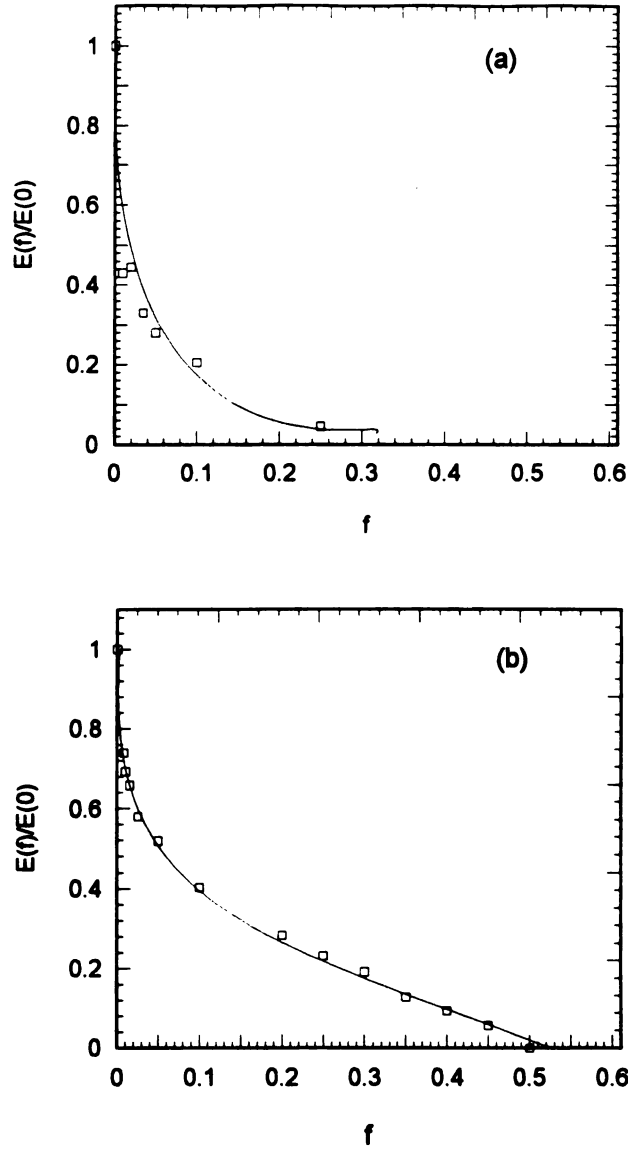


Fig.2.3: (a) The dielectric breakdown field ratio of experimental results on samples of paraffin wax containing stainless steel balls. (b) The dielectric breakdown field ratio calculated using the square lattice dielectric breakdown model[2]. Each point is an average over at least 50 configurations of 100×100 lattices. Solid lines are a guide to the eye.

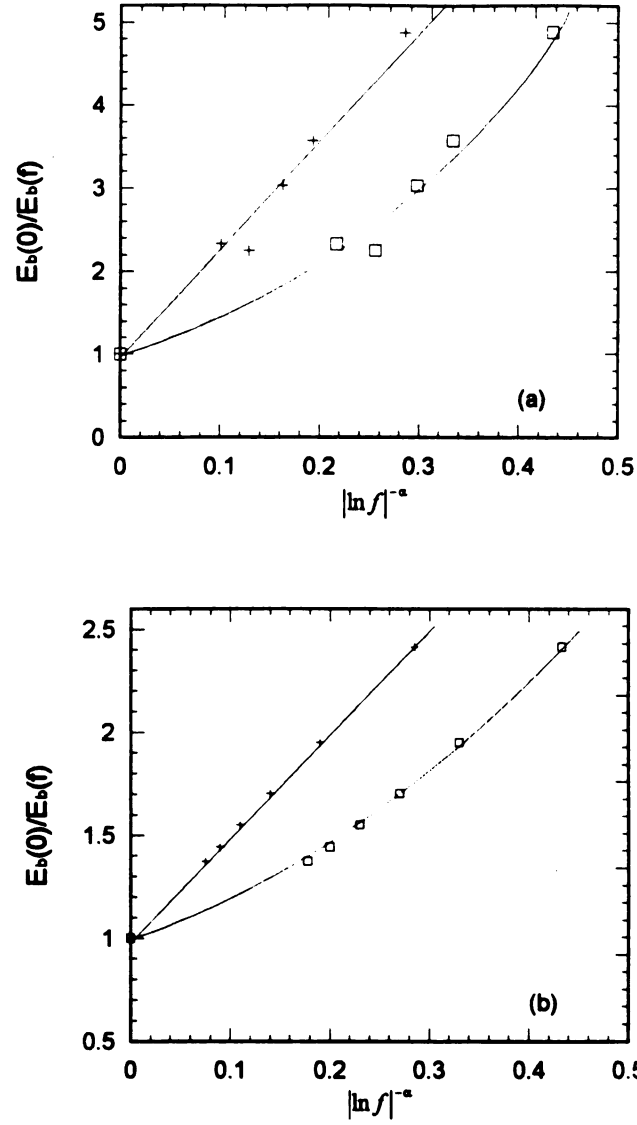


Fig.2.4: A test of Eq.(2.2.5) with $\alpha=3/2(+)$ and $\alpha=1(\square)$. (a) Experimental data same as that in Fig.2.3(a). (b) Numerical simulation data same as that in Fig.2.3(b). The full curves are a guide to the eye.

Bibliography

- [1] P.M.Duxbury, P.D.Beale and P.L.Leath, Phys. Rev. Lett. **57**, 1052(1986)
- [2] P.M.Duxbury, P.L.Leath and P.D.Beale, Phys. Rev. B **36**, 367(1987)
- [3] P.D.Beale and P.M.Duxbury, Phys. Rev. B **37**, 2785(1988)
- [4] Y.S.Li and P.M.Duxbury, Phys. Rev. B **40**, 4889(1989)
- [5] P.M.Duxbury, P.D.Beale, H.Bak and P.A.Schroeder, J. Phys. D. Appl. Phys. **23**,
1546(1990)
- [6] R.W.Coppard, J.Bowman, R.T.Rakowski, R.T.Durham and S.M.Rowland, 3rd
International Conference on Conduction and Breakdown in Solid Dielectrics. 1989

Chapter 3

Comparison of capacitance and dielectric breakdown

3.1 Introduction

Capacitance and dielectric breakdown experiments were aimed at investigating the effect of a conducting defect in an insulating background. The resulting behaviors are different because breakdown fields are related to the extreme moments of the local field distribution, while capacitance is related to the second moment of this distribution.[1] For this reason the statistics of capacitance are described by the central limit form while the statistics of dielectric breakdown fields obey the extreme statistics. The detailed explanations of the differences will be given. We will discuss the forms of statistical distribution functions, i.e., the conventional Weibull distribution and the modified Gumbel distribution. To distinguish between them we made 300 paraffin wax discs and tested them for their dielectric strengths. Experimental results and the numerical data show that the modified Gumbel distribution gives a better fit to the data than does the Weibull distribution.

3.2 Local field distribution

Fig.3.1 shows the difference between the low loading behavior of the dielectric breakdown field, and that of the capacitance. It is seen that the experimental data is qualitatively similar to the numerical data. From both the experimental and numerical data we see that the dielectric breakdown field has much stronger defect sensitivity at low loading than does the capacitance.

This difference may be understood from the study of the local field distribution, $D(v)$. $D(v)$ is the probability that on application of an external voltage V_0 , the voltage across a small region of fixed size and orientation inside the sample is v . If the sample is uniform, the field everywhere inside sample would be the same and $D(v)$ would have a simple delta function form, but $D(v)$ broadens in the presence of disorder. If we can determine the local field distribution function, $D(v)$ then we have obtained all possible information about local electric field fluctuations. We usually cannot determine $D(v)$ but we can often obtain information about the moments of v . The m th moment of v is defined[2]

$$\langle v^m \rangle = \sum_i v_i^m D(v). \quad (3.2.1)$$

In a bond percolation model the capacitance may be related to $D(v)$ as[3]

$$2 \times \text{Energy} = CV_0^2 = N \int c_b v^2 D(v) dv, \quad (3.2.2)$$

where C is the effective capacitance of the system, V_0 is the applied voltage, c_b is the capacitance of an insulating bond, v is the voltage across a bond and N is the total number of bonds in the lattice. In models where c_b is a constant, C may be found from

$$C = Nc_b \langle v^2 \rangle / V_0^2. \quad (3.2.3)$$

Thus the effective capacitance is related to the second moment of $D(v)$.

On the other hand from Eq.(3.2.1) the maximum bond voltage in a system may be written,

$$v_{\max} \sim \lim_{m \rightarrow \infty} \langle v^m \rangle^{1/m}. \quad (3.2.4)$$

We call $\langle v^m \rangle_{m \rightarrow \infty}^{1/m}$ the extreme moment.

In terms of v_{\max} Eq.(2.2.5) can be rewritten as

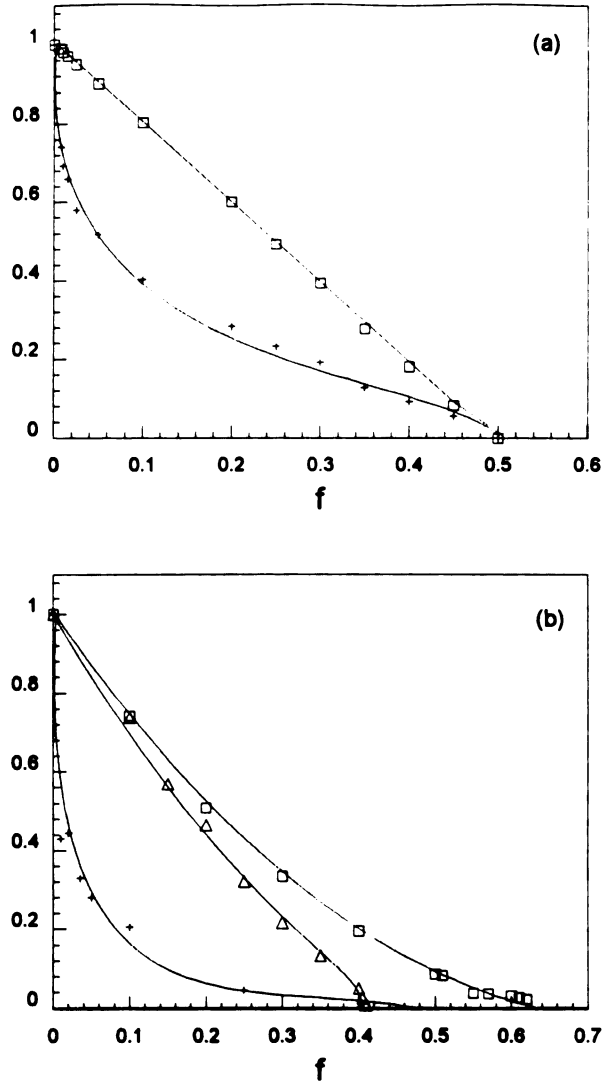


Fig.3.1: The capacitance ratio $C(0)/C(f)$, (\square and Δ) and the dielectric breakdown field ratio $E_b(f)/E_b(0)$, (+). (a) The results calculated using the square lattice dielectric breakdown model. Each point is an average over at least 50 configurations of 100×100 lattices[3]. (b) Experimental results on samples of paraffin wax containing stainless steel balls(\square) and copper particles(Δ). The full curves are a guide to the eye.

$$\begin{aligned} E_b(f)/E_b(0) &\sim E_{np}(0)/E_{np}(f) \\ &\sim V_0/(Lv_{\max}). \end{aligned} \quad (3.2.5)$$

From the Eqs.(3.2.2) through (3.2.5) the dielectric constant is related to the second moment of the local electric field and the dielectric breakdown field is related to the very high moment of the local electric field.

One of the possible technological applications of these measurements concerns the non destructive testing of a component for dielectric breakdown by measuring capacitance. Since the capacitance and dielectric breakdown depend on different moment of the local field distribution, the dependence on particle concentration will be different. Once the results of Fig.3.1 are established, then for a given sample size a measurement of the capacitance can be used to predict what the corresponding breakdown voltage would be.

3.3 Statistics

The statistics applicable to a given series of measurements depends on the moments associated with the measurement. Capacitance depends on the low moments of the local field distribution. For such a quantity sample to sample variability obeys the central limit form[2]. The central limit theorem tells us that if we have a large number of experiments which measure some random variable, X , then the probability distribution of the average of all the measurements approaches a Gaussian regardless of the form of the distribution for X itself. Hence in the case of the dielectric constant

$$P(\varepsilon_N) = \exp\left(-N[\varepsilon_N - \varepsilon_\infty]^2/\sigma^2\right), \quad (3.3.1)$$

where ε_N is the dielectric constant of a sample of size N , ε_∞ is the dielectric constant of an infinite sample and σ depends on disorder and for example diverges near the percolation point.

Since the dielectric breakdown field depends on the highest moments of the electric field, it does not obey the central limit theorem. The statistics of the dielectric breakdown

field are described by the extreme distributions[3-7]. In extreme statistics the cumulative distribution is more convenient than the differential distribution. This experimental distribution is shown in Fig.3.2. $C(E)$ is the probability that a sample will fail when an electric field E is applied to it. The Weibull distribution is most often used in fitting breakdown distributions in engineering applications of materials.[8] It is given by

$$C(E) = 1 - \exp\left(-N(E/E_0)^m\right), \quad (3.3.2)$$

where E_0 and m are constants. This expression for $C(E)$ gives a straight line of gradient m if $\ln[-\ln(1 - C(E))/N]$ is plotted against $\ln E$.

More generally we assume that there are unspecified defects in a sample. The larger the defect appearing in a sample, the lower the breakdown voltage will be. The failure statistics is therefore based on the probability of the larger defects occurring i.e., on the distribution at the extreme or large defects. For an example which does not directly apply to the pure paraffin samples, we consider the case where steel particles form the defects. In this case the smallest breakdown voltage is associated with the largest clusters and the statistical distribution of breakdown voltage will depend on the distribution of clusters at the large cluster extreme. If the distribution at extreme sizes is exponential one gets the Gumbel form[9]

$$C(E) = 1 - \exp\left(-cN \exp(-kE_0/E)\right), \quad (3.3.3)$$

where c and k are constants weakly dependent on the steel particle concentration. This type of statistic gives a straight line on a plot of $\ln[-\ln(1 - C(E))/N]$ against $1/E$.

For the purpose of comparison of these statistics 300 pure paraffin discs were tested. Fig.3.2 shows the cumulative failure distribution. Plots of $-\ln[-\ln(1 - C(E))/N]$ against $1/E$ and $\ln E$ are shown in Fig.3.3 to test the two statistical forms. It is immediately clear that neither form fits the whole range of values. The plots are therefore divided into two regions, high and low breakdown fields. In the low breakdown field region χ^2 values are 0.088 for the Weibull form and 0.129 for the Gumbel form. In the high breakdown field region χ^2 values are 1.291 for the Weibull form and 0.905 for the Gumbel form. In other

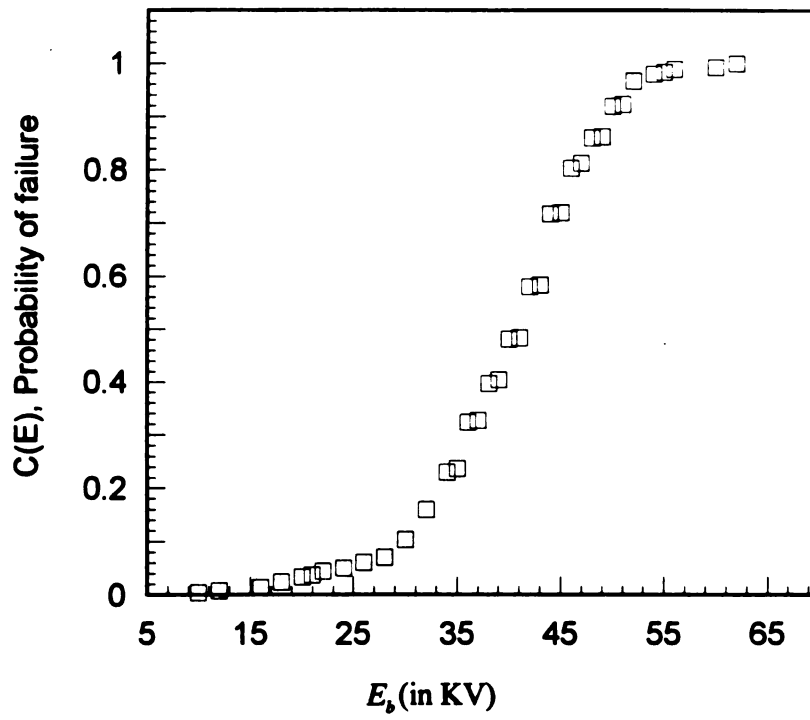


Fig.3.2: A cumulative probability of failure of paraffin discs against breakdown voltage.

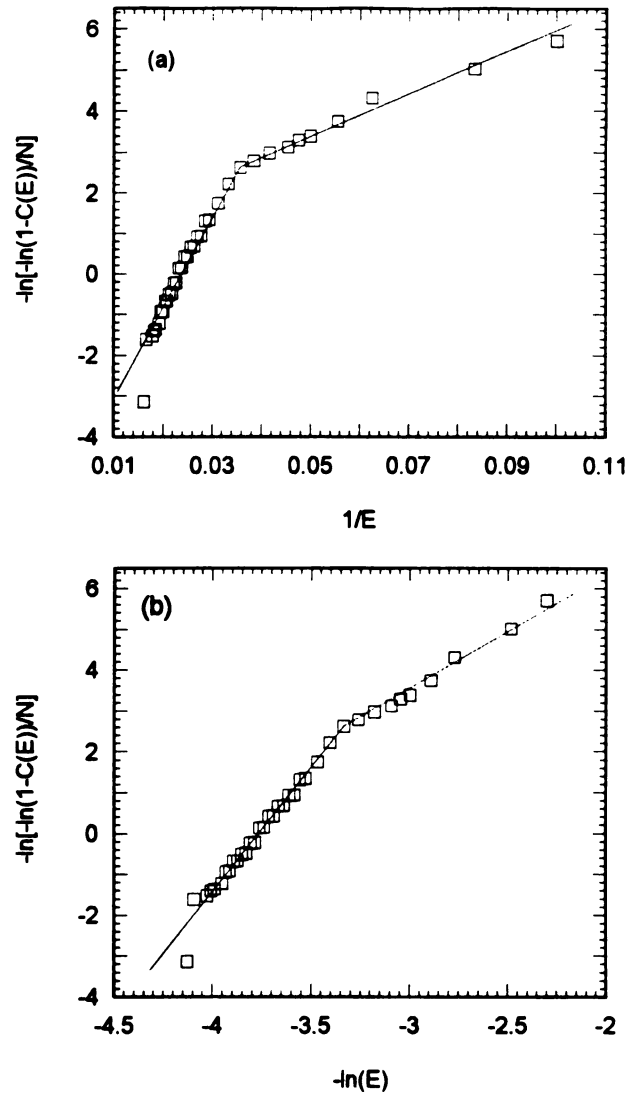


Fig.3.3: Tests of breakdown statistics. (a) If the modified Gumbel distribution (Eq.(3.3.3)) is correct the data as plotted here should be linear; (b) If the Weibull distribution (Eq.(3.3.2)) is correct this way of plotting the data should yield a linear relationship. The full curves are a guide to the eye. The data are from 300 samples of pure paraffin(0.3mm thick).

words, Weibull form is more appropriate than Gumbel form in the low breakdown field region and the converse is true in the high breakdown field region. The separate linear fits suggest that there are two different kinds of breakdown process. A similar plot has been presented by Fischer and Nissen for breakdown measurements in polyethylene using a ramping voltage, and in these data there is also a clear indication of two processes.[10] They suggest that the higher-gradient Weibull plot at high electric fields was intrinsic breakdown and the lower-gradient tail was considered to arise from macroscopic imperfections in the sample and termed technological breakdown.

In our experiments both distribution forms gave very good fits. 300 failures is a large sample set for this type of test. However, in order to differentiate between the two statistics at least 1000 failures would be required.[11]

Bibliography

- [1] Y.S.Li and P.M.Duxbury, Phys. Rev. B **40**, 4889(1989)
- [2] L.E.Reichl, A Modern Course in Statistical Physics(1980)(Austin, TX, University of Texas Press)
- [3] P.M.Duxbury, P.D.Beale, H.Bak and P.A.Schroeder, J. Phys. D: Appl. Phys. **23**, 1546(1990)
- [4] P.M.Duxbury and P.L.Leath, J. Phys. A: Math. Gen. **20**, L411(1987)
- [5] R.W.Coppard, L.A.Dissado, S.M.Rowland and R.Rakowski, J. Phys.: Condens. Matter. **1**,3401(1989)
- [6] R.M.Hill and L.A.Dissado, J. Phys. C: Solid State Phys., **16**, 4447(1983)
- [7] S.M.Rowland, R.M.Hill and L.A.Dissado, J. Phys. C: Solid State Phys. **19**, 6263(1986)
- [8] W.Weibull, J. Appl. Mech. **18**, 293(1951)
- [9] E.J.Gumbel, Statistics of Extremes(1958)(New York: Columbia University)
- [10] P.H.H.Fischer and K.W.Nissen, IEEE Trans. Elec. Ins. EI-11,37(1976)
- [11] P.M.Duxbury, P.L.Leath and P.D.Beale, Phys. Rev. B **36**, 367(1987)

Chapter 4

Dielectric properties of colloidal suspensions - Theoretical reviews

4.1 Introduction

Large values of the dielectric constant have been observed with colloidal solutions and biological cells at low frequencies[1]. H.P.Schwan and co-workers reported very large dielectric constants of polystyrene spheres (size $\sim .1\mu\text{m}$) suspended in KCl solution[2]. The dielectric constant they observed is about 1000 at frequencies below 1KHz (See Fig.4.1). This is remarkable since the dielectric constant of KCl solution is about 80 and that of the dry polystyrene is about 3.

There has been a lot of theoretical attempts to explain the dielectric properties of colloidal suspensions[3-9]. There are two starting points for the theoretical description since they occupy an intermediate position between true solutions and coarse disperse systems. The first one is to extend the theories of homogeneous mixtures and solutions and the second is to extend the macroscopic theories on the polarization of the interface between two media. Two theories are reviewed and discussed.

4.2 Complex permittivity

It is customary to express the dielectric properties of materials in terms of the complex permittivity which is defined by

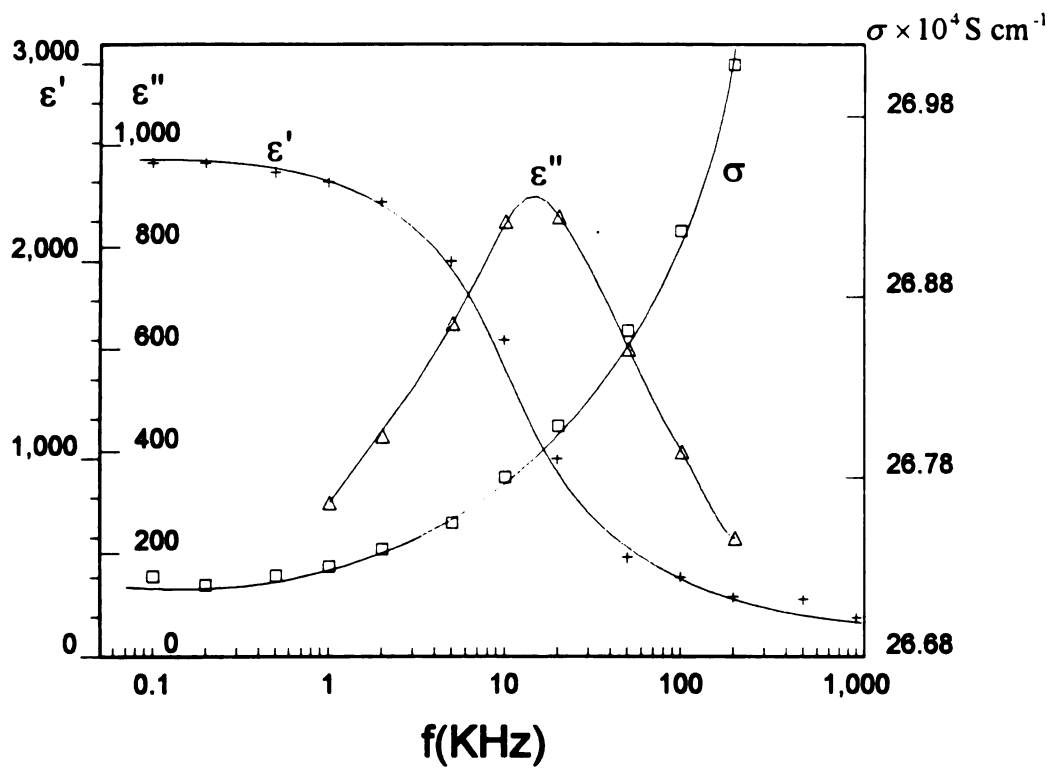


Fig.4.1 : Real (ϵ') and imaginary (ϵ'') parts of the complex dielectric constant of a suspension of polystyrene particles as a function of frequency: particle diameter $0.188\mu\text{m}$, particle concentration 30%.

$$\epsilon^* = \epsilon' - i\epsilon'', \quad (4.2.1)$$

where ϵ' and ϵ'' are the real and imaginary part of the permittivity, and $i = \sqrt{-1}$. The electrical behavior of a material may be expressed in terms of the admittance Y , i.e.,

$$Y = G + i\omega C, \quad (4.2.2)$$

where G and C are the conductance and the capacitance. For a plane parallel capacitor with a dielectric material the conductance and the capacitance are given by

$$G = \sigma \frac{A}{d} \text{ and } C = \epsilon_0 \epsilon_r \frac{A}{d} = \epsilon \frac{A}{d}, \quad (4.2.3)$$

where A is the area of the electrodes and d is their separation, σ is the conductivity and ϵ_0 and ϵ_r are the permittivity of the free space and the relative permittivity respectively.

Therefore for a unit cube Eq.(4.2.2) becomes

$$Y = \sigma + i\omega\epsilon. \quad (4.2.4)$$

The complex permittivity and the unit admittance are related by

$$Y = i\omega\epsilon^*. \quad (4.2.5)$$

Comparing of Eqs.(4.2.4) and (4.2.5) gives that the following relations hold,

$$\epsilon' = \epsilon, \quad (4.2.6)$$

$$\epsilon'' = \sigma/\omega. \quad (4.2.7)$$

The quantity ϵ'' is called the dielectric loss since it is associated with the energy loss during the relaxation process. Many polarization processes are characterized by a finite relaxation time. At sufficiently high frequencies, when the period of the field is commensurable with the relaxation time, the phase shift between the polarization and the field becomes perceptible and manifests itself in dielectric loss.

4.2a Debye Equations

The Debye theory is concerned with a gas of non interacting permanent dipoles. An applied electric field tends to aline them. At the same time thermal motion acts to restore

the original disorder. In the absence of an external field a group of independent permanent dipoles in a liquid or solid are distributed randomly in angle. When they are subject to an external field each dipole rotates to line up in the direction of the field. They will be completely polarized after a long time. As soon as the field is turned off the polarization decays exponentially as the angular distribution becomes random, i.e.,

$$P = P_0 e^{-t/\tau}, \quad (4.2.8)$$

where τ is called the relaxation time and is independent of time. From this assumption the dielectric constant of the substance can be derived as[10]

$$\epsilon^*(\omega) = \epsilon_\infty + \frac{\epsilon_s - \epsilon_\infty}{1 + i\omega\tau}. \quad (4.2.9)$$

Separating the real and imaginary parts we find

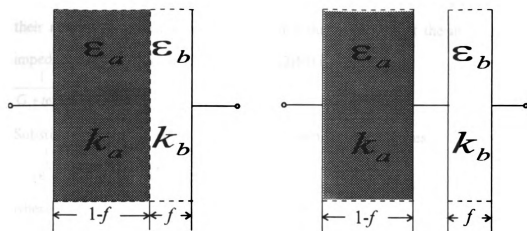
$$\epsilon' = \epsilon_\infty + \frac{\epsilon_s - \epsilon_\infty}{1 + \omega^2\tau^2}, \quad (4.2.10a)$$

$$\epsilon'' = \frac{(\epsilon_s - \epsilon_\infty)\omega\tau}{1 + \omega^2\tau^2}, \quad (4.2.10b)$$

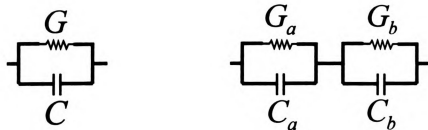
where ϵ_s and ϵ_∞ are the dielectric constants at very low frequency and high frequency, respectively. These equations are called Debye equations since they were established by Debye and subsequently have been applied to many substances. Their behavior is very similar to that illustrated in Fig.4.1 though the mechanism behind the Schwan et al. measurements of Fig.4.1 may be quite different.

4.3 Maxwell-Wagner theory

The dielectric dispersion observed in heterogeneous systems was explained by Maxwell from the point of impedance theory[11]. The basis of this model is illustrated in Fig. 4.2(a) which depicts a parallel plate capacitor filled by layers of two materials a and b. ϵ_a and ϵ_b are the real part of the dielectric constants of material a and b, k_a and k_b are



(a)



(b)

Fig. 4.2 : (a) The model of a binary heterogeneous system. (b) The equivalent circuit of the system.

their respective conductivities and f is the volume fraction of the material b. The total impedance of the equivalent circuit (Fig.4.2(b)) is

$$\frac{1}{G + i\omega C} = \frac{1}{G_a + i\omega C_a} + \frac{1}{G_b + i\omega C_b}. \quad (4.3.1)$$

Substituting Eqs.(4.2.3), (4.2.4) and (4.2.5) into Eq.(4.3.1) gives

$$\frac{1}{\epsilon^*} = \frac{1}{\epsilon_a^*} (1 - f) + \frac{1}{\epsilon_b^*} f, \quad (4.3.2)$$

where

$$\epsilon_a^* = \epsilon_a + \frac{k_a}{i\omega}, \quad (4.3.3a)$$

$$\epsilon_b^* = \epsilon_b + \frac{k_b}{i\omega}. \quad (4.3.3b)$$

Using Eqs.(4.3.3), Eq.(4.3.2) can be rewritten by

$$\epsilon^* = \epsilon_h + \frac{\epsilon_l - \epsilon_h}{1 + i\omega\tau} + \frac{k_l}{i\omega}, \quad (4.3.4)$$

where

$$\epsilon_h = \frac{\epsilon_a \epsilon_b}{\epsilon_b + f(\epsilon_a - \epsilon_b)}, \quad (4.3.5a)$$

$$\epsilon_l = \frac{\epsilon_a k_b^2 + f(\epsilon_b k_a^2 - \epsilon_a k_b^2)}{[k_b + f(k_a - k_b)]^2}, \quad (4.3.5b)$$

$$\tau = \frac{\epsilon_b + f(\epsilon_a - \epsilon_b)}{k_b + f(k_a - k_b)}, \quad (4.3.5c)$$

$$k_l = \frac{k_a k_b}{k_a + f(k_a - k_b)}. \quad (4.3.5d)$$

The frequency dependent behavior of Eq.(4.3.4) is illustrated in Fig.4.3. The dielectric phenomena of this system are associated with the polarization at the interface between the dielectric layers. The polarization is due to charges which are piled up at the boundary of the layer in the external electric field. The theory predicts a high value of ϵ' (>300 in this calculation) which decreases rapidly at frequencies where the charge transfer cannot keep up with the applied frequency.

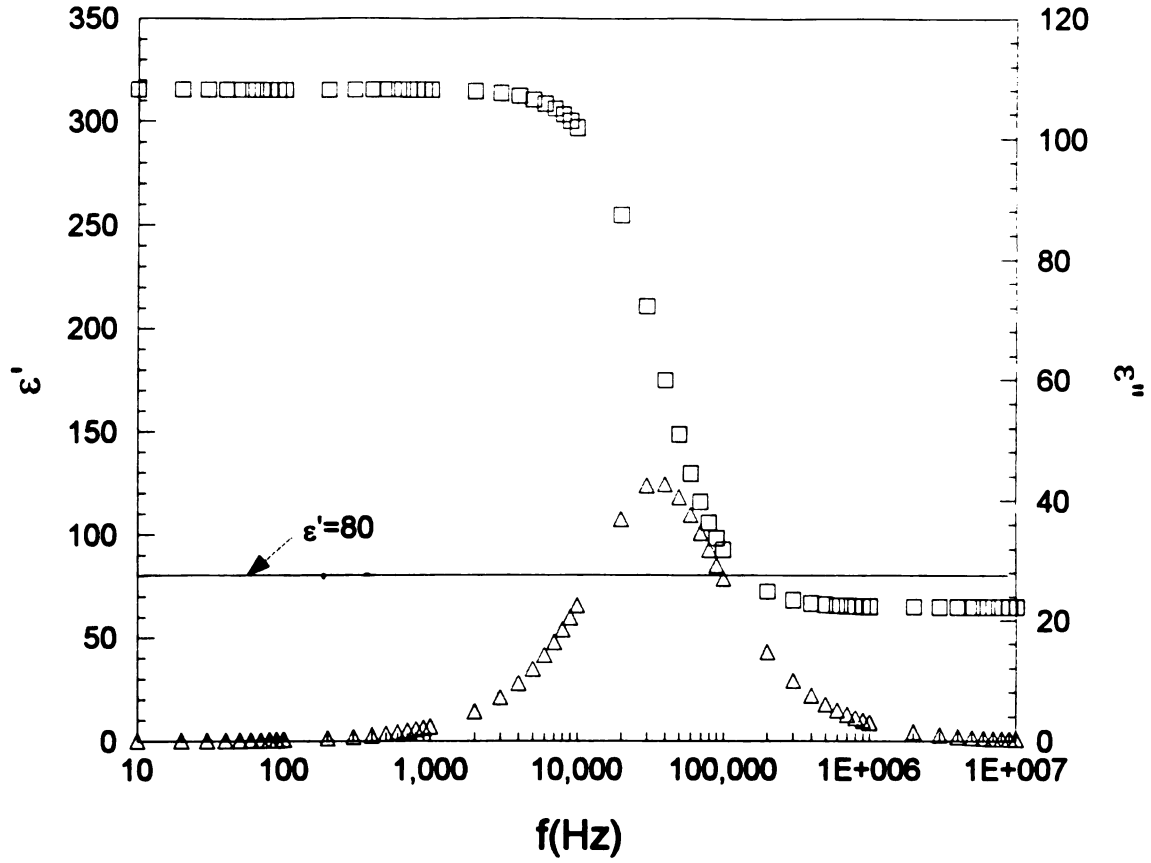


Fig.4.3: Real part(\square) and imaginary part(Δ) of dielectric behavior of Eq.(4.3.4). In this plot $\epsilon_s = 80\epsilon_0$, $\epsilon_b = 2\epsilon_0$, $k_s = 1 \times 10^{-5}$, $k_b = 1.5 \times 10^{-9}$, and $f=3/500$ are used.

Wagner developed a dielectric theory pertaining to this kind of polarization for dilute suspension of spherical particles[12]. Now let's consider an infinite disperse system with complex dielectric constant ϵ_o^* . The spherical particles which have uniform size are distributed evenly and randomly. The distance between them is much larger than the size of each particle so that the interactions can be neglected. Thus the system is polarized in the external electric field only. The induced field due to this polarization at very large distance from the particles can be represented by two methods as illustrated in Fig. 4.4.

For a single particle in an electric field the induced complex dipole potential is given by

$$\varphi^* = d_e^* \frac{\cos \theta}{r^2}. \quad (4.3.6)$$

Here d_e^* is the complex dipole moment of a spherical particle of radius a . First let's look at the spherical volume of radius b containing a number of particles (See Fig.4.4(a)). Each particle is polarized only by the external field since the interaction of the particles are negligible. Therefore the induced potential at sufficiently large distance from the sphere is just the sum of the potentials induced by each particle and given by

$$\varphi_\infty^* = \frac{4}{3} \pi b^3 N \varphi^*, \quad (4.3.7)$$

where N is the number of particles per unit volume. Furthermore the sphere of radius b can be treated as a homogeneous spherical body which is characterized by the effective complex dielectric constant $\bar{\epsilon}^*$ (See Fig.4.4(b)). The potential due to the polarization of this sphere is given by

$$\varphi_\infty^* = d_\Sigma^* \frac{\cos \theta}{r^2}. \quad (4.3.8)$$

Here d_Σ^* is the complex dipole moment of a sphere of radius b . When a sphere of dielectric constant ϵ_1 is embedded in a medium with dielectric constant ϵ_0 in an external electric field E_0 solving Laplace's equation gives the potential outside the sphere, i.e.,

$$\varphi(r, \theta) = -E_0 r \cos \theta + \frac{\epsilon_1 - \epsilon_0}{2\epsilon_0 + \epsilon_1} a^3 E_0 \frac{\cos \theta}{r^2}, \quad (4.3.9)$$

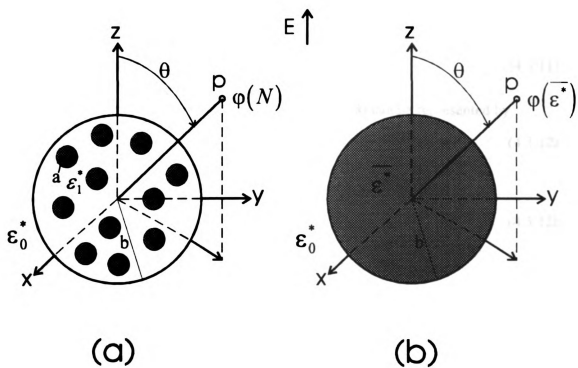


Fig.4.4: Wagner's model for a dilute suspension of spherical particles.

The first term describes the potential of the applied uniform field, while the second term is associated with the change in potential due to the polarization of the sphere. The potential generated by a permanent dipole oriented along an axis $\theta=0$ in a medium with dielectric constant ϵ_0 is

$$\varphi = d_\epsilon \frac{\cos\theta}{r^2}. \quad (4.3.10)$$

Comparing the Eqs.(4.3.9) and (4.3.10) we obtain

$$d_\epsilon = \frac{\epsilon_1 - \epsilon_0}{2\epsilon_0 + \epsilon_1} a^3 E_0. \quad (4.3.11)$$

In analogy with this d_ϵ^* in Eq.(4.3.6) and d_Σ^* in Eq.(4.3.8) can be represented by

$$d_\epsilon^* = \frac{\epsilon_1^* - \epsilon_0^*}{2\epsilon_0^* + \epsilon_1^*} a^3 E_0 \quad (4.3.12a)$$

and

$$d_\Sigma^* = \frac{\overline{\epsilon^*} - \epsilon_0^*}{2\epsilon_0^* + \overline{\epsilon^*}} a^3 E_0. \quad (4.3.12b)$$

From Eqs.(4.3.7), (4.3.8) and (4.3.9) we deduce

$$d_\Sigma^* = \frac{4}{3} \pi b^3 N d_\epsilon^*. \quad (4.3.13)$$

Combining Eqs. (4.3.12) and (4.3.13) we obtain

$$\frac{\overline{\epsilon^*} - \epsilon_0^*}{2\epsilon_0^* + \overline{\epsilon^*}} = f \frac{\epsilon_1^* - \epsilon_0^*}{2\epsilon_0^* + \epsilon_1^*}, \quad (4.3.14)$$

where $f = \frac{4}{3} \pi a^3 N$ is the volume fraction of the dispersed particles. By solving

Eq.(4.3.14) for $\overline{\epsilon^*}$ we derive the Wagner formula, i.e.,

$$\overline{\epsilon^*} = \epsilon_0^* \frac{2\epsilon_0^* + \epsilon_1^* + 2f\epsilon_0^*(\epsilon_1^* - \epsilon_0^*)}{2\epsilon_0^* + \epsilon_1^* - f(\epsilon_1^* - \epsilon_0^*)}. \quad (4.3.15)$$

After substituting the expressions

$$\epsilon_0^* = \epsilon_0 - i \frac{k_0}{\omega},$$

$$\epsilon_1^* = \epsilon_1 - i \frac{k_1}{\omega},$$

we obtain

$$\overline{\epsilon^*} = \overline{\epsilon_h} + \frac{\overline{\epsilon_l} - \overline{\epsilon_h}}{1 + i\omega\tau} - i \frac{\overline{k_l}}{\omega}, \quad (4.3.16)$$

where

$$\tau = \frac{2\varepsilon_0 + \varepsilon_1 + f(\varepsilon_0 + \varepsilon_1)}{2k_0 + k_1 + f(k_0 - k_1)}, \quad (4.3.17a)$$

$$\overline{\varepsilon_h} = \varepsilon_0 \frac{2\varepsilon_0 + \varepsilon_1 - 2f(\varepsilon_0 - \varepsilon_1)}{2\varepsilon_0 + \varepsilon_1 + f(\varepsilon_0 - \varepsilon_1)}, \quad (4.3.17b)$$

$$\overline{\varepsilon_l} - \overline{\varepsilon_h} = \frac{9(\varepsilon_0 k_1 - k_0 \varepsilon_1)^2 f(1-f)}{[2\varepsilon_0 + \varepsilon_1 + f(\varepsilon_0 - \varepsilon_1)][2k_0 + k_1 + f(k_0 - k_1)]^2}, \quad (4.3.17c)$$

$$\overline{k_l} = k_0 \frac{2k_0 + k_1 - 2f(k_0 - k_1)}{2k_0 + k_1 + f(k_0 - k_1)}. \quad (4.3.17d)$$

These results are very similar to Maxwell theory, and yield behaviour similar to that in Fig.4.3.

4.4 Thin double layer approximation

The polystyrene spheres have terminating COOH or SO₄ groups in their surface. In solution these groups ionize(hydrolize), leaving usually a negatively charged sphere(radius a) surrounded by positive(counter) ions which create the electrical double layer(thickness δ) as illustrated in Fig. 4.5(a). Whereas the Maxwell-Wagner effect arises principally from induced charges on the surface, several people have suggested that the polarization of the double layer is responsible for the high values of the real part of the dielectric constant at low frequency[7,9,13,14]. Of these we describe the theory of Chew and Sen. The details of their theory are given in Appendix 2. Here we emphasize the physics of what is happening rather than the mathematics.

A consequence of the Chew-Sen theory is that for $r > a + \delta$, the system is electrically neutral but there is a diffusion cloud in which both charge densities vary exponentially with distance. The application of an alternating electric field results in oscillatory circumferential conduction currents within the double layer plus radial diffusion

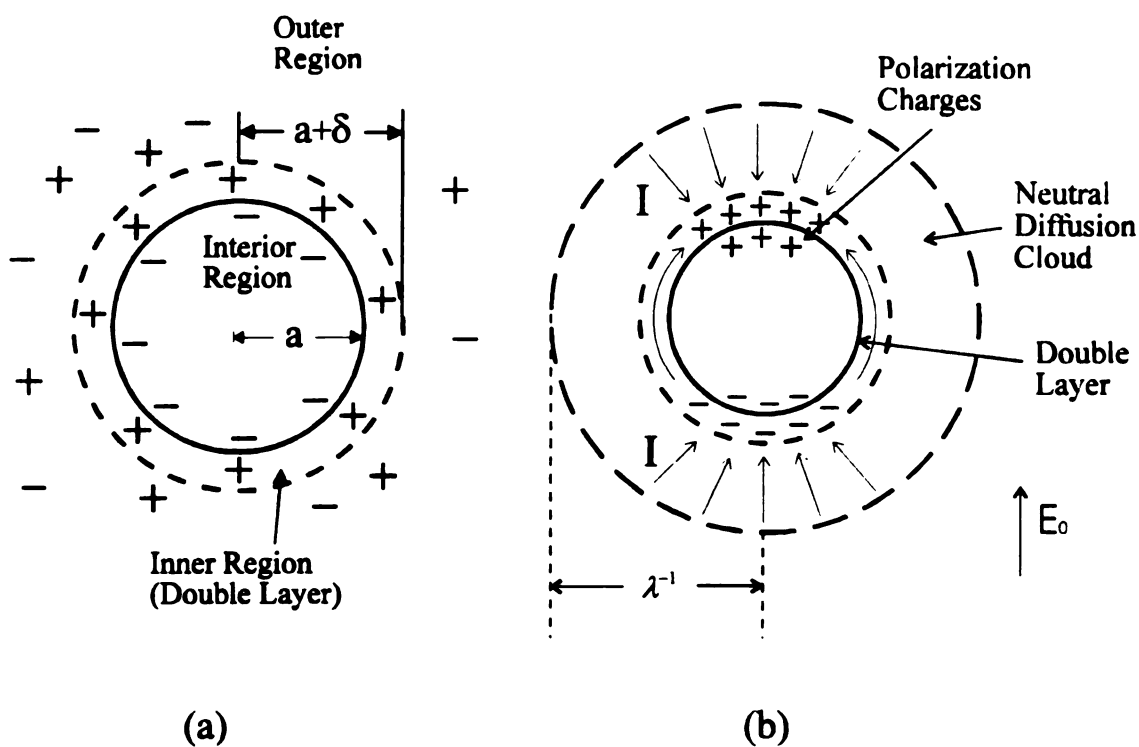


Fig.4.5: (a) A negatively charged particle in ionic solution acquires positively charged counterions in the absence of an external electric field. (b) In the presence of an external electric field E_0 the charge distribution in the double layer changes and polarization charges develop within the particle.

currents from the diffusion cloud(Fig.4.5(b)). The circumferential currents are conduction currents which do not give rise to increased dielectric constant. On the other hand the radial current has the phase relations associated with a displacement current and is responsible for the dielectric enhancement.

The mathematical steps are as follows. The potential in the electrolyte solution surrounding a colloid particle is governed by the Poisson-Boltzmann equation. Chew and Sen set up equations for the inner $a < r < a + \delta$ and outer $r > a + \delta$ regions where δ is the width of the double layer. The solution of the potential equations is obtained by matching at the boundaries order by order in (δ/a) . The dielectric constant becomes large when the induced dipole moments and potential develop an out of phase component. This does not occur in the zeroth and first order approximations. Solving the equation by perturbation method gives the potential, i.e.,

$$\psi = -e_0 r \cos\theta + (Pe_0/r^2)a^3 \cos\theta, \quad (4.4.1)$$

which is similar to Eq.(4.3.9). Here $e_0 = E_0 e / k_b T$. The second term describes the effect of the induced dipole moment of a particle. The zeroth order solution is

$$\psi^{(0)} = -e_0 r \cos\theta - \frac{1}{2} e_0 (a^3/r^2) \cos\theta. \quad (4.4.2)$$

Therefore the induced dipole moment is $P^{(0)} = -\frac{1}{2}$ which is real, resulting in an induced current which is purely resistive and there is no enhancement in the dielectric constant.

In the first order of (δ/a) , a radial current $j_{\pm X}$ appears in the inner region. It is given by

$$j_{\pm X}^{(1)} \sim \pm 3e_0 D N_0 \cos\theta \left[X \mp \frac{4t}{1 \pm t} \right], \quad X = \frac{r-a}{\delta} \quad (4.4.3)$$

where $t = \tanh(\Psi_0/4)$, Ψ_0 is the potential at the surface of the particle, and D and N_0 are the diffusion coefficient and the the equilibrium ionic densities in the absence of the charged particles. The + and - signs refer to + and - ions which have different distributions across the inner region.

The wide difference in amplitudes of $j_{+X}^{(1)}$ and $j_{-X}^{(1)}$ implies that these ionic currents cannot be carried away from the inner region into the outer region by conduction current alone, since conduction gives rise to ionic currents which are equal and opposite. Hence, we expect a diffusion cloud of ions in the outer region which is induced by the inequality in amplitudes of $j_{\pm X}^{(1)}$.

The charge density outside the double layer determines the diffusion process. The charge density of this diffusion cloud is given by

$$n_{\pm} \sim e^{-\lambda(r-a)}, \quad (4.4.4)$$

where $\lambda = (1-i)\sqrt{\omega/2D}$. The diffusion cloud is neutral and has a size $\sim 1/\lambda$. Fig.4.5 illustrates the change of charge distribution in the presence of an external electric field. This neutral diffusion cloud gives the normal component of the current and induces a dipole moment. The induced dipole moment is pure real up to 1st order in (δ/a) . The first out of phase term for P appears in the second order of (δ/a) and is given by

$$P \sim -\frac{1}{2} + \left(\frac{\delta}{a}\right) \frac{6t^2}{1-t^2} + \left(\frac{\delta}{a}\right)^2 \left[-\frac{3}{4} \frac{i\omega}{D} \frac{\epsilon_p}{\epsilon'} a^2 + 6 \ln(1-t^2) - \frac{24t^2}{(1-t^2)^2} \left(t^2 + \frac{1}{\alpha} \right) \right]. \quad (4.4.5)$$

Here $\alpha = \left(1 + \lambda a + \frac{\lambda^2 a^2}{2} \right) / (1 + \lambda a)$.

We may write the Eq.(4.3.14) in terms of P for small f (the volume fraction of dispersed particle), when this is done the effective dielectric constant of an ensemble of spherical particles randomly distributed in a background medium of ϵ_0^* becomes

$$\overline{\epsilon^*} = \epsilon_0^* (1 + 3fP). \quad (4.4.6)$$

From Eq.(4.4.5) the enhancement comes mostly from the last terms. Therefore Eq.(4.4.6) can be approximated by

$$\overline{\epsilon^*} \sim \left(\epsilon' + i \frac{\sigma}{\omega} \right) \left(1 - 3fF \frac{1}{\alpha} \right), \quad (4.4.7)$$

where

$$F = \left(\frac{\delta}{a}\right)^2 \frac{24t^2}{(1-t^2)^2}. \quad (4.4.8)$$

Hence the condition for enhancement is $t \rightarrow 1$ or $\Psi_0 \gg 1$. This implies that a particle must be highly charged. Furthermore the enhancement comes from the induced out of phase currents which are generated from the diffusion cloud outside the double layer. The bigger the size of the diffusion cloud the larger the enhancement. At high frequency the rapid oscillation of the circumferential current in the double layer does not give time for a diffusion cloud to form outside the double layer. Therefore the induced out of phase current becomes small and the enhancement disappears. The effective dielectric constant is given by

$$\begin{aligned} \bar{\epsilon}'' &\sim -3fF \left(\epsilon' + i \frac{\sigma}{\omega} \right) \frac{1}{\alpha} \\ &= -3fF \frac{1}{(1+\sqrt{\omega\tau})^2} \left[\epsilon' + 2\epsilon'\sqrt{\omega\tau} - \sigma\tau + i \left\{ \epsilon'\omega\tau + \sigma\tau + \frac{\sigma}{\omega} (1+\sqrt{\omega\tau}) \right\} \right], \end{aligned} \quad (4.4.9)$$

where $\tau = \frac{a^2}{2D}$. Fig.4.6 shows the behavior of the effective dielectric constant vs.

frequency. In this plot the following values are used.

$$\Psi_0 = 3.85, N_0 = 2.08 \times 10^{25} \text{ m}^{-3}$$

$$D = 1.97 \times 10^{-5} \text{ cm}^2/\text{sec},$$

$$\epsilon_w = 80\epsilon_0, \epsilon_p = 3\epsilon_0,$$

$$\delta/a = 1/60, a = 0.094\mu \text{ and } f=0.3.$$

In this figure the maximum in ϵ'' occurs at the high frequency $\sim 10^5 \text{ Hz}$. The maximum occurs at frequency $1/\tau$. The frequency of the maximum therefore is expected to be $\propto a^{-2}$.

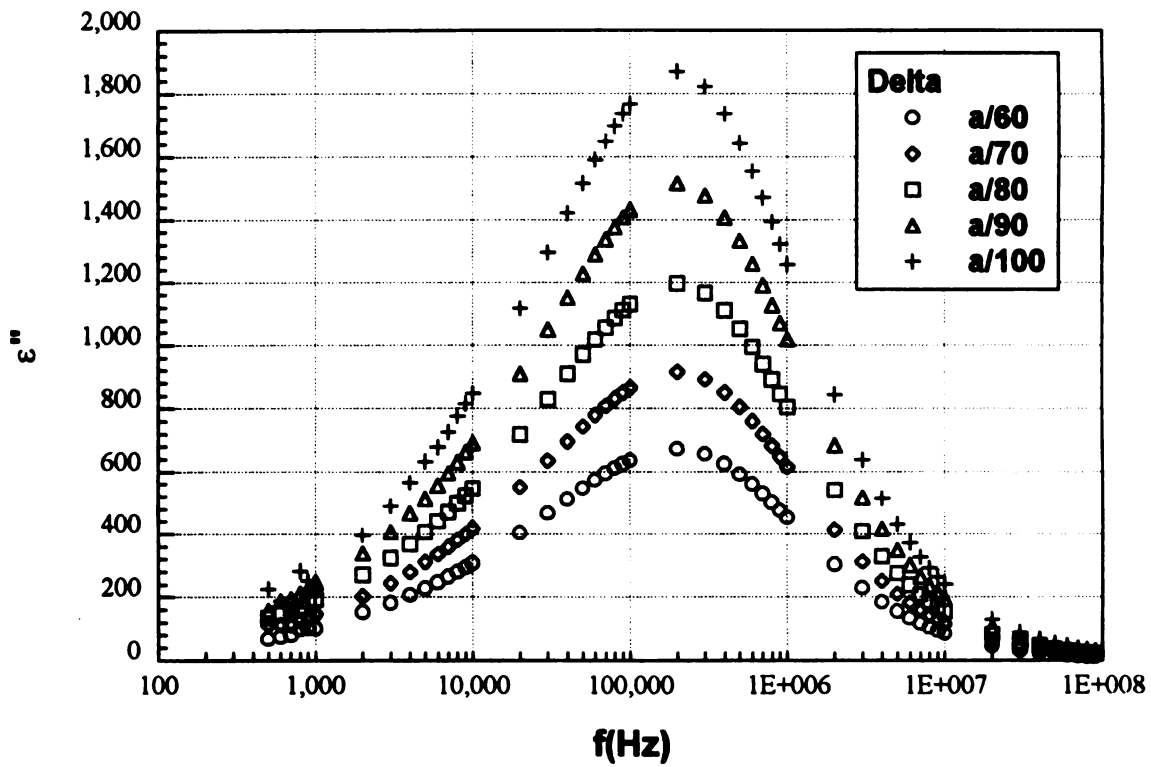
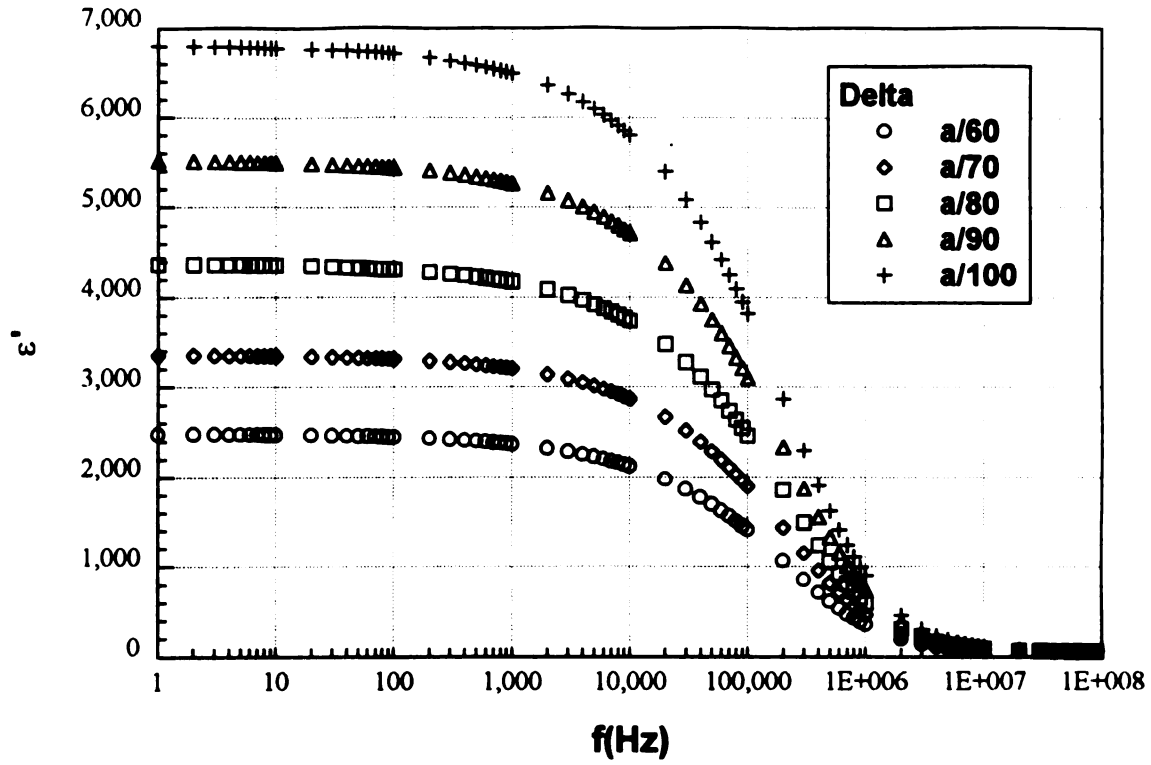


Fig.4.6: Dielectric behavior of Eq.(4.4.9).

Bibliography

1. H.P.Schwan, Advan. Biol. Med. Phys. **5**, 147(1957)
2. H.P.Schwan, G.Schwarz, J.Maczuk and H.Pauly, J.Phys. Chem. **66**, 2626(1962)
3. G.Schwarz, J. Phys. Chem. **66**,2636(1962)
4. K.W.Wagner, Ann. Phys. **5**, 817(1913)
5. J.Lyklema, S.S.Dukhin and V.N.Shilov, J. Electroanal. Chem. **143**, 1(1983)
6. W.C.Chew and P.N.Sen, J. Chem. Phys. **77**, 4683(1982)
7. M.Fixman, J. Chem. Phys. **72**, 5177(1980)
8. J.M.Schurr, J. Phys. Chem. **68**, 2407(1964)
9. E.H.B.Delacey and L.R.White, J. Chem. Soc. Faraday Trans. 2, **77**, 2007(1981)
10. V.V.Daniel, Dielectric Relaxation, Academic Press(1967)
11. J.C.Maxwell, Treatise on Electricity and Magnetism, 1873(Dover, New York 1954)
12. K.W.Wagner, Arch. Elect. **2**, 37(1914)
13. W.C.Chew and P.N.Sen, J. Chem. Phys. **77**, 2042(1982)
14. S.S.Dukhin and V.N.Shilov, Dielectric Phenomena and the Double Layer in Disperse Systems and Polyelectrolytes(Halsted, NY, 1974)

Chapter 5

Dielectric properties of colloidal suspensions - Experimental attempts

5.1 Introduction

Since Schwan and his co-workers presented their results for the dielectric dispersion of dilute suspension of polystyrene microspheres[1], the frequency dependence of the effective dielectric constant has been of great experimental theoretical interest. Many experimental attempts associated with this matter have been reported[2-4]. None have been completely successful.

In this chapter we review and criticize Schwan's experiment which used the long cell arrangement, and introduce other method using a small cell. We compare the pros and cons of both setups using several different electrodes. We point out that the use of platinum black electrodes, which is the conventionally recommended method for reducing electrode effects, is not a good solution to reduce electrode polarization. It turns out that platinum black acts as an insulating layer which gives rise to the Maxwell-Wagner effect. To support this we performed measurements using electrodes covered with insulating scotch tape and obtained similar results.

5.2 Electrode polarization

Electrode polarization is a major source of error in determination of the dielectric properties of ionic solution[5-6]. Fig. 5.1 shows how the polarization of a sample can take place in a parallel plate capacitor[7]. The dielectric material can be polarized by the reorientations of the dipoles along the external field. If the material is nonconducting then the measured dielectric constant gives a measure of this orientation process. If the material has finite conductivity then the ions in the electrolyte accumulate at the electrodes forming an electrical double layer. This phenomenon is called electrode polarization. In a parallel plate capacitor configuration the voltage drop divided by the applied current yields the complex impedance. However, this includes the additional voltage drop at the electrode-electrolyte interface caused by electrode polarization. This is very difficult to measure and predict. The electrode polarization effect becomes large as the frequency is lowered and as the conductivity of the solution is raised. Our measurements in Fig 5.2 illustrate the effect of electrode polarization in materials ranging from very high resistivity transformer oil to a highly conducting 2mM KCl solution. From these results we see that electrode polarization is large in the region 1-100KHz where we anticipate the important results for microsphere suspensions. Eq.(5.3.3) below is qualitatively verified by these results. The various experimental methods outlined below are largely designed to eliminate errors due to electrode polarization.

5.3 Review of Schwan's experiment

In the investigation of the impedance of materials which have high dielectric losses substantial errors due to electrode polarization can occur. Now consider the equivalent circuit in Fig.5.3 in which C_s and R_s are the capacitance and resistance of the sample, C_m and R_m are the measured capacitance and resistance and C_p and R_p are the capacitance and resistance due to electrode polarization[8]. The total impedance is

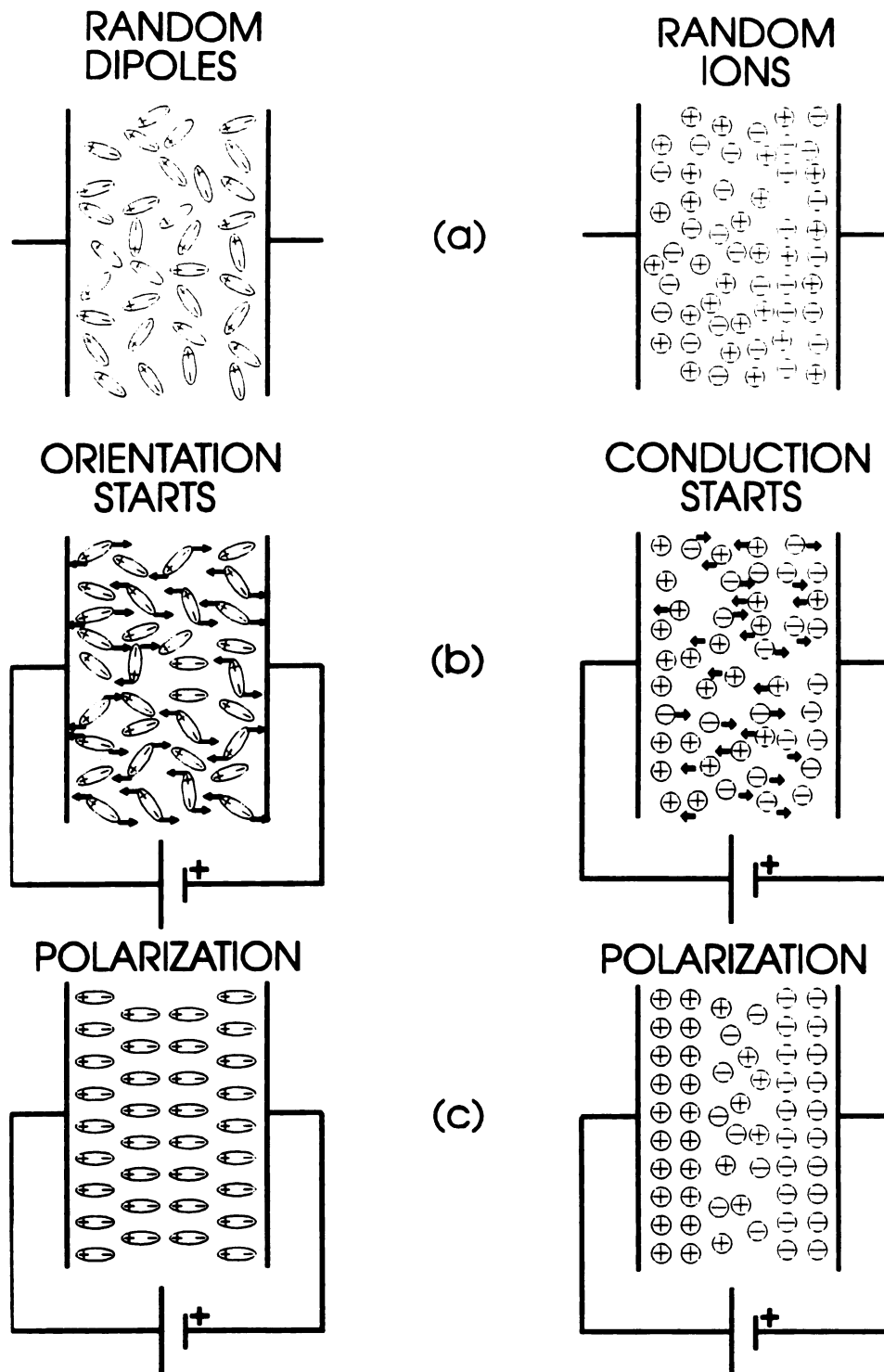


Fig.5.1: Idealized view of the polarization due to dipoles and ions: (a) unpolarized; (b) orientation and conduction begins; (c) fully polarized. In actual materials, both processes can occur simultaneously.

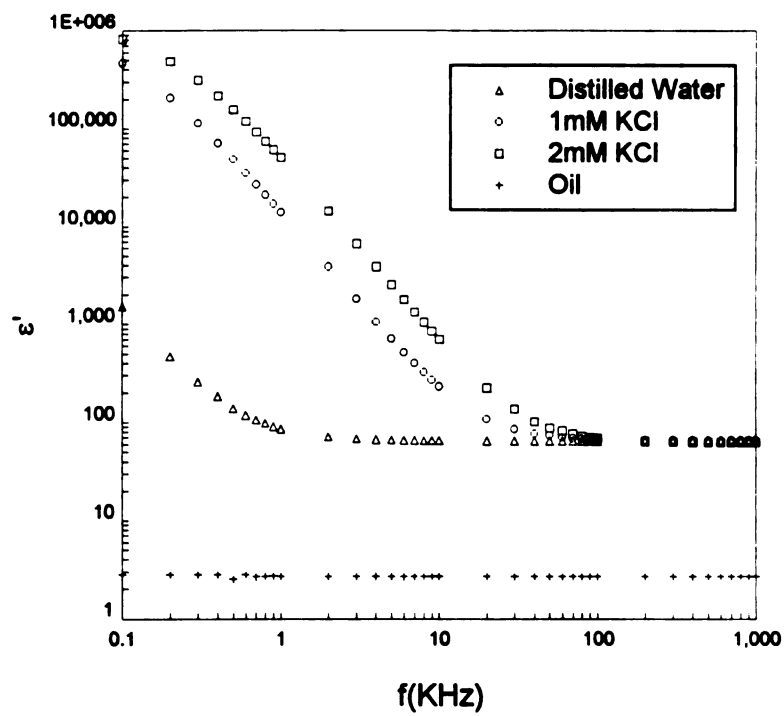
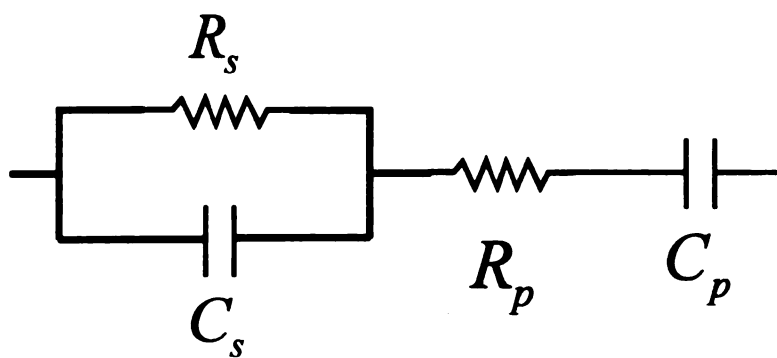
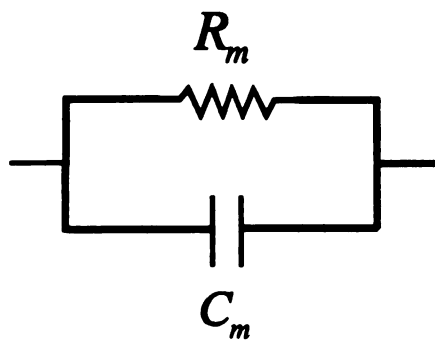


Fig 5.2. The apparent dielectric constants of several liquids which are different in conductivity.



(a)



(b)

Fig. 5.3: (a) Equivalent circuit of dielectric cell. (b) Equivalent circuit of the total measured admittance.

$$\frac{1}{\frac{1}{R_s} + j\omega C_s} + R_p + \frac{1}{j\omega C_p} = \frac{1}{\frac{1}{R_m} + j\omega C_m}, \quad (5.3.1)$$

From Eq.(5.3.1) we can derive that

$$R_m = R_s + R_p + R_s(\omega C_m R_m)^2, \quad (5.3.2)$$

$$C_m = C_s + \frac{1}{\omega^2 C_p R_m^2}. \quad (5.3.3)$$

Many assumptions have been used in these equations, namely $1/\omega C_s \gg R_s$, $R_m \ll 1/\omega C_m$, and $R_s \gg R_p$.

Since the second part of the total capacitance expression increases rapidly as the frequency decreases, it is often impossible to get a correct sample data C_s from the measured capacitance C_m . One way to minimize electrode polarization effects is to use large electrode separation to make R_m large and thereby make C_m and C_s comparable. A cell with large electrode separation is very hard to handle because it is accompanied by large stray field effects. One method of dealing with the electrode polarization problem is as follows[9]. Fig.5.4 shows a schematic diagram of a cylindrical capacitance cell which has very large electrode separation. The teflon cylindrical cell is filled with the sample to be measured. The upper electrode is grounded through the outer metallic cylinder, while the lower electrode is connected in our case to the high terminal of our impedance analyzer. This arrangement is considered as a transmission line with the admittance Y between the points A and B given by

$$Y_0 = \frac{1}{Z} \frac{1 + e^{-2\gamma l}}{1 - e^{-2\gamma l}}, \quad (5.3.4)$$

$$Z^2 = \frac{(R + j\omega L)}{j\omega C}, \quad (5.3.5a)$$

$$\gamma^2 = \frac{(R + j\omega L)}{\omega C}, \quad (5.3.5b)$$

where the characteristic impedance is Z , the resistance per unit length of inner conductor R ; total length of transmission line l ; inductance per unit length L ; capacity between inner and outer cylinder per unit length C ; and propagation constant γ . At low frequencies ωL is very small compared to R . Consequently Eq.(5.3.4) may be rewritten

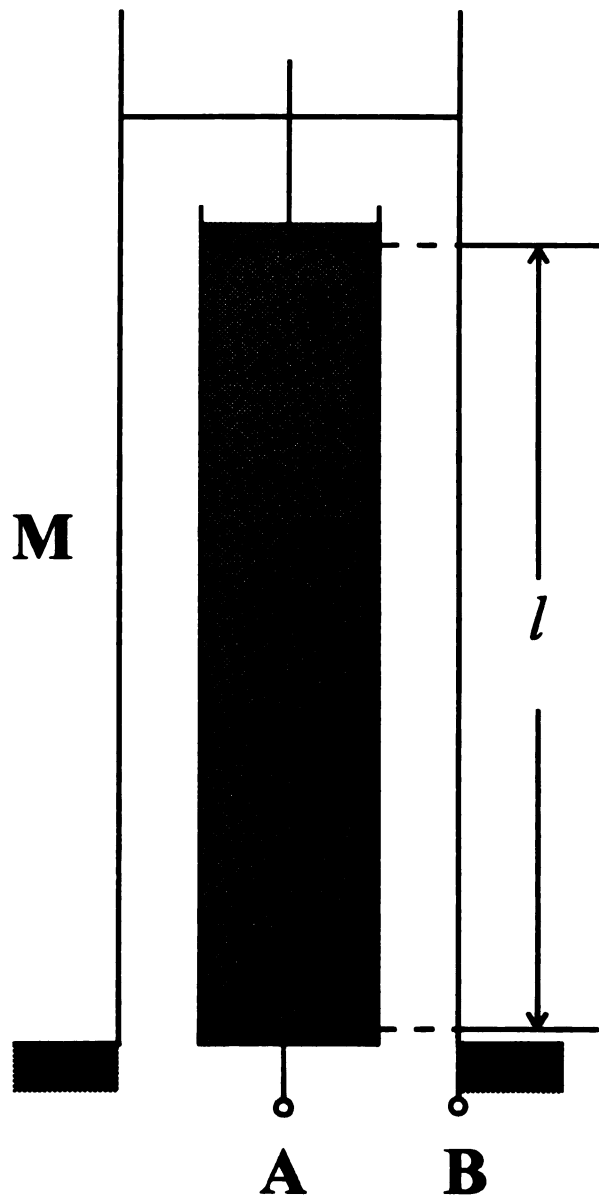


Fig.5.4: Cylindrical teflon sample cell S with metallic coaxial shield M .

$$Y_0 = \left(\frac{j\omega C}{R} \right)^{1/2} \frac{1 + \exp \left[-2l(j\omega CR)^{1/2} \right]}{1 - \exp \left[-2l(j\omega CR)^{1/2} \right]}. \quad (5.3.6)$$

Since $Y_0 = G_0 + j\omega C_0$,

$$G_0 = G \left(\frac{R\omega C}{2} \right)^{1/2} \frac{e^a - e^{-a} + 2 \sin a}{e^a + e^{-a} - 2 \cos a} \quad (5.3.7a)$$

and

$$C_0 = \frac{C}{(2R\omega C)^{1/2}} \frac{e^a - e^{-a} - 2 \sin a}{e^a + e^{-a} - 2 \cos a}. \quad (5.3.7b)$$

Here $G = 1/R$ and $a = l(2R\omega C)^{1/2}$. If the sample is highly conducting and the low frequency range is considered, then a is much smaller than 1. Hence the conductance G_0 and the capacitance C_0 can be expressed by

$$G_0 = \frac{G}{2l} \frac{1 + \frac{a^4}{5!} + \frac{a^8}{9!} + \dots}{\frac{1}{2!} + \frac{a^4}{6!} + \frac{a^8}{10!} + \dots}, \quad (5.3.8a)$$

$$C_0 = Cl \frac{\frac{1}{3!} + \frac{a^4}{7!} + \frac{a^8}{11!} + \dots}{\frac{1}{2!} + \frac{a^4}{6!} + \frac{a^8}{10!} + \dots}. \quad (5.3.8b)$$

In the limit $a \ll 1$ Eqs.(5.3.8) become

$$G_0 = G/l \text{ and } C_0 = \frac{1}{3} Cl. \quad (5.3.9)$$

These are the conductance and the capacitance contributions due to the stray field between sample and shield. Therefore the total capacitance is obtained from Eqs.(5.3.3) and (5.3.9), i.e.,

$$C_T = \epsilon\epsilon_0 \frac{A}{l} + \frac{Cl}{3} + \frac{1}{\omega^2 R^2 C_p}. \quad (5.3.10)$$

The apparent dielectric constant is

$$\epsilon_s = \epsilon + \frac{C}{3\epsilon_0 A} l^2 + \frac{\kappa^2 A}{\omega^2 C_p \epsilon_0} \frac{1}{l}. \quad (5.3.11)$$

We have used $R = \frac{1}{\kappa} \frac{l}{A}$, where κ is the conductivity of the sample. The three components of ϵ_a plotted in a logarithmic scale are shown in Fig.5.5. From this analysis there are two ways to proceed.

- (1) Use this technique to separate ϵ from ϵ_a . The real dielectric constant of the sample can be obtained by subtracting the contribution of the stray and the electrode polarization terms which are extrapolated from measurements at very high and low l -values respectively.
- (2) From measurements on H_2O , put $\epsilon = 78$ and use large l measurements to calculate C which is assumed to be independent of sample.

The details of the method used by Schwan and his coworkers are vague but apparently they used a method like (1) above. A typical result of their work is shown in Fig.4.1 and it is this behaviour we have tried to emulate. The graphs are similar to what would be obtained from the alignment of permanent dipoles but current interpretations are different.

Some of the results Schwan and his co-workers found are

- i) the dielectric constant is proportional to the particle size,
- ii) the characteristic time(i.e., the period corresponding to the maximum in ϵ'' in Fig.4.1) is proportional to the square of the particle radius,
- iii) both the dielectric constant and the characteristic time are independent of salinity at high salinity.

We note that Schwan et al. used concentrations as high as 30 volume % of microspheres. Present day manufacturers rate 4% to 10 % as maximum values for stability against coagulation.

5.3a Review of other experiments

Springer and Lyklema[2]

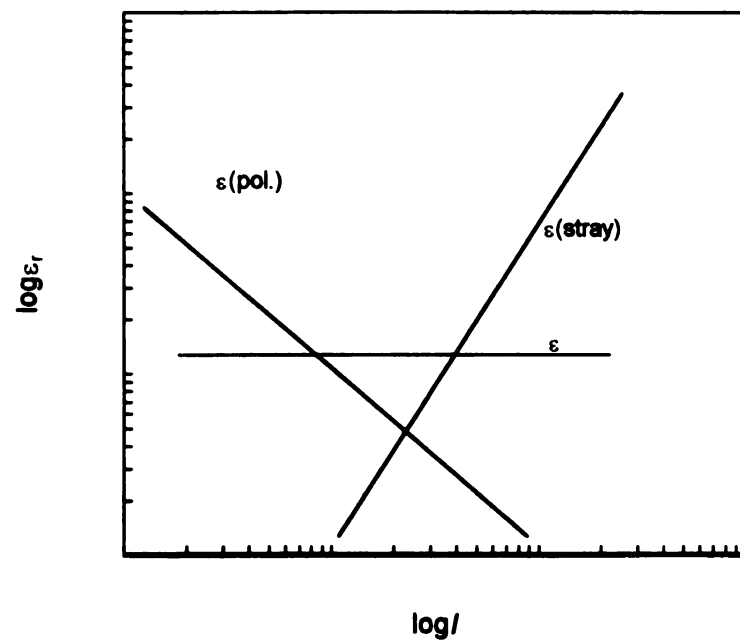


Fig.5.5: Components of the apparent dielectric constant as function of electrode distance.

They used a small cell with variable electrode spacing. Their cell had a guard electrode which was used to control stray electric fields. The electrodes were sandblasted platinum, a "well known" method of reducing the electrode effects. In their results a dielectric loss peak appears. The experimental results shown in Fig.5.6(a) are measurements of the sample of 222nm latex(2.2% solids) in 0.878mM KCl solutions.

Lim and Franses[3]

They employed a cell with variable electrode spacing which is similar to Springer's but they used a platinum black electrode instead of a sandblasted one. They also used a microprocessor controlled bridge circuit which controlled the experiment and records data so that the speed of measurements was increased significantly. They only give the real part of the dielectric constant and don't mention the imaginary part. In Fig.5.6(b) the data are for 450nm polystyrene latex(4.4% solids) in aqueous NaCl.

Myers and Saville[4]

A four electrodes method was used in these experiments and all electrodes were platinum blacked. They assume that separating the current source and sink electrodes and voltage measuring electrodes eliminates the electrode effects. The voltage drops at the source and sink electrodes don't affect the current across the entire cell. Even though the voltage drop at the voltage measuring electrodes is large using a high input impedance measuring device minimizes current flow through the electrodes. Therefore the voltage drop at the electrodes is negligible compared to the voltage drop between the electrodes. They also used a computerized measurement system to reduce the measurement time. Their results show a dielectric behavior similar to Schwan's. In Fig.5.6(c) the sample is 191nm latex in 0.1mM HCl solutions. The volume fraction of polystyrene balls is 4.1%.

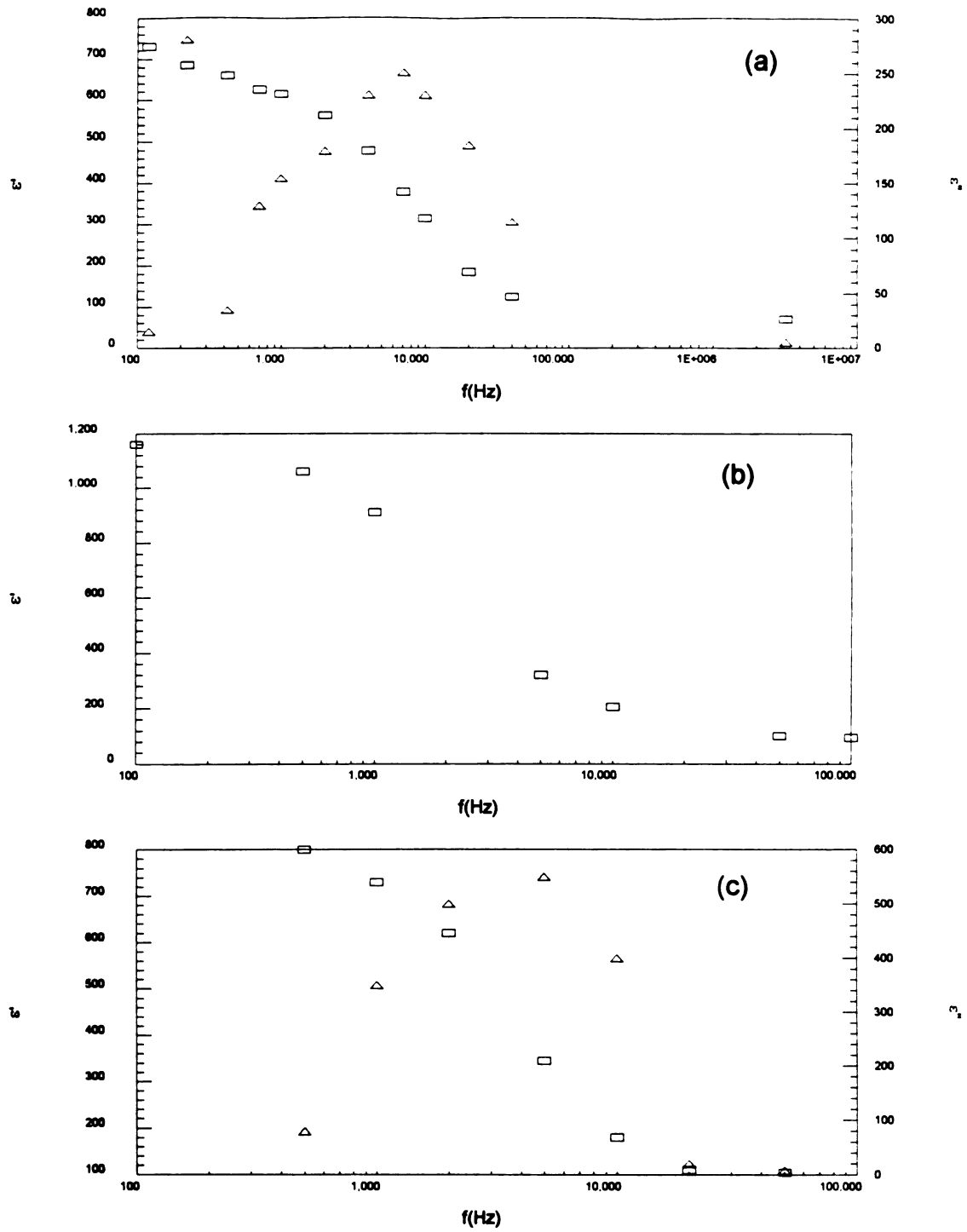


Fig. 5.6: Dielectric properties(real part(\square) and imaginary part(Δ)) from (a) Springer and Lyklema and (b) Lim and Franses (c) Myers and Saville.

In table 5.1 we compare all the measurements that we are aware of at this time. It is clear that there are wide divergences and there are many variables whose effects have not been studied in detail. The experimental state cannot be described as satisfactory.

Table 5.1 Comparison of the previous experimental results.

	diameter(nm)	f_o (KHz)	ϵ_o	solid %	solution
Schwan	88	80	540	<30	1mM KCl
	188	15	2450		
	566	1.8	3000		
	1170	0.6	10,000		
Lim	450		1160	4.4	NaCl
Springer	222	43.5	750	2	0.878mM KCl
Myers	191	3	800	4.1	1mM HCl

5.4 Experimental setup

5.4.1 Capacitance cell

The experimental determination of dielectric properties is usually accomplished by measuring the capacitance of a material using a plain parallel capacitor. If the capacitor is ideal the capacitance is given by

$$C = \epsilon_r \epsilon_o \frac{A}{d}. \quad (5.4.1)$$

But the electric field between the plates of an ordinary plain parallel capacitor is not uniform due to edge effects. These can be reduced by using the guard ring arrangement discussed in section 1.3. If the material is a highly conducting liquid, such as an aqueous

electrolyte solution, the electrode polarization effect due to the impedance of the diffuse double layer at the electrodes makes the determination of the sample capacitance difficult. According to the literature this effect can be reduced by using bare platinum or platinum black electrodes[10,11].

From the second part of Eq.(5.3.3) we deduce that increasing the resistance of the sample reduces the electrode polarization effect. This implies that the electrode effect is very small for a nonconducting sample so that it may be neglected. But if the conductivity of a sample is high enough then it makes a considerable contribution to the total capacitance. One way to increase the total resistance of the sample is to make a longer sample. To do so a large, especially long, cell is needed. Fig.5.7 shows the schematic diagram of the long cylindrical capacitance cell we used. The capacitance cell consists of two parts. The lower cylinder contains the liquid sample and holds the lower electrode E_L . The upper part supports the micrometer M and the upper electrode E_U . The upper electrode can be moved by hand in the vertical direction through the tubes containing two guiding O-rings. It is fixed coaxially to a glass tube so that it is electrically isolated from the outer cylinder. The lower electrode is separated by epoxy from the shield. In this arrangement we anticipated using Schwan's analysis method to compensate the stray capacitance. The long cylindrical arrangement can reduce the electrode polarization effect but cannot avoid the stray field effect. However in a high ϵ_r sample the field lines will tend to concentrate in the sample.

5.4.2 Electrodes

Earlier measurements were made with brass electrodes. Difficulties with these experiments led us to use platinum and platinum black electrodes. The face of each electrode was covered with platinum sheet using conducting silver epoxy. Both platinum electrodes were electroplated with platinum black to reduce the electrode polarization effect[12]. The plating apparatus consisted of a 50mL beaker, the platinum electrode to

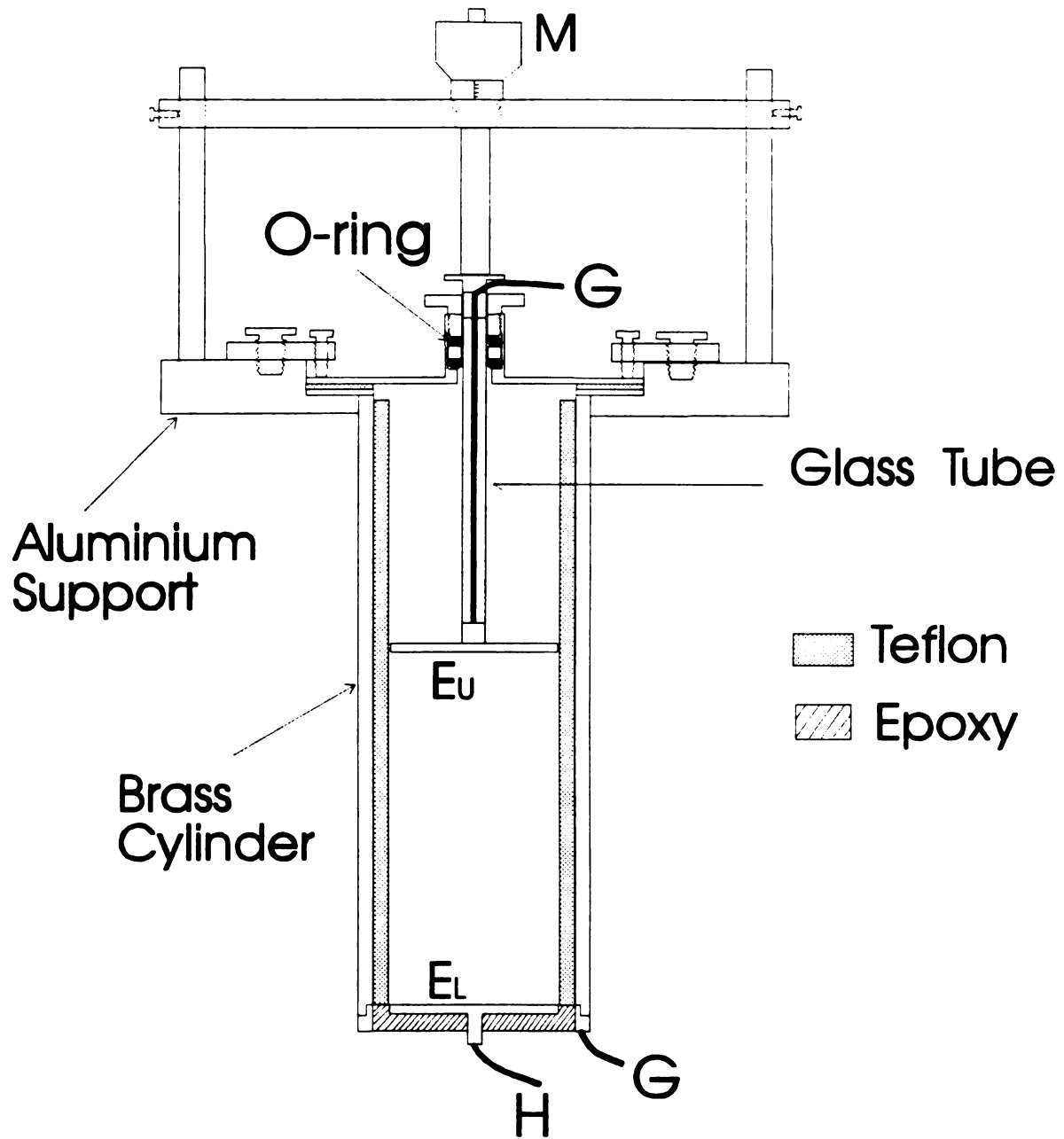


Fig.5.7: Long cylindrical dielectric cell. H and L are the high and low terminal. G is ground. E_U and E_L are the upper and low electrodes. M is the micrometer.

be plated, a counter electrode and a DC power supply. The platinic acid solution (1.4% PtCl_6^{2-} and 0.02% Pb^{2+} in dilute aqua regia) was prepared from 1.58g of the hydrogen hexachloroplatinate hydrate (from Aldrich Chem. Co.) in 10 mL of aqua regia (one part HNO_3 , three part HCl). It was diluted to 50g of solution with deionized water. Finally 0.01g $\text{Pb}(\text{NO}_3)_2$ was added. The lead nitrate is a powerful oxidizing agent essential to the production of the platinum black matrix. The counter electrode used was a braided platinum wire connected to the positive pole of a DC power supply. The electrode to be plated was immersed in the platinic acid solution and connected to the negative pole. The electroplating was achieved in 5 minutes with the power supply adjusted to 2V. After that both electrodes were rinsed several times with deionized water.

Springer and Lyklema have recommended sandblasted Pt electrodes for diminishing the effect of electrode polarization. We have also performed measurements with these electrodes (See section 5.5.2).

5.4.3 Microsphere samples

Initially samples were bought from Interfacial Dynamics Corporation and Duke Scientific. The data in this thesis are for samples made by Mr. Grant Shouldice a graduate student in the Department of Chemistry at the University of Waterloo, London Ontario. They are generated via emulsifier-free emulsion polymerization of styrene[13].

Microspheres are stabilized against coagulation though the electrostatic charge on the particles. In the past the polymerization took place in the presence of a surfactant usually alkyl sulfonates or alkyl carbonates. These materials adsorb at the particle surface, enhancing the negative charge on the microspheres and thereby increasing colloidal stability and resistance to coagulation by electrolyte ions. The use of surfactants, however leads to a product with ill defined surface properties, unless they pass through complex processes to remove the surfactant.

Now the microspheres are prepared without the use of surfactants. Instead in a surfactant free process high concentrations of an "initiator" are used. Charge previously supplied by the surfactant is produced from the generation of intrinsic charges at the particle surface, thereby negating the necessity of having charge from adsorbed surfactant molecules.

Polymer microspheres made of polystyrene comprise chains of polystyrene held together by van der Waals forces to form non porous hydrophobic particles. The hydrophobic nature of these particles would encourage aggregation. Surfactant free microspheres are stabilized against aggregation by surface charges introduced at the particle surface by various polymer chain terminators introduced in the polymerization process, rather than by the introduction of ionic surfactants or detergents.

Hydrophobic polymers always tend to aggregate. This tendency is prevented by electrostatic repulsion from the presence of surface charge groups on the particle. Aggregation can be avoided by keeping the suspensions dilute. Typically sulfate or carboxylate lattices are sold at < 10 vol% solid. Depending on the particles' surface group and concentration, the recommended maximum vol% solid can be considerably smaller than that. The samples we receive from University of Waterloo have 4 vol% solid.

The latex microspheres have a pK associated with the surface group which is analogous to the pH for hydrogen ion concentration. For stability the pH of the suspension should be selected so that the surface charge groups on the microspheres remain fully ionized, i.e., $pH > pK+1$. For sulfate latexes $pK < 2$ and consequently the particles are stable in acid media. For the carboxyl group pK is ~ 5 and consequently these particles are not suitable for work in acidic media.

The samples have all the same vol% but different surface charge densities. Determining the charge density is done by the conductometric titrations using 1mM NaOH solutions. Fig.5.8 are the titration data for all solutions. In each graph the minimum is the equivalent point which implies that the moles of base added is equal to the moles of acid

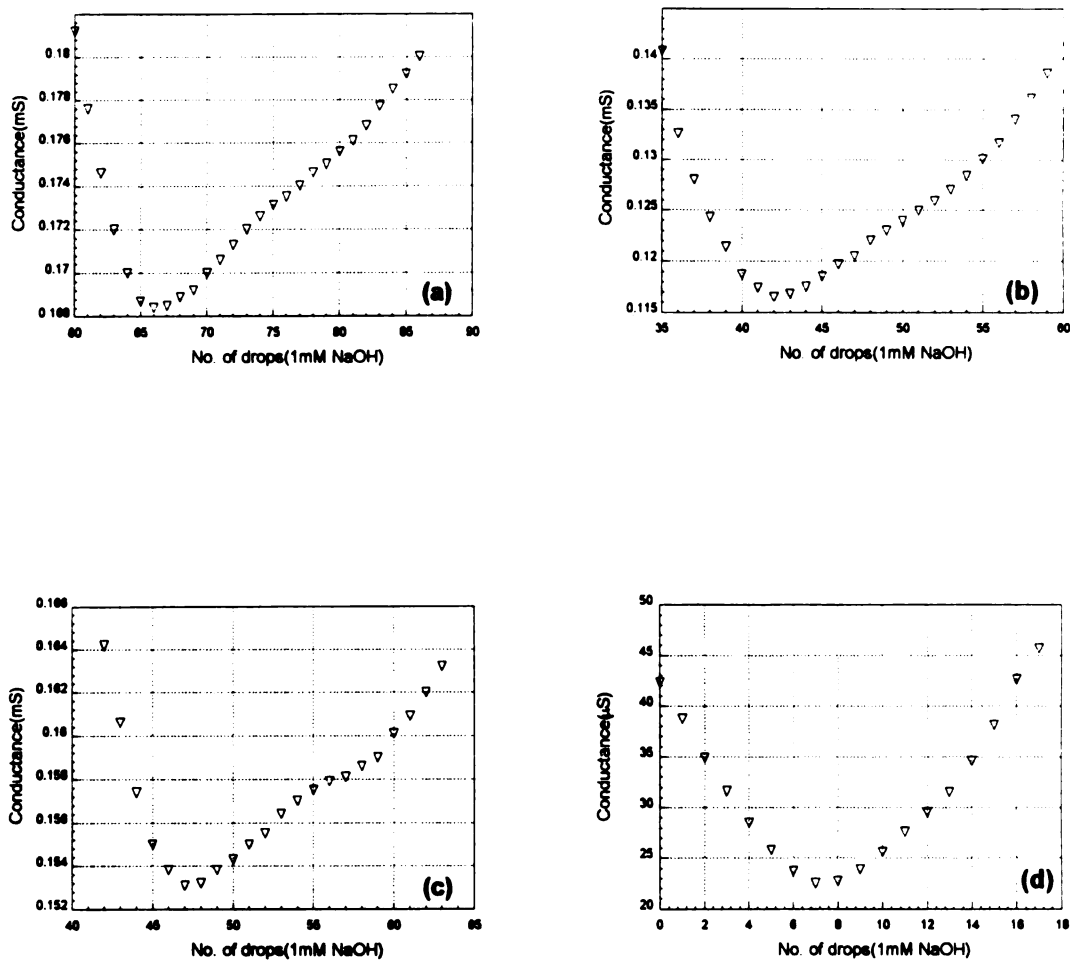


Fig.5.8: Titration data of (a) 213.8nm (b) 364.1nm (c) 367.7nm (d) 624.3nm suspensions.

groups. Assuming a point charge for each acid group we may obtain the surface charge density by dividing the number of charges by total surface area. The surface charge densities of 213.8nm, 364.1nm, 367.7nm and 624.3nm balls are 3.34, 3.61, 4.01, and 1.03 in $\mu\text{C}/\text{cm}^2$, respectively. The combination of low charge density and large mass, resulted in visible sedimentation of the 624.3nm balls in the course of several days.

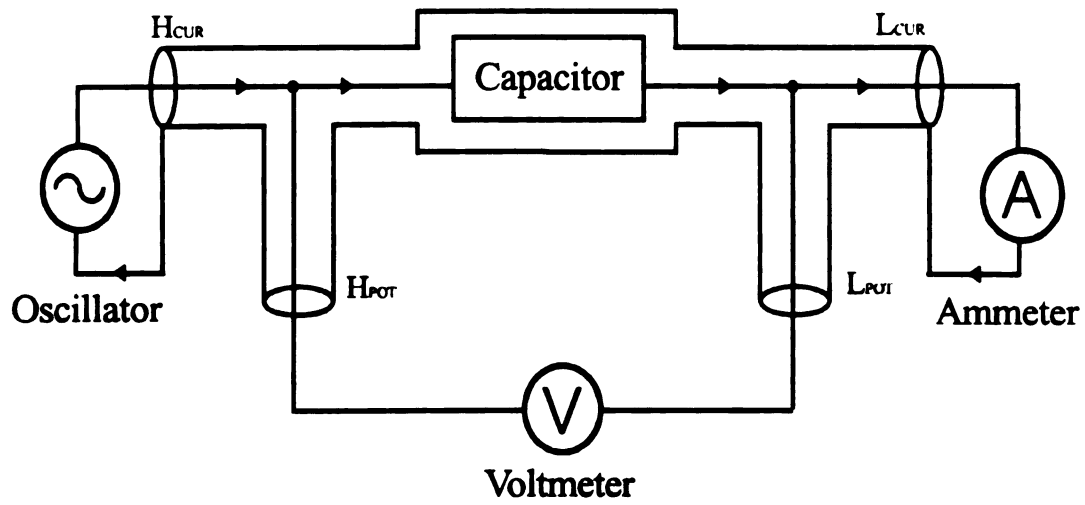
5.4.4 Measurement setup

The HP 4192A impedance analyzer was used to measure the admittance at each frequency. The 4192A employs the four terminal configuration measurement illustrated in Fig.5.9[14]. To compose a measurement circuit loop in a four terminal pair configuration, the H_{CUR} and H_{POT} , L_{POT} and L_{CUR} terminals must be respectively connected together and, in addition, the shields of all conductors must be connected together. The distinctive feature of the four terminal pair configuration is that the outer shield conductor works as the return path for the measurement signal current. The same current flows through both the center conductors and the outer shield conductors in opposite directions. Thus no external magnetic fields are generated around the conductors, i.e., the magnetic fields produced by the inner and outer currents completely cancel each other. Because the measurement signal current does not develop an external inductive magnetic field, the test leads do not contribute additional measurement errors due to mutual-inductance between the individual leads.

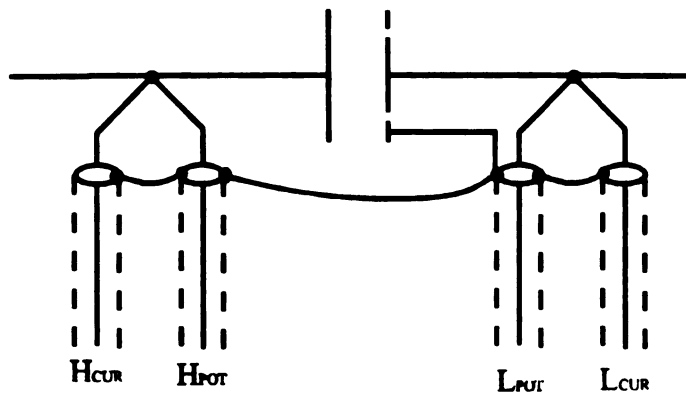
5.5 Experiments and discussion

5.5.1 Long cell

In this section we give experimental data obtained using the long cylindrical cell with three different electrodes, brass, platinum and platinum with platinum black.



(a)



(b)

Fig.5.9: (a) Four terminal pair measurement principle. (b) Actual four terminal pair connections.

Fig.5.10(a) shows the apparent dielectric constants of distilled water. The data set at 100KHz does not include polarization effects because of the high frequency. But the data at the low frequency(1KHz) indicate that the electrode effect is getting bigger. On the other hand capacitance data for a 1mM KCl solution (Fig.5.10(b)) show the electrode effect occurring at a much higher frequency. For example the apparent dielectric constant of a 1mM KCl solution at 1 KHz gives a strong electrode polarization effect throughout the range of electrode separations (see Fig.5.10(b)). This is very crucial because the system of polystyrene balls suspended in water generally has a high conductivity. Furthermore we add some electrolyte to make the double layer effect at the balls larger. The contribution of electrode polarization in the case of distilled water is comparatively small due to its high resistance.

The high frequency data for water in Fig.5.11(a) show negligible polarization effects. However after the subtraction of the stray capacitance obtained by extrapolation from large l the corrected dielectric constant is not constant. The capacitance due to stray fields is not expected to be a function of frequency but we see differences in stray contributions at high- l values for the three frequencies in Fig.5.10(a). There are also serious problems with the subtraction of electrode polarization effects. Fig.5.11(b) illustrates the imprecision of subtracting the electrode polarization part from the data for 1mM KCl at 1KHz. Fig.5.11(c) shows the data of 1mM KCl at 10 KHz with subtraction of stray capacitance but there is no way to subtract the electrode polarization effect because there are insufficient data for good extrapolation. We conclude that it is impossible to get correct sample data from the capacitance measured this way. The one hope is to further reduce the electrode polarization effect.

5.5.1a Effect of electrode material

It is customary to use platinum, platinum black, and sandblasted Pt electrodes in order to make the electrode effects smaller. From Fig.5.12 we see that use of a platinum

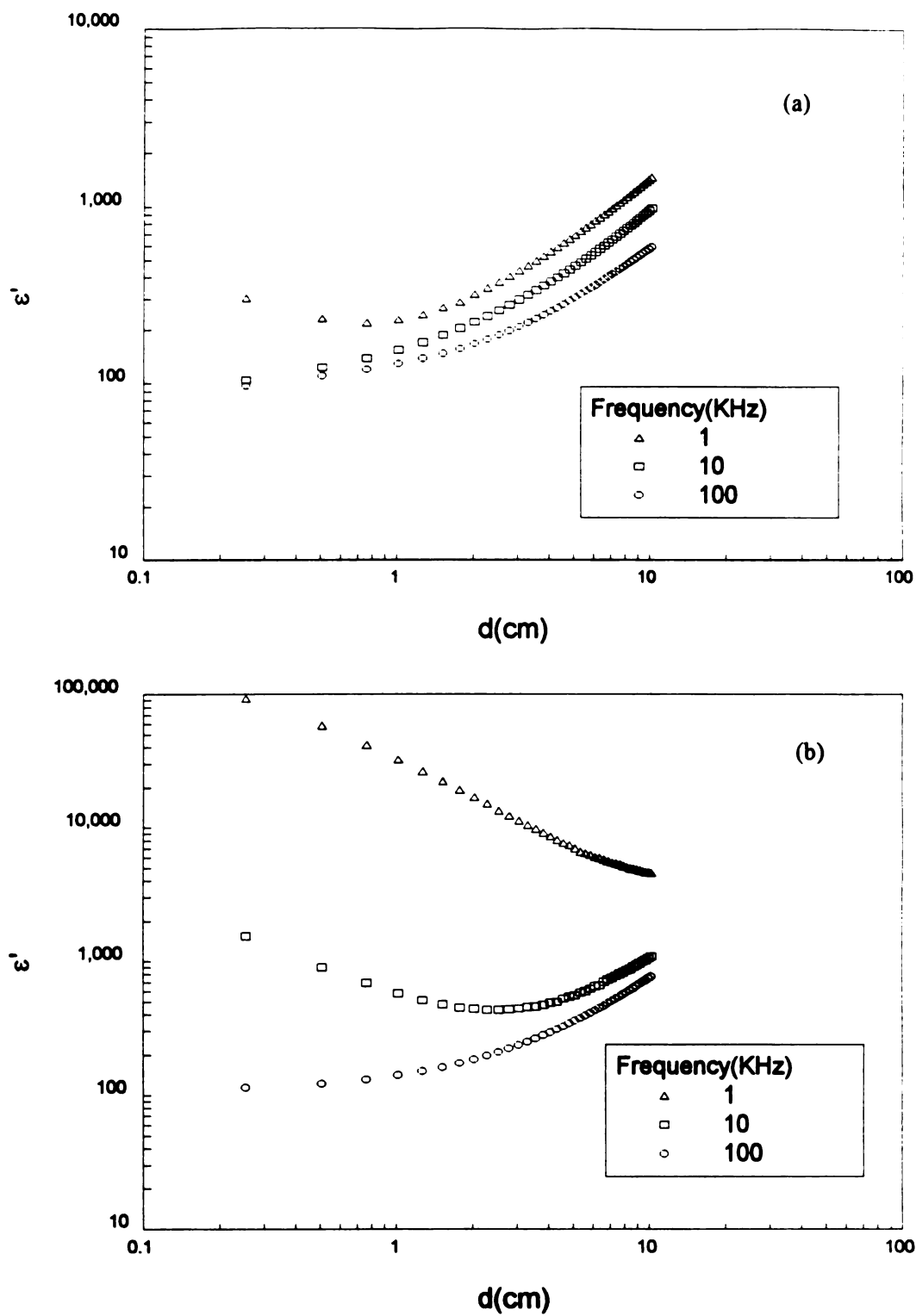


Fig.5.10: Apparent dielectric constants of (a) distilled water and (b) 1mM KCl solution using brass electrode.

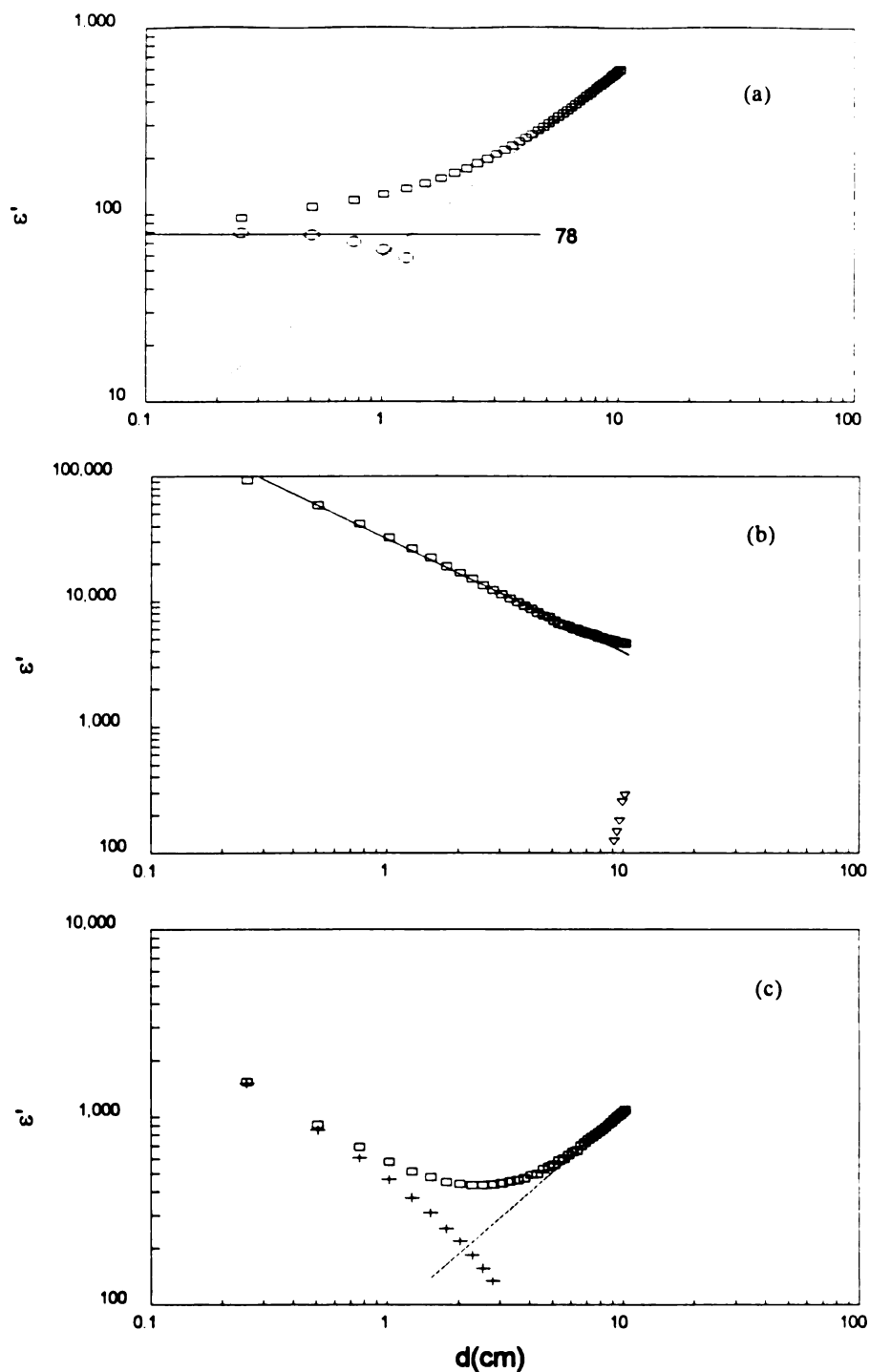


Fig.5.11: Apparent dielectric constants(\square). (a) Real dielectric constant(\circ) after subtraction of stray effects of distilled water at 100KHz. (b) Real dielectric constant(∇) after subtraction of electrode effects of 1mM KCl at 1KHz. (c) Real dielectric constant($+$) after subtraction of stray effects of 1mM KCl at 10KHz.

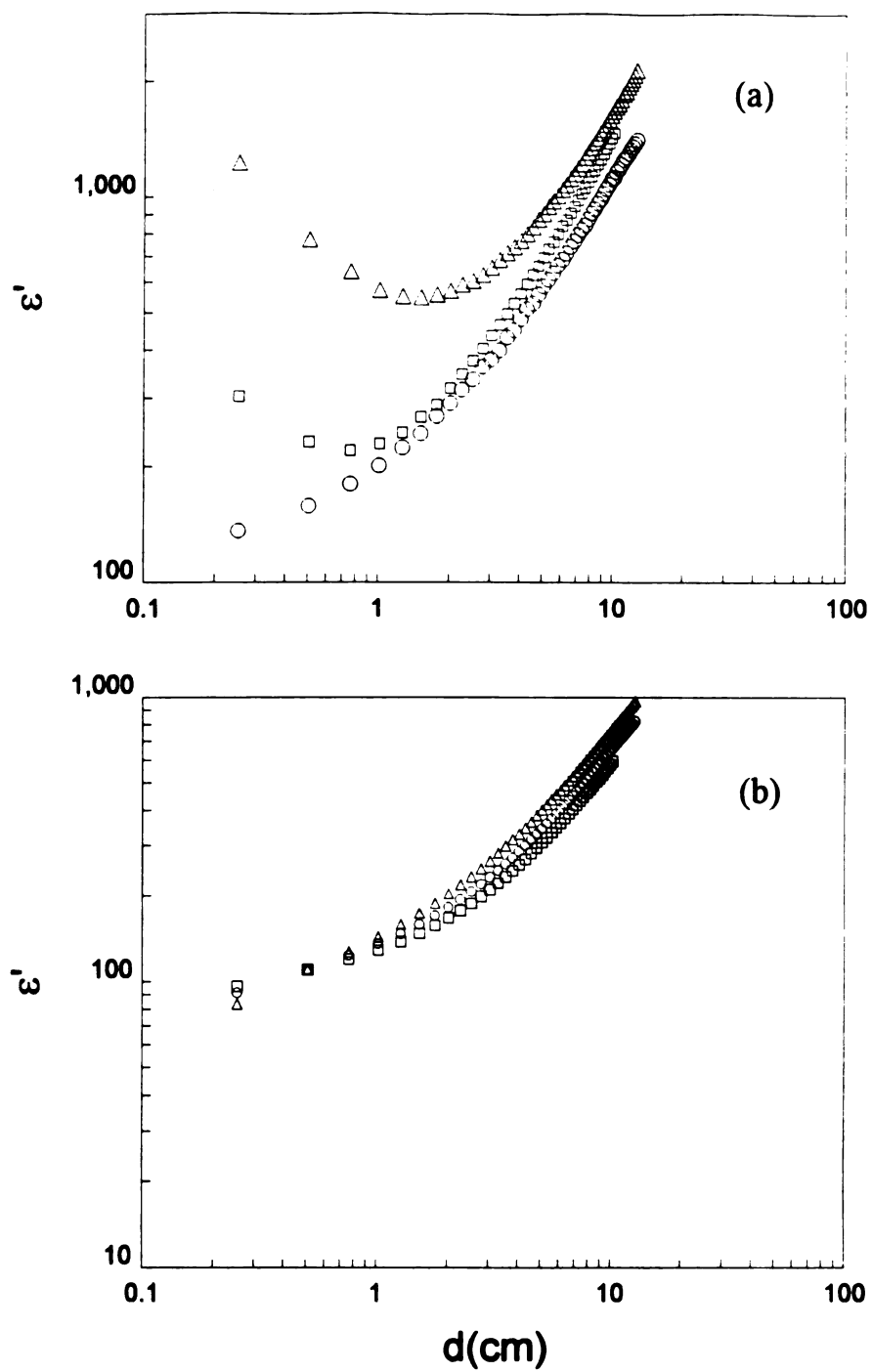


Fig. 5.12: Apparent dielectric constants of distilled water at (a) 1KHz and (b) 100KHz using brass(\square), platinum(\circ), and platinum black(Δ) electrodes, respectively.

electrode reduced the electrode effects. But it seems that the platinum black electrode made the electrode effects worse. Experiments on sandblasted Pt electrodes were performed in a different cell and will be described later.

At this point we examine the role of platinum black which is frequently quoted as reducing the electrode effect. According to Eq.(5.3.10) the electrode effect can be reduced by making the sample resistance (R) large. If the platinum black electrode by increasing R makes the electrode effect smaller, without any additional effect, the dielectric constant of distilled water with platinum black electrodes at small separations should be smaller than the others. But in Fig.5.12 the data at low separations are not consistent with this prediction. We argue that the introduction of a high resistance platinum black layer confuses the issue further by introducing a Maxwell-Wagner effect. We refer to the Figs. 5.12 and 4.3. At a low frequency like 1KHz, apparent dielectric constants using a platinum electrode are much smaller than dielectric constants using a platinum black electrode while the reverse is true at high frequency over 100KHz and small electrode separation. This is consistent with the form of the Maxwell-Wagner effect shown in Fig.4.3. The Maxwell-Wagner contribution is very large at low frequency but it is much smaller at high frequency. Even at high frequency the dielectric constants are smaller than the dielectric constant of the conducting medium by itself. Data using the Pt electrode was better but we still had difficulty in making the necessary subtraction.

In addition to the above difficulties in obtaining the accurate capacitance from the Schwan analysis there are problems associated with the analysis of R_m . Eq.(5.3.2) can be written as

$$R_m = R_s \left(1 + (\omega C_m R_m)^2 \right) + R_p. \quad (5.5.1)$$

The second term in the parenthesis is the square of the quality factor of the whole system which is much less than 1 (See table 5.2). It can further be taken that R_p is small compared with R_s if the size of the electrode is not too small. Thus we can approximate $R_m \approx R_s = 1/G_s$ so that the total conductance should be

Table 5.2 The quality factor of 1mM KCl.

f(KHz)	Cm	Gm	Qm	Qm^2	f(KHz)	Cm	Gm	Qm	Qm^2
0.005	5.79E-06	1.02E-04	2.83E-01	8.01E-02	10	2.30E-10	1.31E-03	1.76E-03	3.09E-06
0.01	4.62E-06	1.82E-04	2.54E-01	6.43E-02	20	1.50E-10	1.31E-03	2.29E-03	5.25E-06
0.02	3.38E-06	3.42E-04	1.98E-01	3.90E-02	30	1.30E-10	1.31E-03	2.98E-03	8.88E-06
0.03	2.61E-06	4.86E-04	1.61E-01	2.59E-02	40	1.30E-10	1.31E-03	3.97E-03	1.58E-05
0.04	2.07E-06	6.09E-04	1.36E-01	1.85E-02	50	1.20E-10	1.31E-03	4.58E-03	2.10E-05
0.05	1.68E-06	7.11E-04	1.18E-01	1.39E-02	60	1.20E-10	1.31E-03	5.50E-03	3.03E-05
0.06	1.38E-06	7.94E-04	1.04E-01	1.09E-02	70	1.21E-10	1.31E-03	6.47E-03	4.19E-05
0.07	1.15E-06	8.63E-04	9.36E-02	8.75E-03	80	1.20E-10	1.31E-03	7.33E-03	5.38E-05
0.08	9.75E-07	9.20E-04	8.48E-02	7.19E-03	90	1.20E-10	1.31E-03	8.25E-03	6.81E-05
0.09	8.35E-07	9.68E-04	7.76E-02	6.02E-03	100	1.20E-10	1.31E-03	9.17E-03	8.40E-05
0.1	7.21E-07	1.01E-03	7.16E-02	5.12E-03	200	1.19E-10	1.31E-03	1.82E-02	3.31E-04
0.2	2.40E-07	1.19E-03	4.02E-02	1.62E-03	300	1.19E-10	1.31E-03	2.73E-02	7.44E-04
0.3	1.16E-07	1.25E-03	2.79E-02	7.80E-04	400	1.18E-10	1.31E-03	3.60E-02	1.30E-03
0.4	6.81E-08	1.27E-03	2.14E-02	4.58E-04	500	1.18E-10	1.31E-03	4.50E-02	2.03E-03
0.5	4.43E-08	1.28E-03	1.72E-02	2.97E-04	600	1.18E-10	1.31E-03	5.40E-02	2.92E-03
0.6	3.13E-08	1.29E-03	1.45E-02	2.12E-04	700	1.18E-10	1.31E-03	6.32E-02	3.99E-03
0.7	2.32E-08	1.30E-03	1.26E-02	1.58E-04	800	1.18E-10	1.31E-03	7.21E-02	5.20E-03
0.8	1.79E-08	1.30E-03	1.10E-02	1.22E-04	900	1.18E-10	1.31E-03	8.11E-02	6.58E-03
0.9	1.42E-08	1.30E-03	9.82E-03	9.65E-05	1000	1.19E-10	1.32E-03	9.01E-02	8.12E-03
1	1.16E-08	1.30E-03	8.92E-03	7.95E-05	2000	1.19E-10	1.33E-03	1.79E-01	3.19E-02
2	3.10E-09	1.31E-03	4.74E-03	2.25E-05	3000	1.20E-10	1.37E-03	2.64E-01	6.99E-02
3	1.40E-09	1.31E-03	3.21E-03	1.03E-05	4000	1.22E-10	1.41E-03	3.46E-01	1.20E-01
4	8.00E-10	1.31E-03	2.44E-03	5.98E-06	5000	1.24E-10	1.47E-03	4.22E-01	1.78E-01
5	6.00E-10	1.31E-03	2.29E-03	5.25E-06	6000	1.27E-10	1.56E-03	4.91E-01	2.41E-01
6	4.00E-10	1.31E-03	1.83E-03	3.36E-06	7000	1.31E-10	1.66E-03	5.53E-01	3.05E-01
7	3.50E-10	1.31E-03	1.87E-03	3.50E-06	8000	1.36E-10	1.79E-03	6.05E-01	3.66E-01
8	3.00E-10	1.31E-03	1.83E-03	3.36E-06	9000	1.41E-10	1.96E-03	6.48E-01	4.19E-01
9	2.50E-10	1.31E-03	1.72E-03	2.95E-06	10000	1.47E-10	2.17E-03	6.79E-01	4.61E-01

$$G_t = G_s + G_0, \quad (5.5.2)$$

where the second term is the stray conductance which is represented by Eq.(5.3.9). Both terms in the right hand side of the above equation vary linearly with $1/l$ which makes separation of the two components difficult. In Fig.5.13 we show that the conductance vs. $1/l$ graph is close to linear for Pt electrodes. For the platinum black electrode there are wide divergence from linearity. For the platinum black electrode the additional term which is associated with Maxwell-Wagner effect should be added in Eq.(5.5.2). Then the total resistance becomes a very complicated function of l which is almost impossible to separate. Because of these difficulties we proceeded to use a different method using a smaller cell.

5.5.2 Small cell

Since, despite our efforts, the above configuration still has reduced but serious electrode and stray field effects, the small cell with guard ring arrangement[15] (See Fig.5.14) might have a merit if the electrode polarization can be removed appropriately. The cell has two parts which are separated by epoxy to maintain electrical isolation between them. The top part supports a precision micrometer and the bottom part contains the fluid. The lower electrode was machined separately, then held in the correct position relative to the guard ring and fixed there by pouring epoxy. The upper electrode was fixed to the spindle of the micrometer.

Fig.5.15 shows the equivalent circuit suggested by Touw, Mandel, Honijk and Verhoog[16, 17]. For the long cylindrical cell we tried to apply Schwan's method to eliminate stray field effects. When we are using a small separation between electrodes the stray field effect (C_s and G_s in Fig.5.15(a)) can be reduced by the guard ring arrangement. In the following analysis we neglect them. The resistance(R_l) and inductance(L) of the lead wires are also negligible. Hence G_m and C_m of the equivalent circuit in Fig.5.15(b)

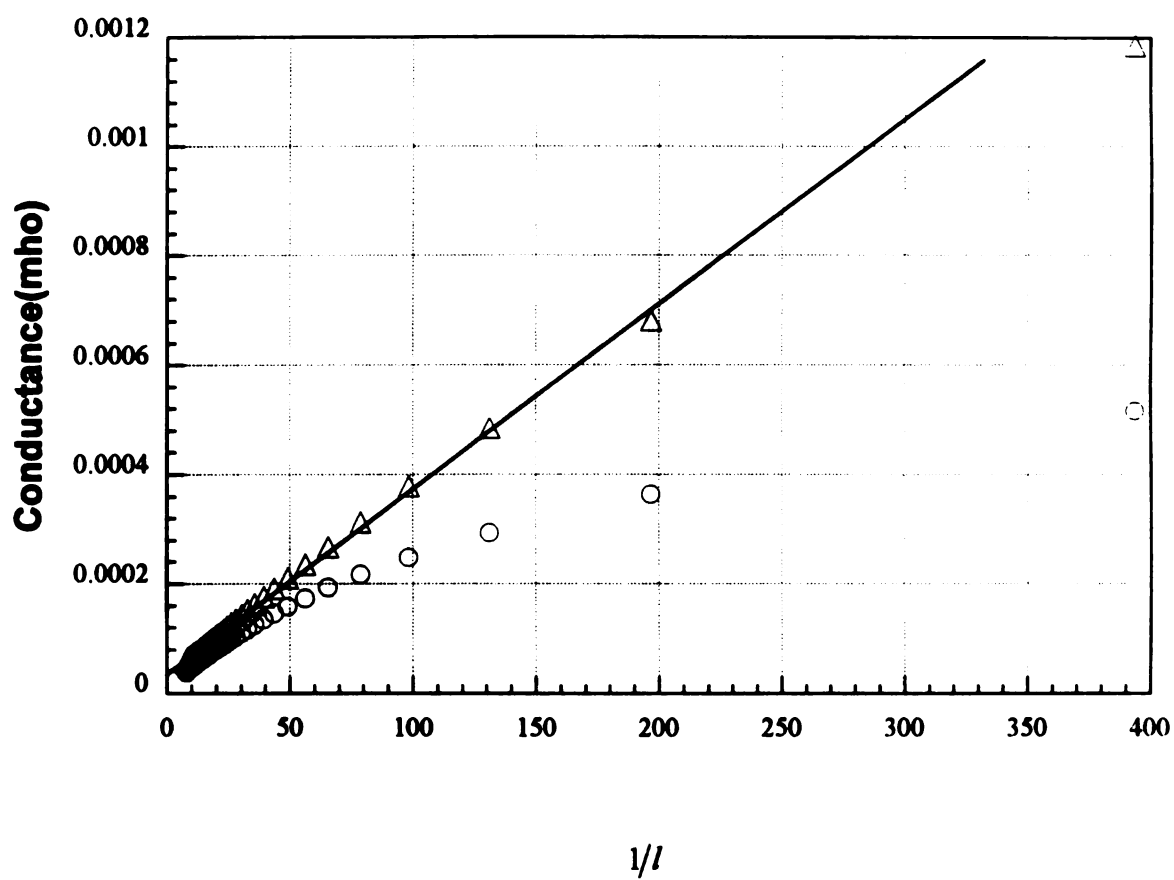


Fig.5.13: Conductance vs. $1/l$ of 1mM KCl solution using Pt(Δ) and Pt black(O) electrodes at 100KHz. The solid line is a guide to the eye.

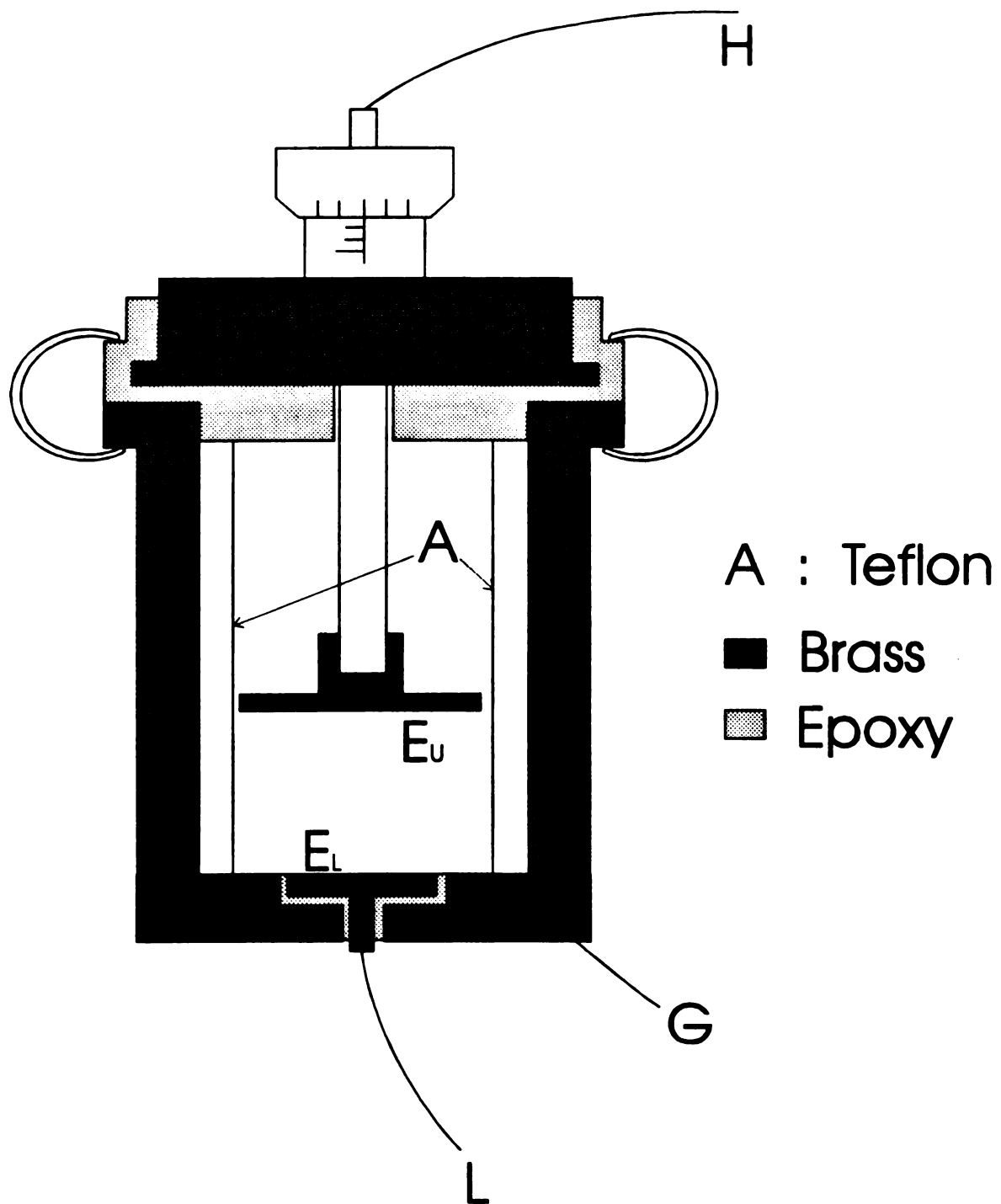


Fig.5.14: Dielectric cell with guard ring arrangement. H and L are the high and low terminals respectively. G is ground, and E_u and E_l are the upper and lower electrodes.

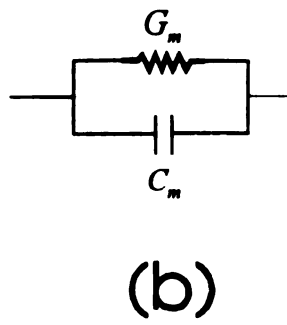
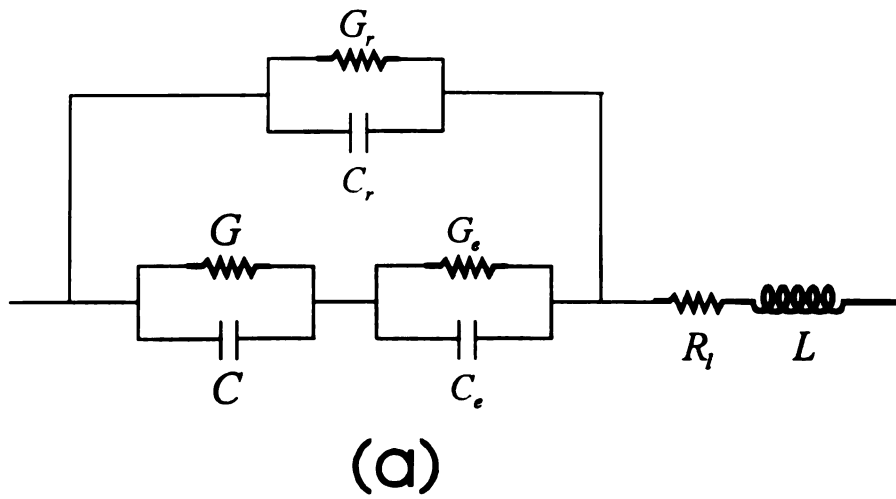


Fig.5.15: (a) A detailed electric circuit of the cell. (b) A measured equivalent circuit. The subscripts r, e, m stand for residual, electrode and measure, respectively. R_l is lead wire resistance.

can be related to impedances by

$$\frac{1}{G_m + j\omega C_m} = \frac{1}{G + j\omega C} + \frac{1}{G_e + j\omega C_e}, \quad (5.5.3)$$

where G_m and C_m are measured conductance and capacitance, and G and C are those of the sample, and G_e and C_e are those of the electrode effect respectively. From this equation we can deduce that

$$G_m [G_m^2 + \omega^2 C_m^2]^{-1} = [G(1 + Q^2)]^{-1} + [G_e(1 + Q_e^2)]^{-1}, \quad (5.5.4a)$$

$$C_m [G_m^2 + \omega^2 C_m^2]^{-1} = C[G^2(1 + Q^2)]^{-1} + C_e[G_e^2(1 + Q_e^2)]^{-1}, \quad (5.5.4b)$$

where $Q = \omega CG^{-1}$ and $Q_e = \omega C_e G_e^{-1}$ are the quality factors of the solution and the double layer on the electrode respectively. Eqs.(5.5.4) can be rewritten by

$$G_m^{-1} = G^{-1}(1 + Q_m^2)(1 + Q^2)^{-1} + G_e^{-1}(1 + Q_m^2)(1 + Q_e^2)^{-1}, \quad (5.5.5a)$$

$$C_m = CG_m G^{-2}(1 + Q_m^2)(1 + Q^2)^{-1} + C_e G_m^2 G_e^{-2}(1 + Q_m^2)(1 + Q_e^2)^{-1}, \quad (5.5.5b)$$

where $Q_m = \omega C_m G_m^{-1}$, the quality factor of the whole system. At low frequency Q^2 and Q_m^2 become negligible with respect to unity. Since electrode effects have no influence on G_m and C_m , at high frequency we have $Q_m \approx Q$ so that

$$G_m^{-1} = G^{-1} + G_e^{-1}(1 + Q_e^2)(1 + Q_e^2)^{-1}, \quad (5.5.6a)$$

$$C_m = CG_m^2 G^{-2} + C_e G_m^2 G_e^{-2}(1 + Q_e^2)(1 + Q_e^2)^{-1}. \quad (5.5.6b)$$

From the table 5.2 for $60\text{Hz} < f < 2\text{MHz}$ the squares of the quality factors of the measured quantities are much less than unity so that we can neglect Q_m in the above equations.

Therefore Eqs.(5.5.6) can be written as

$$G_m^{-1} \approx G^{-1} + G_e^{-1}(1 + Q_e^2)^{-1} = G^{-1}(1 + GR_e). \quad (5.5.7)$$

Since the ion concentration near the electrode is greater than that of the bulk solution we may assume that if the electrode resistance $R_e = G_e^{-1}(1 + Q_e^2)^{-1}$ is much smaller than the bulk resistance $R = G^{-1}$, then $G \approx G_m$, and to a good first approximation, Eq.(5.5.6b) yields

$$C_m = C + C_e G^2 G_e^{-2}(1 + Q_e^2)^{-1}. \quad (5.5.8)$$

Using the relations as

$$C_e = \frac{Q_e^2}{1+Q_e^2} C_p \text{ and } R = \frac{1}{G_m} \quad (5.5.9)$$

we can prove Eq.(5.5.8) is identical to Eq.(5.3.3).

Using $G = \sigma A/d$ and $C = \epsilon A/d$, and the fact that the electrode effect is not a function of d Eqs.(5.5.7) and (5.5.8) can be expressed by

$$G_m \approx \sigma A \frac{1}{d} - R_e \sigma^2 A^2 \frac{1}{d^2}, \quad (5.5.10a)$$

$$C_m \approx \epsilon A \frac{1}{d} + \text{const.} \left(\frac{1}{d} \right)^2, \quad (5.5.10b)$$

where d is the separation of electrodes and A is the area of electrode. Using the above analysis the conductivity and dielectric constant can be obtained by fitting the total conductance and the capacitance with a polynomial of $1/d$ up to the second order. Table 5.3 is the results of G_m and G for distilled water and 1mM KCl solution. From this data for distilled water there is about 15% error between G_m and G , and about 4% error for 1mM KCl solutions above 100Hz. The approximation $G \approx G_m$ introduced at Eq.(5.5.8) is good for a highly conducting medium.

5.5.2a Results using Pt black electrode

Fig.5.16 and Fig.5.17 are results using a platinum black electrode. They have loss peaks which should not be seen in the distilled water and KCl solutions. We believe that using a platinum black electrode gives an additional effect so that Eq.(5.5.10b) should be modified to

$$C_m \approx \epsilon A \frac{1}{d} + \text{const.} \left(\frac{1}{d} \right)^2 + MW. \quad (5.5.11)$$

The third term refers to the Maxwell-Wagner polarization term which is also a function of electrode separation. Therefore fitting the measured capacitance to the inverse of the electrode separation gives a wrong result. These results support our contention that the platinum black acts like an insulating layer causing Maxwell-Wagner polarization.

Table 5.3 Comparison of conductivity values obtained from direct measurement(Gm) and from using analysis(G).

f(KHz)	Gm(H2O)	G(H2O)	Gm(KCl)	G(KCl)	f(KHz)	Gm(H2O)	G(H2O)	Gm(KCl)	G(KCl)
0.005	2.42E-04	2.81E-04	5.38E-04	-3.28E-04	10	2.63E-04	3.04E-04	6.89E-03	7.16E-03
0.01	2.53E-04	2.97E-04	9.59E-04	-5.28E-04	20	2.63E-04	3.03E-04	6.89E-03	7.16E-03
0.02	2.59E-04	3.03E-04	1.80E-03	-4.70E-04	30	2.63E-04	3.03E-04	6.89E-03	7.17E-03
0.03	2.61E-04	3.05E-04	2.56E-03	1.14E-04	40	2.63E-04	3.03E-04	6.89E-03	7.16E-03
0.04	2.61E-04	3.04E-04	3.20E-03	9.57E-04	50	2.63E-04	3.03E-04	6.89E-03	7.16E-03
0.05	2.62E-04	3.04E-04	3.74E-03	1.87E-03	60	2.63E-04	3.03E-04	6.89E-03	7.16E-03
0.06	2.62E-04	3.05E-04	4.18E-03	2.73E-03	70	2.63E-04	3.03E-04	6.89E-03	7.16E-03
0.07	2.62E-04	3.04E-04	4.54E-03	3.37E-03	80	2.63E-04	3.02E-04	6.89E-03	7.17E-03
0.08	2.62E-04	3.04E-04	4.84E-03	4.11E-03	90	2.63E-04	3.02E-04	6.89E-03	7.16E-03
0.09	2.62E-04	3.04E-04	5.09E-03	4.67E-03	100	2.63E-04	3.01E-04	6.89E-03	7.17E-03
0.1	2.62E-04	3.04E-04	5.30E-03	5.18E-03	200	2.64E-04	3.03E-04	6.89E-03	7.17E-03
0.2	2.62E-04	3.04E-04	6.28E-03	7.11E-03	300	2.64E-04	3.02E-04	6.89E-03	7.16E-03
0.3	2.63E-04	3.04E-04	6.58E-03	7.39E-03	400	2.65E-04	3.02E-04	6.90E-03	7.16E-03
0.4	2.63E-04	3.04E-04	6.70E-03	7.45E-03	500	2.66E-04	3.05E-04	6.90E-03	7.16E-03
0.5	2.63E-04	3.04E-04	6.76E-03	7.38E-03	600	2.66E-04	3.05E-04	6.90E-03	7.16E-03
0.6	2.63E-04	3.04E-04	6.80E-03	7.39E-03	700	2.67E-04	3.04E-04	6.91E-03	7.16E-03
0.7	2.63E-04	3.03E-04	6.82E-03	7.33E-03	800	2.68E-04	3.06E-04	6.91E-03	7.16E-03
0.8	2.63E-04	3.03E-04	6.83E-03	7.32E-03	900	2.69E-04	3.09E-04	6.92E-03	7.17E-03
0.9	2.63E-04	3.04E-04	6.85E-03	7.32E-03	1000	2.69E-04	3.07E-04	6.92E-03	7.17E-03
1	2.63E-04	3.03E-04	6.85E-03	7.27E-03	2000	2.79E-04	2.95E-04	7.02E-03	7.22E-03
2	2.63E-04	3.04E-04	6.88E-03	7.21E-03	3000	3.00E-04	3.26E-04	7.18E-03	7.35E-03
3	2.63E-04	3.04E-04	6.88E-03	7.20E-03	4000	3.26E-04	3.25E-04	7.43E-03	7.50E-03
4	2.63E-04	3.04E-04	6.89E-03	7.17E-03	5000	3.68E-04	3.59E-04	7.75E-03	7.65E-03
5	2.63E-04	3.04E-04	6.89E-03	7.19E-03	6000	4.37E-04	2.77E-04	8.18E-03	7.78E-03
6	2.63E-04	3.04E-04	6.89E-03	7.19E-03	7000	5.47E-04	1.16E-04	8.73E-03	7.83E-03
7	2.63E-04	3.04E-04	6.89E-03	7.16E-03	8000	7.05E-04	-4.78E-04	9.43E-03	7.41E-03
8	2.63E-04	3.04E-04	6.89E-03	7.17E-03	9000	9.58E-04	-2.12E-03	1.03E-02	7.15E-03
9	2.63E-04	3.04E-04	6.89E-03	7.18E-03	10000	1.35E-03	-7.16E-03	1.14E-02	4.46E-03

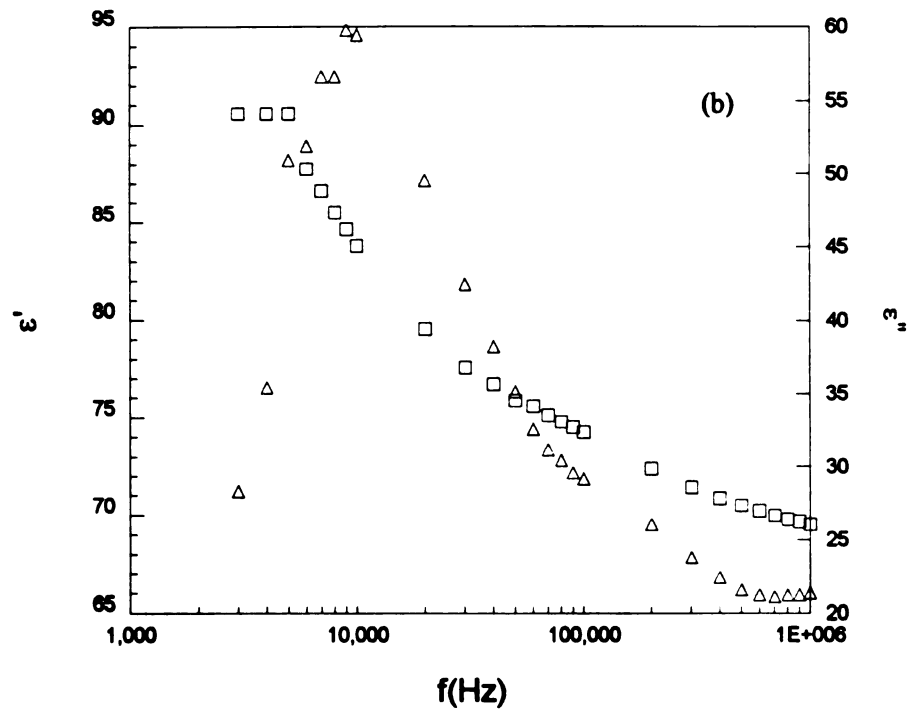
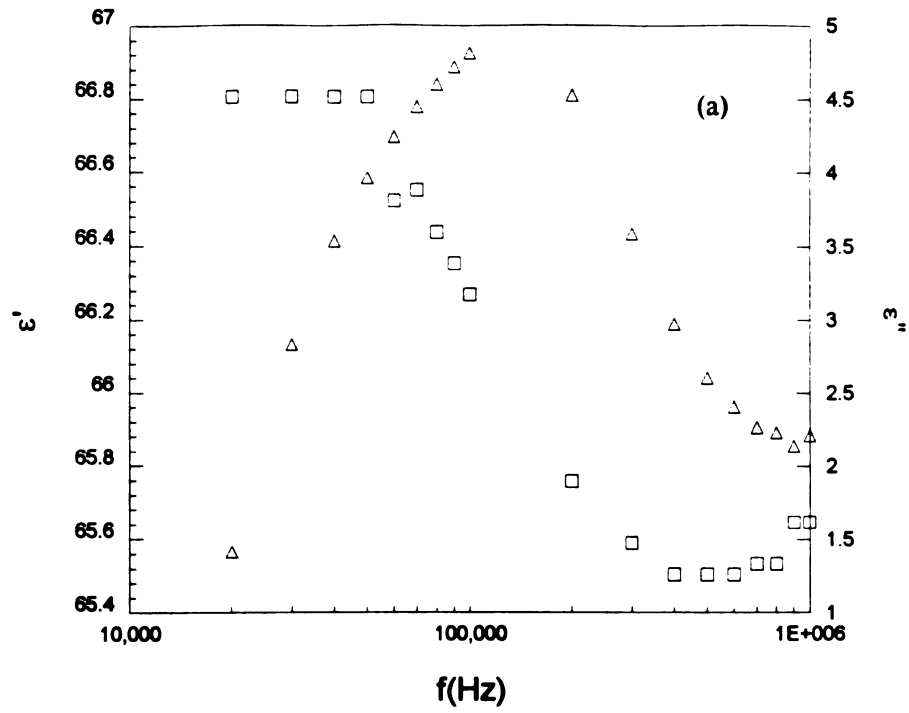


Fig.5.16: Real part(\square) and imaginary part(Δ) of dielectric constants of (a) distilled water and (b) 624.3nm suspensions with platinum black electrode.

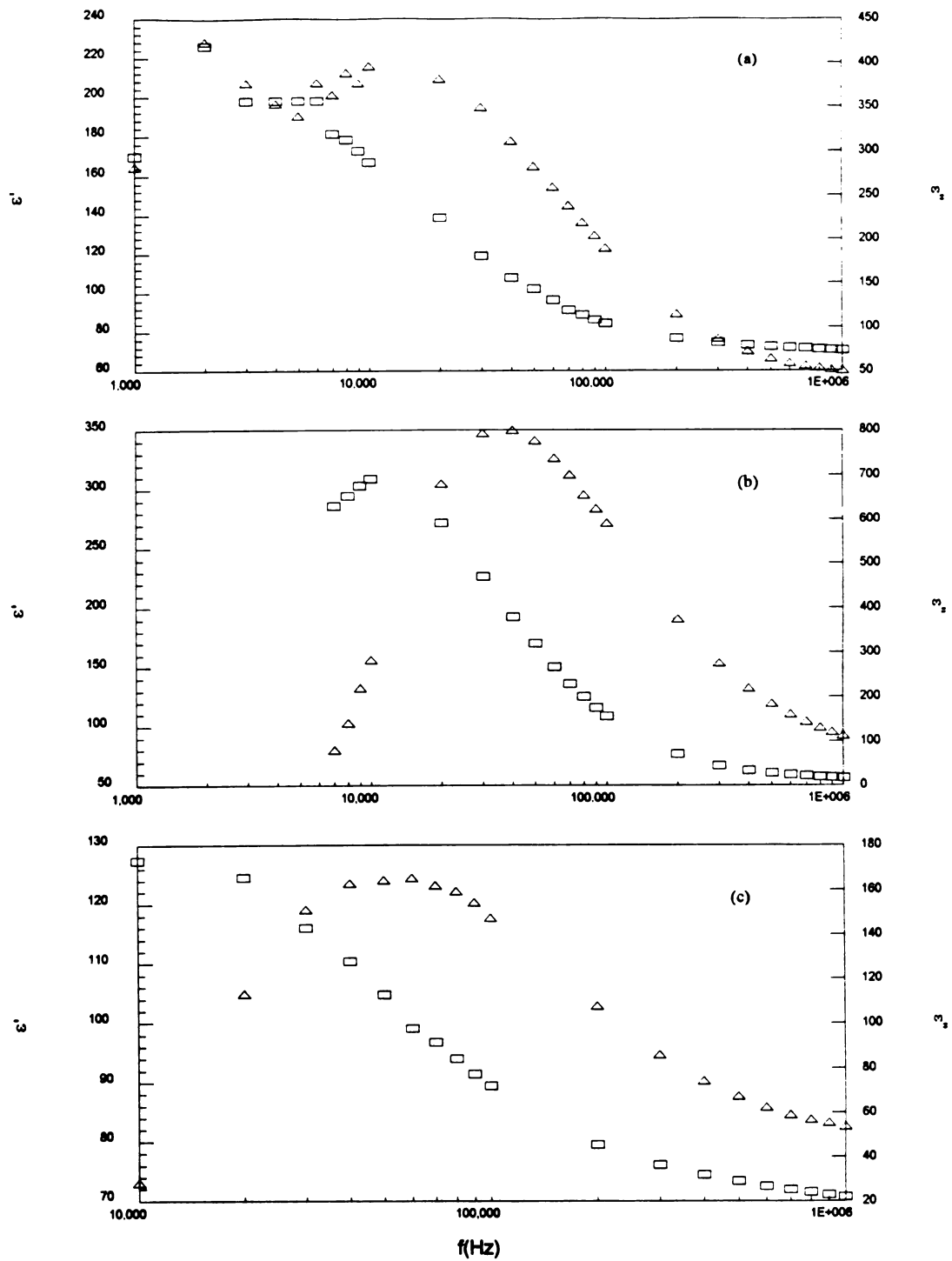


Fig.5.17: Real part(\square) and imaginary part(Δ) of dielectric constants of (a)367.7nm, (b)364.1nm and (c) 213.8nm suspensions with platinum black electrode.

We further confirm the effect of a Maxwell-Wagner term as follows. As mentioned earlier in Sec.5.2 the large resistance of the sample gives a smaller electrode effect. We may increase the total resistance between the electrodes, i.e., the total resistance of the system by covering the electrode with an insulating layer. For this purpose we covered the electrodes with scotch tape. Fig.5.18 and 5.19 show dielectric constants of several samples obtained using the brass electrode covered with tape. There is an enhancement of the real part of the dielectric constant and a loss peak in the imaginary part. The Maxwell-Wagner effect predicts such dielectric behavior for a mixture of insulating and conducting layers (See Fig.4.3).

5.5.2b Variation of measurement with time

At this point we remember the conductivity drift with time pointed out by the previous investigators[1,2,4]. They suggested that this drift may be caused by a temperature change or a coagulation of the particles during a measurements. Even a small change of conductivity can affect the dielectric behavior of the suspensions. It needs to be corrected by additional measurements to determine the time dependence. Fig.5.20 shows the time dependence of the conductivity of 1mM KCl. Neither the conductivity nor the capacitance of the sample change appreciably with time. The only change in conductivity is 0.3% during 10 minutes but the capacitance does not change at all. It is also true for the distilled water. For the suspensions, however, for frequencies <10 KHz there was a very substantial time variation as indicated in Figs.5.21 and 5.22. Because the change in suspensions is much larger than that in a pure electrolyte we conclude that the time variation is associated with the suspended microspheres, -possibly with coagulation- rather than with a temperature change.

Figs.5.21 and 5.22 illustrates the time variations of 624.3nm suspensions at two different electrode separations. For the capacitance the time dependence is frequency dependent for $f < 10$ KHz. At 0.1 KHz it is particularly severe, and for $f > 10$ KHz it is

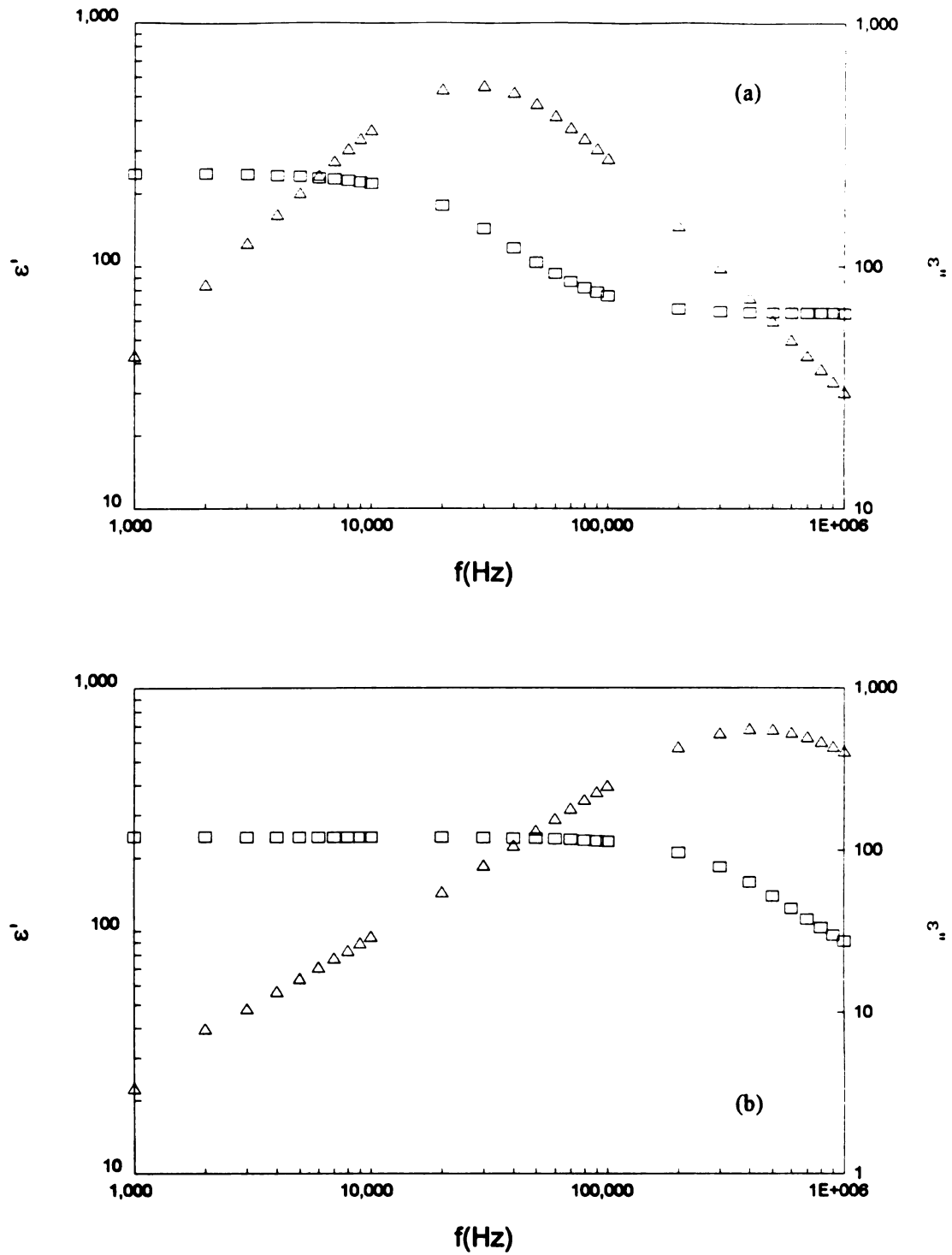


Fig.5.18: Real part(\square) and imaginary part(Δ) of dielectric constant of (a) distilled water and (b) 1mM KCl solution with brass electrode covered with tape.

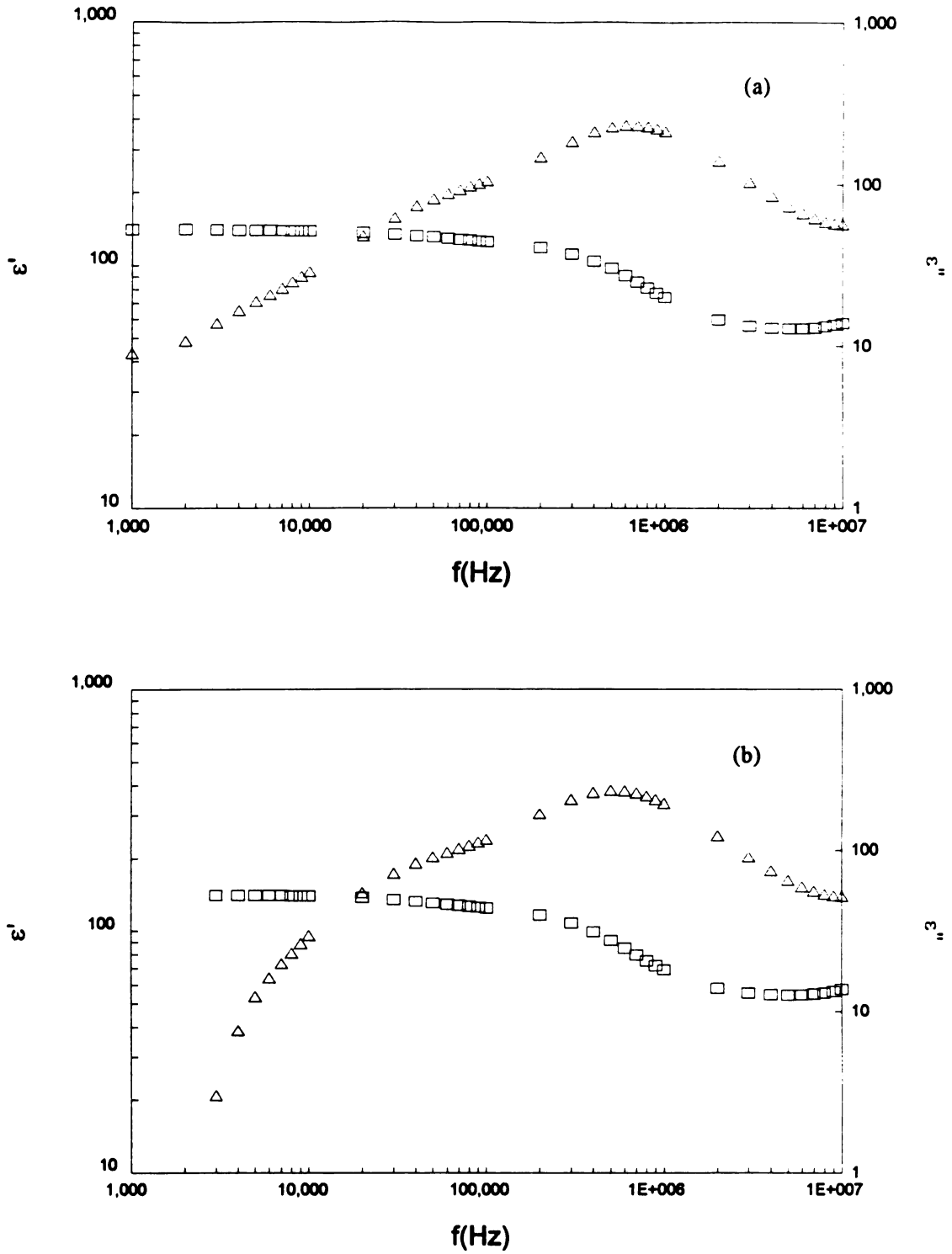


Fig.5.19: Real part(\square) and imaginary part(Δ) of dielectric constants of (a) 367.7 nm and (b) 364.1nm suspensions with brass electrode covered tape.

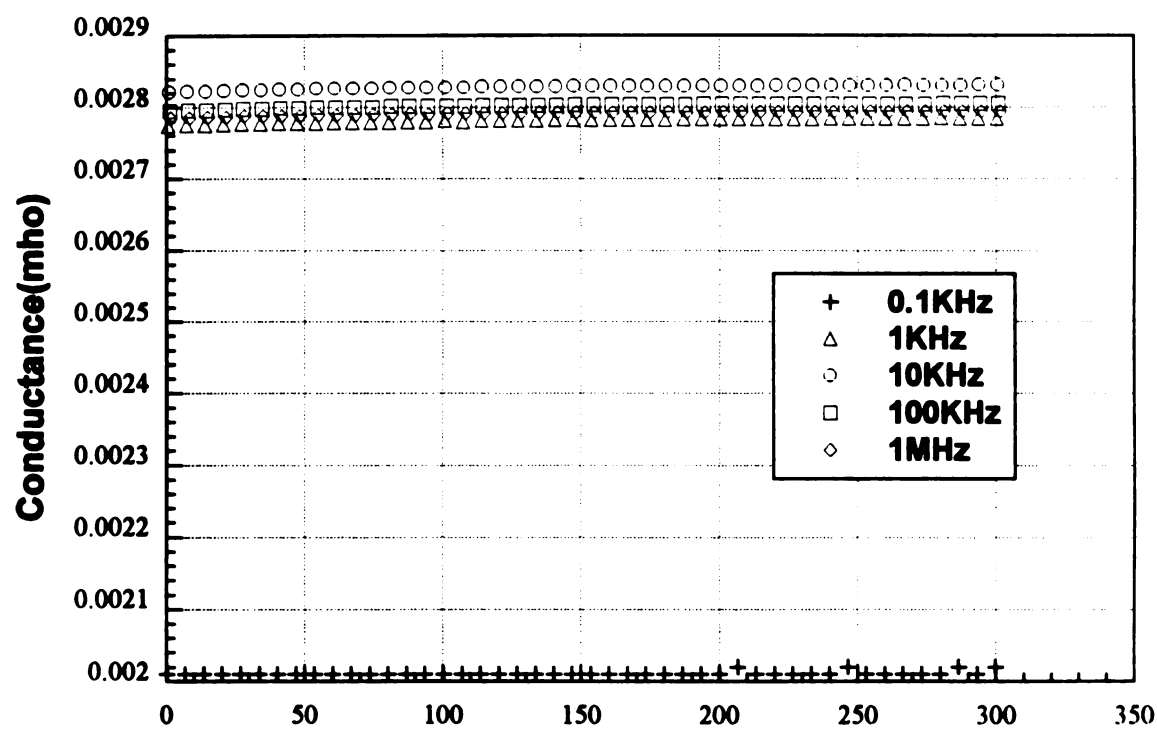
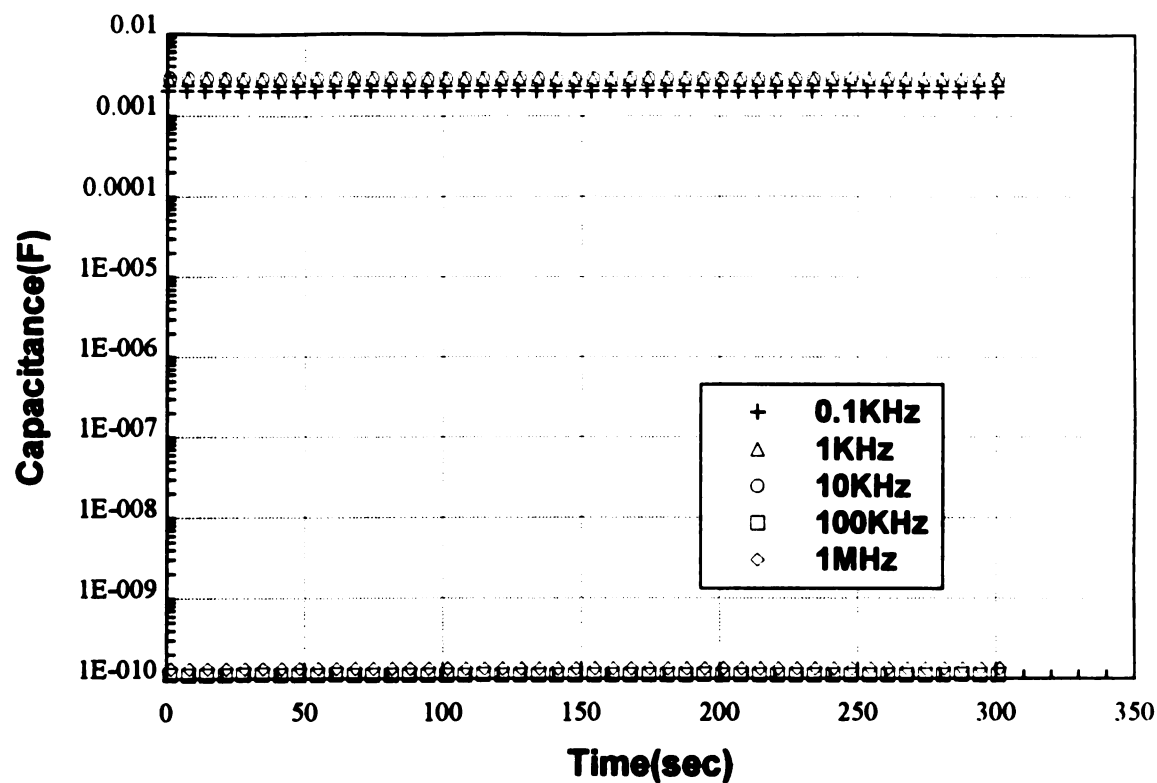


Fig.5.20: Time variation of dielectric behavior of 1mM KCl solution using small cell with Pt electrodes.

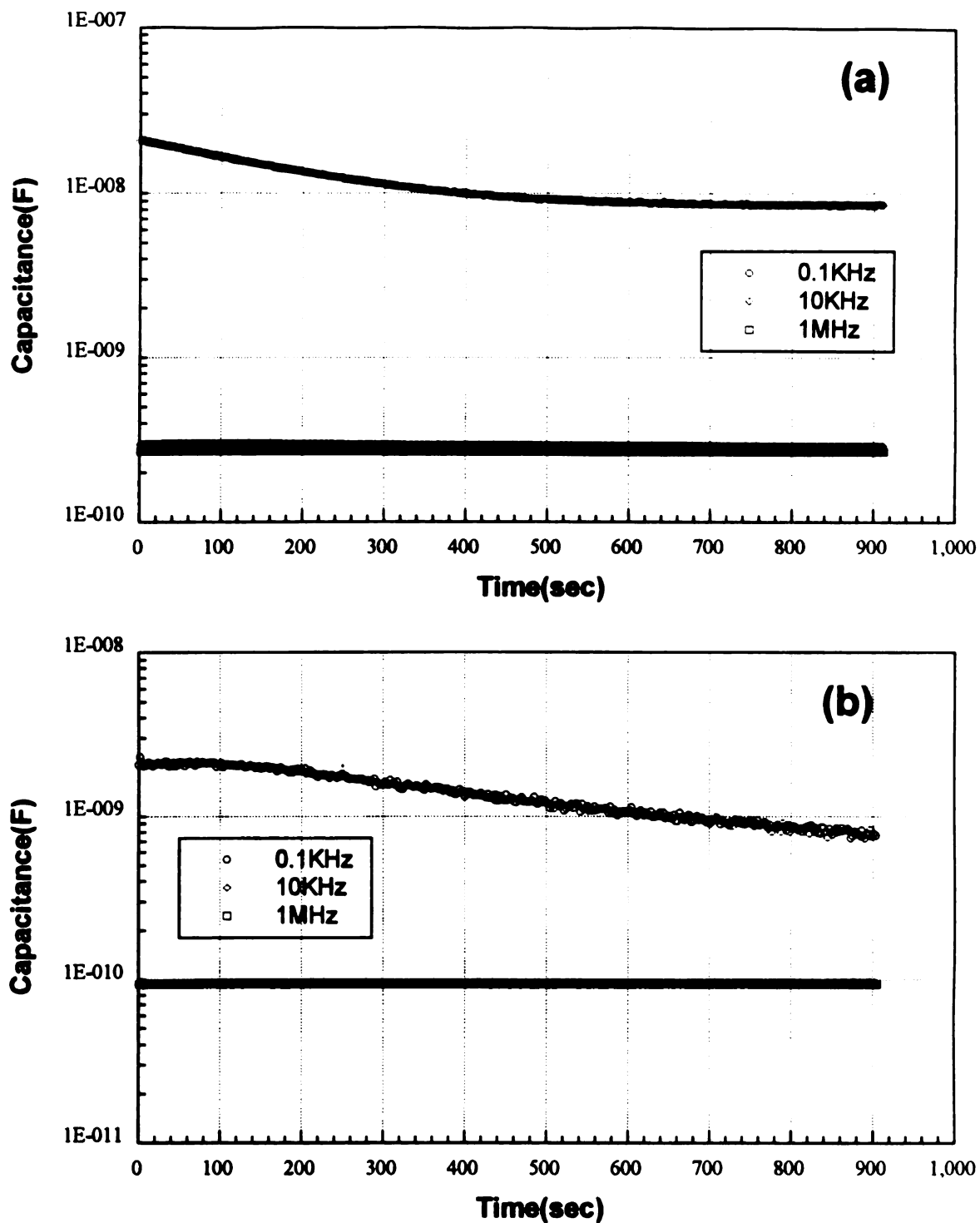


Fig.5.21: Time variation of capacitance of 624.3nm suspensions at (a) 5mm and (b) 7.6mm using Pt electrodes. For clarity only the data for 3 of the 5 frequencies studied are shown.

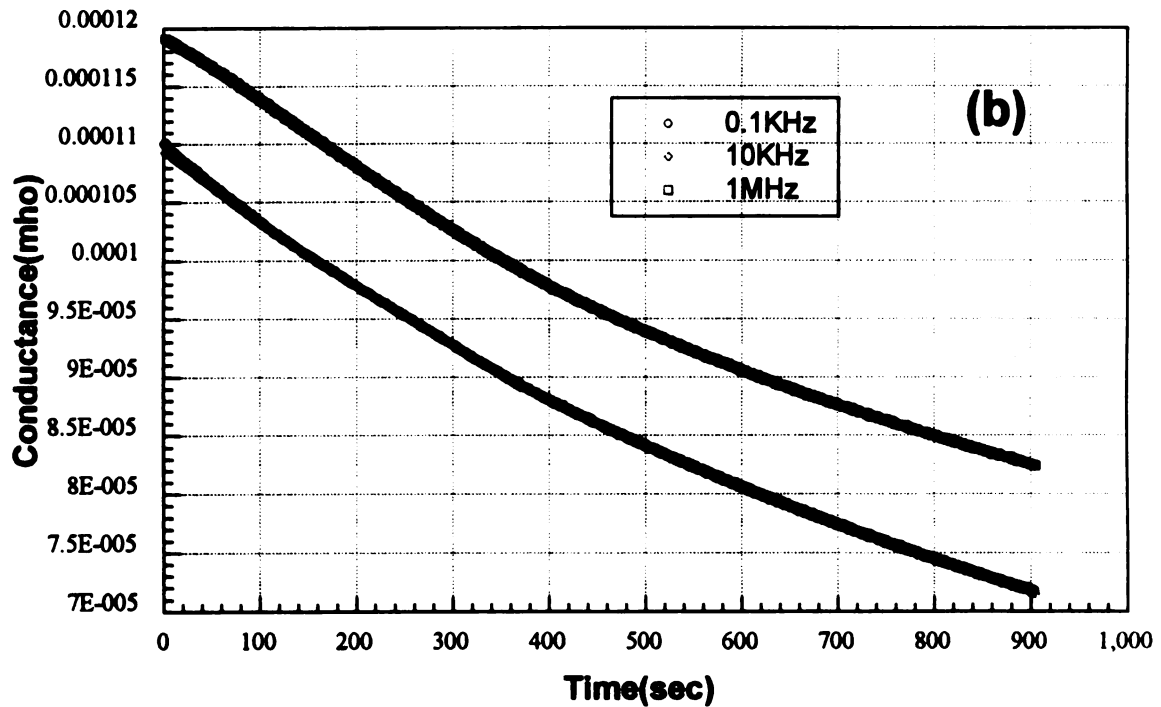
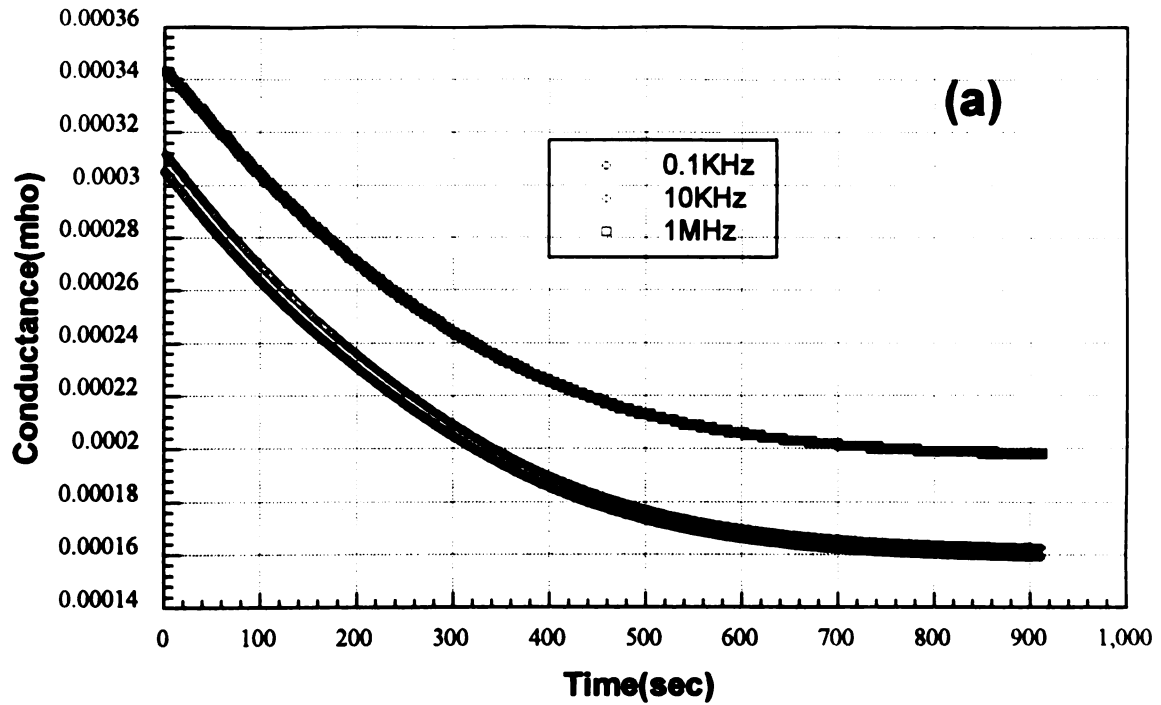


Fig.5.22: Time variation of the conductance of 624nm suspensions at (a) 5mm and (b) 7.6mm using Pt electrodes. For clarity only the data for 3 of 5 frequencies studied are shown.

negligible. In the conductance the time dependence is severe at all frequencies. The time dependence also depends on electrode spacing. Thus it is almost impossible to make a time correction and since the variation within a few minutes is very rapid it is difficult to initialize the time compensation.

5.5.2c Sand blasted electrode

At this stage we remembered the recommendation of Springer and Lyklema regarding sand-blasted electrodes, and as a last resort we performed measurements to see whether their use would reduce the electrode polarization and time variation problem. Since the Pt electrode on the present cell was too thin for sandblasting a new cell with different dimensions was made to accommodate a thick sand-blasted electrode. Fig.5.23 show the time variation of 213.8nm suspensions for a continuously applied field(line) and for an intermittent applied field. The intermittent measurements were performed by measuring 5 frequencies quickly(about 2 seconds) at a mean time and then repeating there at a second mean time and so on. After the intermittent measurement were finished a new sample of the same suspension was found and measured quasi-continuously. The line is a computer drawn line through the experimental points. Initially the variation with time is rapid and this means that the starting points of the 2 curves are different. If we shift the curves so that the capacitance value is the same at $t=0$, then the conclusion is that a substantial portion of the time dependence is associated with the application of an electric field. That is electrophoresis is present, as well as coagulation. Electrophoresis is diminished by the use of small fields. Thus we endeavored to do using an applied voltage of 100 mV. Figs.5.24 and 5.25 show the time variations of 624.3nm suspensions at two different electrode separations. Again the time variations are different at each separation and at each frequency and even worse than that using Pt electrodes. Figs.5.26 and 5.27 show the time variation of the capacitances and conductances of four suspensions using sand-blasted electrodes at 1.3mm electrode separation. The time variation of conductance

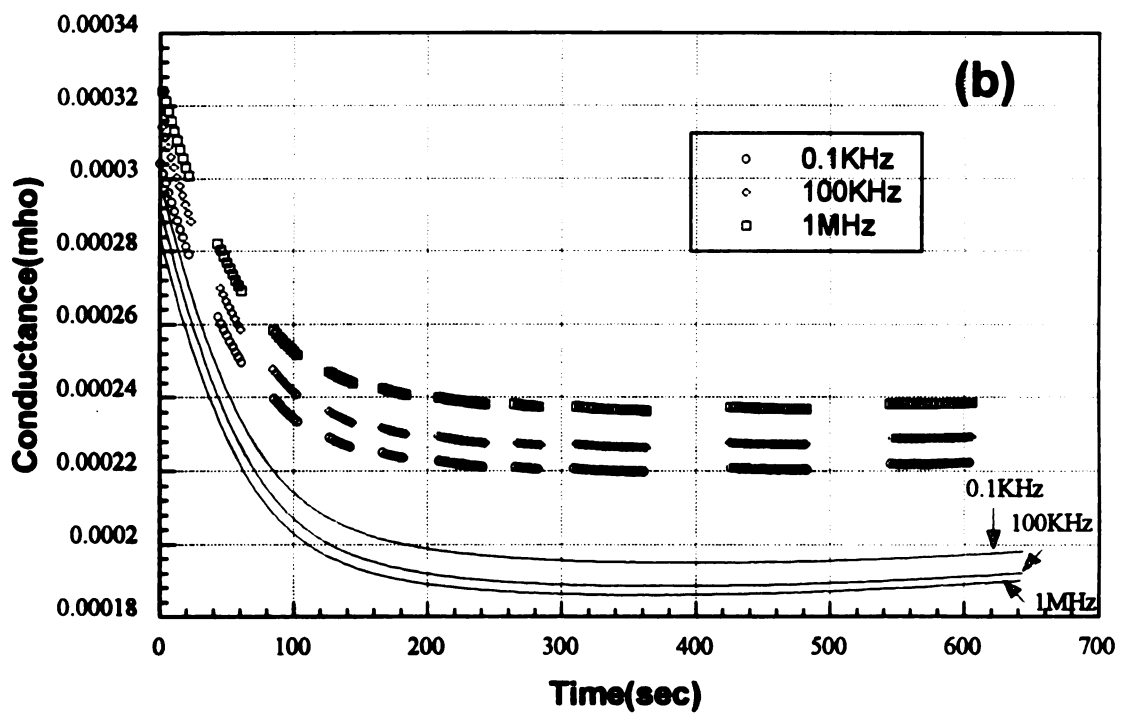
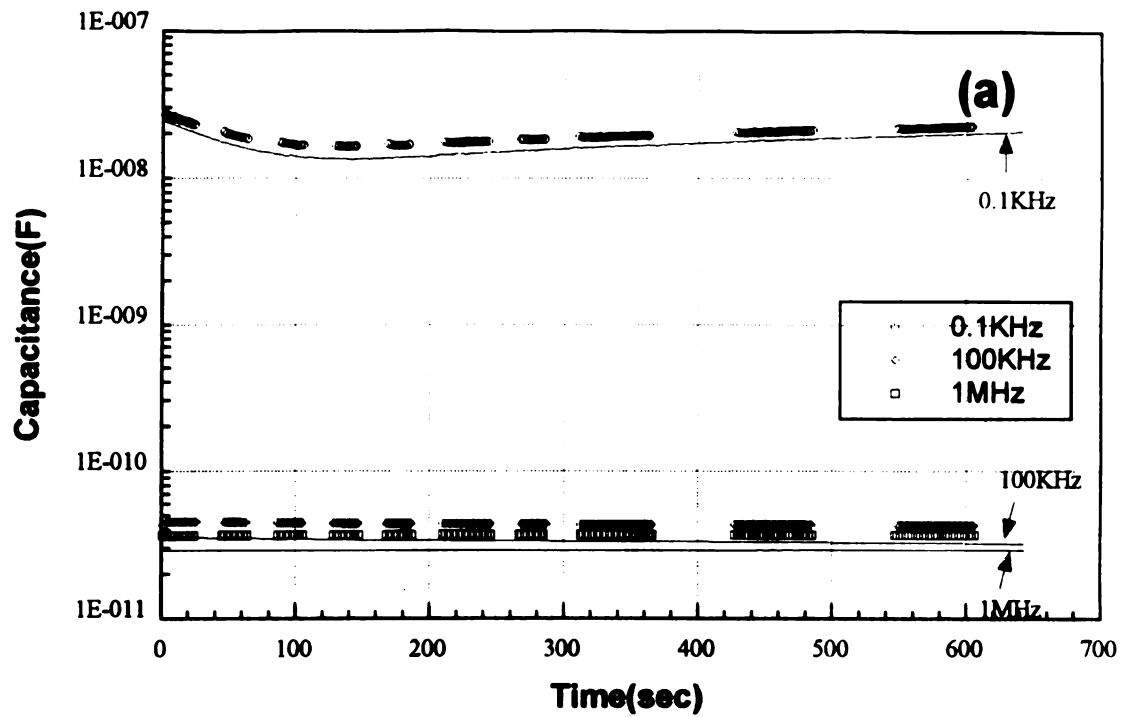


Fig.5.23: Time variation of 213.8nm suspensions with sand blasted electrodes at 1.9mm separation. For clarity only the data for 3 of the 5 frequencies studied are shown.

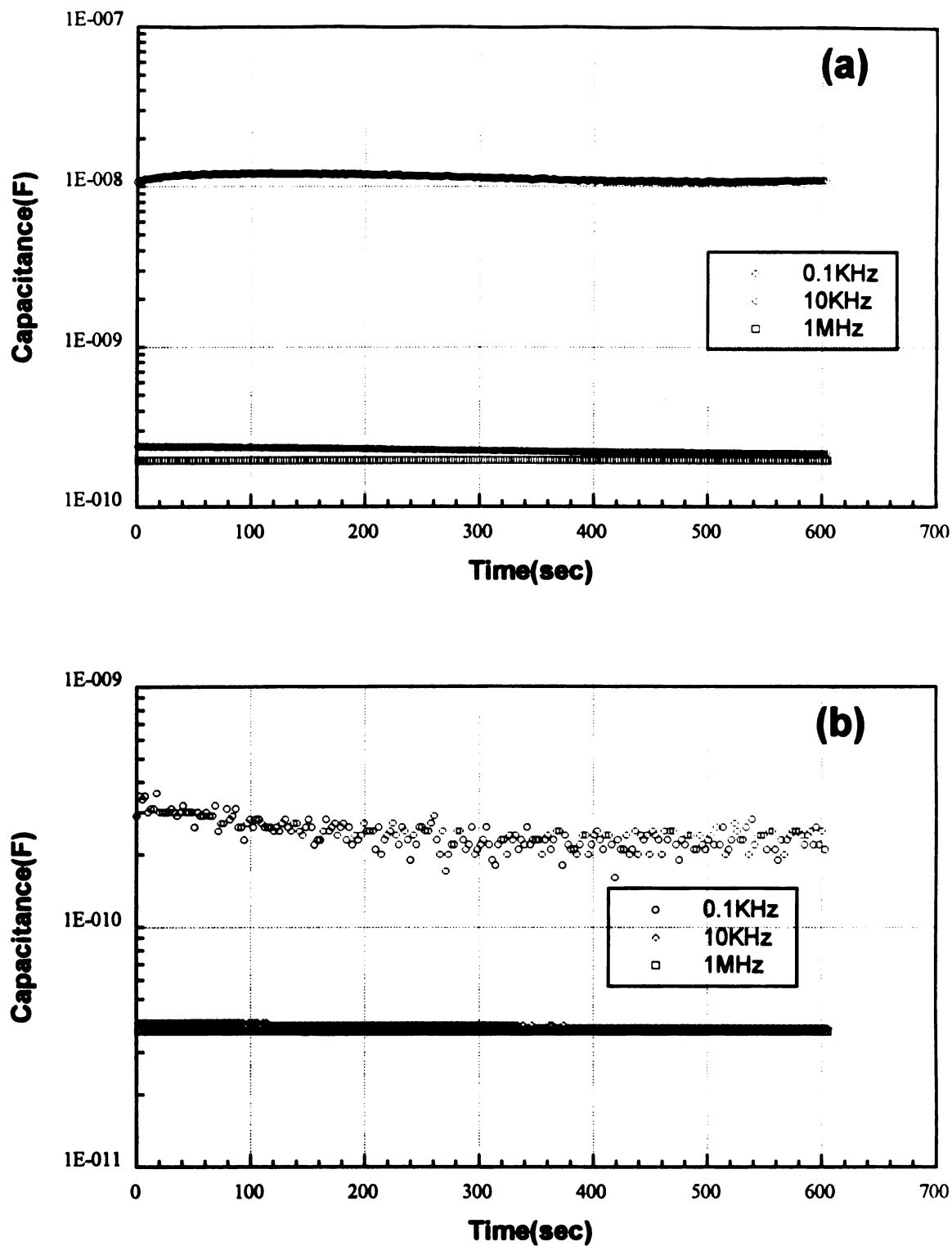


Fig.5.24: Time variation of capacitance of 624.3nm suspensions at (a) 0.6mm and (b) 1.9mm using sand-blasted Pt electrodes. For clarity only the data for 3 of the 5 frequencies studied are shown.

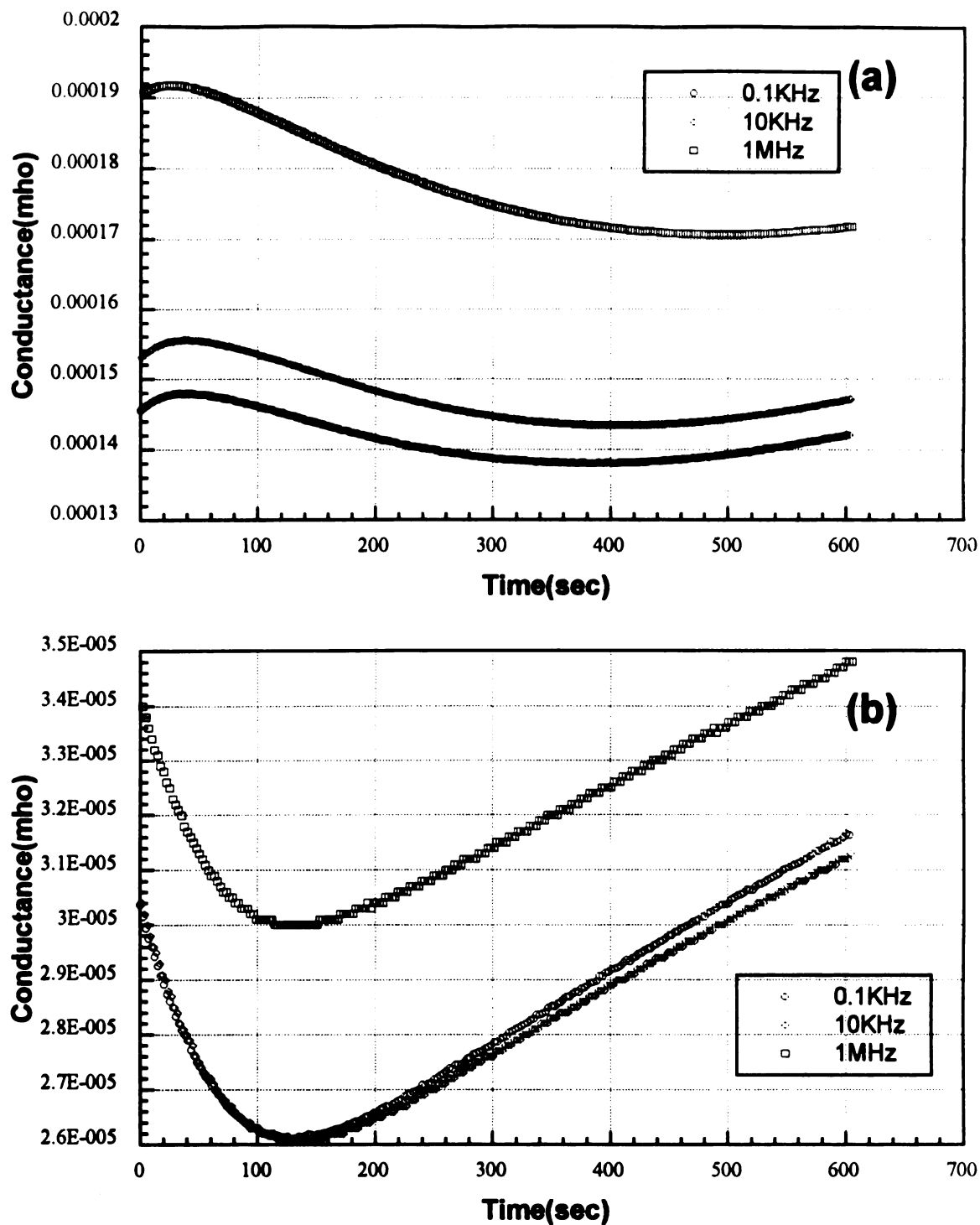
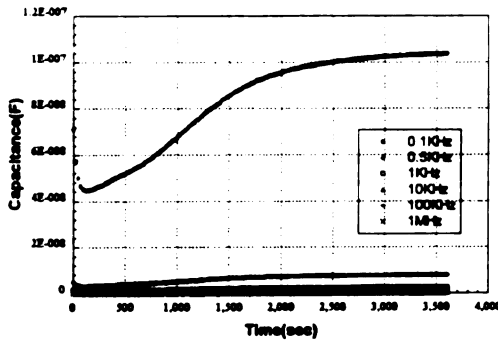
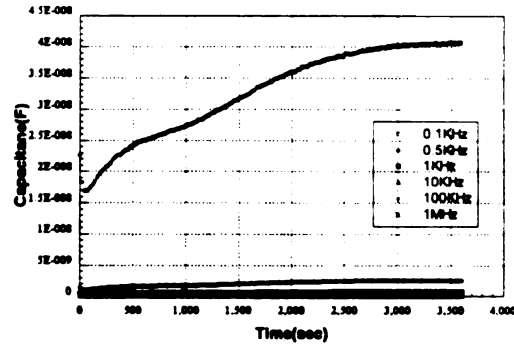


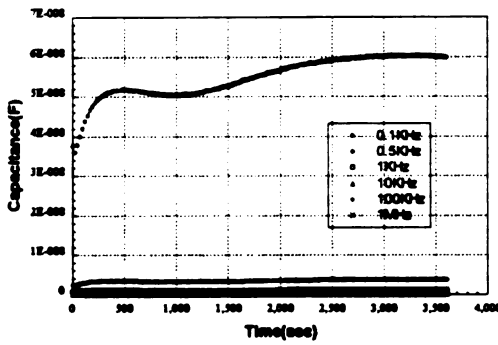
Fig.5.25: Time variation of conductance of 624.3nm suspensions at (a) 0.6mm and (b) 1.9mm using sand-blasted Pt electrodes. For clarity only the data for 3 of the 5 frequencies studied are shown.



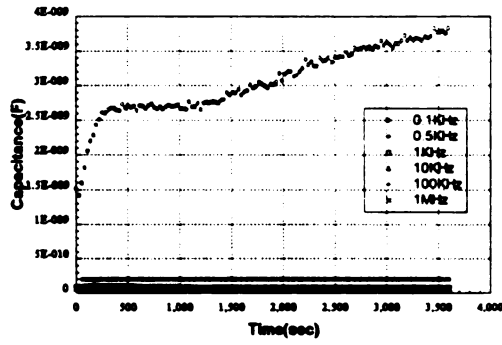
(a)



(b)

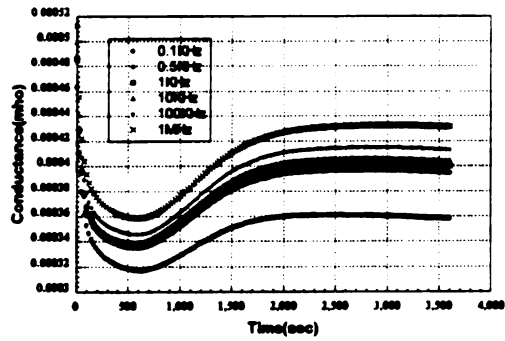


(c)

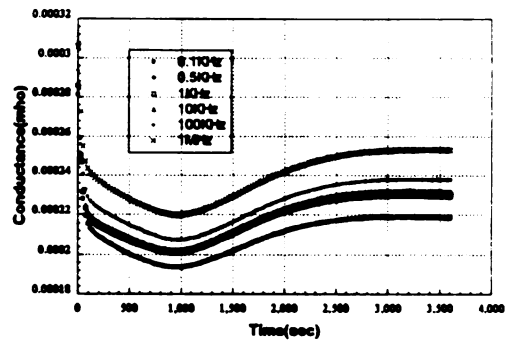


(d)

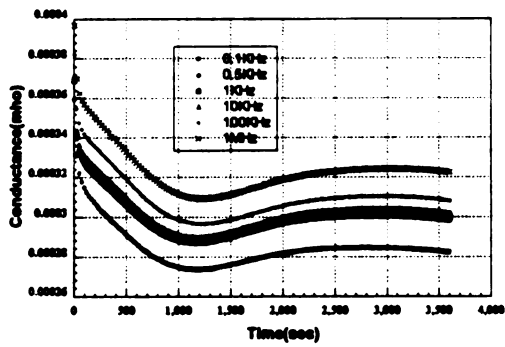
Fig.5.26: Time variation of the capacitances of suspensions of (a) 213.8nm, (b) 364.1nm, (c) 367.7nm and (d) 624.3nm using sand-blasted Pt electrodes at 0.05" separations.



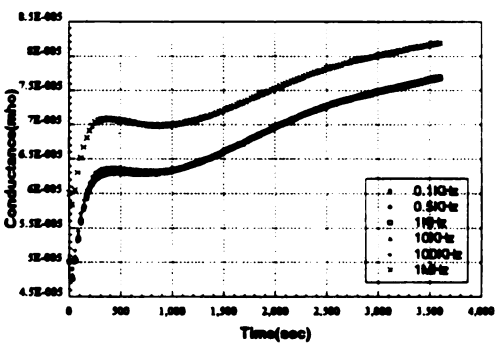
(a)



(b)



(c)



(d)

Fig.5.27: Time variation of the conductances of suspensions of (a) 213.8nm, (b) 364.1nm, (c) 367.7nm and (d) 624.3nm using sand-blasted Pt electrodes at 0.05" separations.

seems to be independent of frequency but that of capacitance is dependent on the frequency. The dielectric behavior is illustrated in Fig.5.28. At low frequencies the electrode effect is still dominant and the dielectric constant is large compared to the Pt electrode results on those obtained by other investigators. The imaginary parts of the experimental results indicate that none of suspensions have dielectric loss peaks. At around 2 KHz they seem to have loss peaks but they are not the real loss peaks.

5.5.2d Results with Pt electrode

Finally we returned to the Pt electrodes which seemed to have the best properties. Due to the timing difficulties the actual measurements were made after one hour when the suspension is stabilized. Until we know the nature of the time variation, this means we do not really know the nature of this stable state. Fig.5.29(a) shows the conductivity of 367.7nm suspensions vs. frequency. From 100 Hz to 1 MHz the conductivity increases gradually but very slightly with frequency. The conductivity increase is more rapid in the frequency range between 10 KHz and 100 KHz, where the dielectric loss peak is expected. Here we are faced by the last major problem. The part of the conductivity associated with dielectric loss is that associated with the AC conductivity. Therefore the DC component of the conductivity is somehow to be subtracted from the measured conductivity. The choice of DC conductivity is not easy because the conductivities below 1 KHz are not approaching a single limit value and DC measurements present an decreasing conductivity with time. Therefore the choice of DC conductivity critically affects the deduced imaginary part of the dielectric constant. Fig.5.29(b) shows the imaginary part of 367.7nm suspensions calculated from different choices of DC conductivity. For the best result we chose the conductivity at 1 KHz as DC conductivity. Therefore, to get the experimental imaginary part of each dielectric constant the following relationship was used

$$(\sigma(\omega) - \sigma(1\text{KHz})) / \omega \text{ . Here } \sigma \text{ is conductivity.}$$

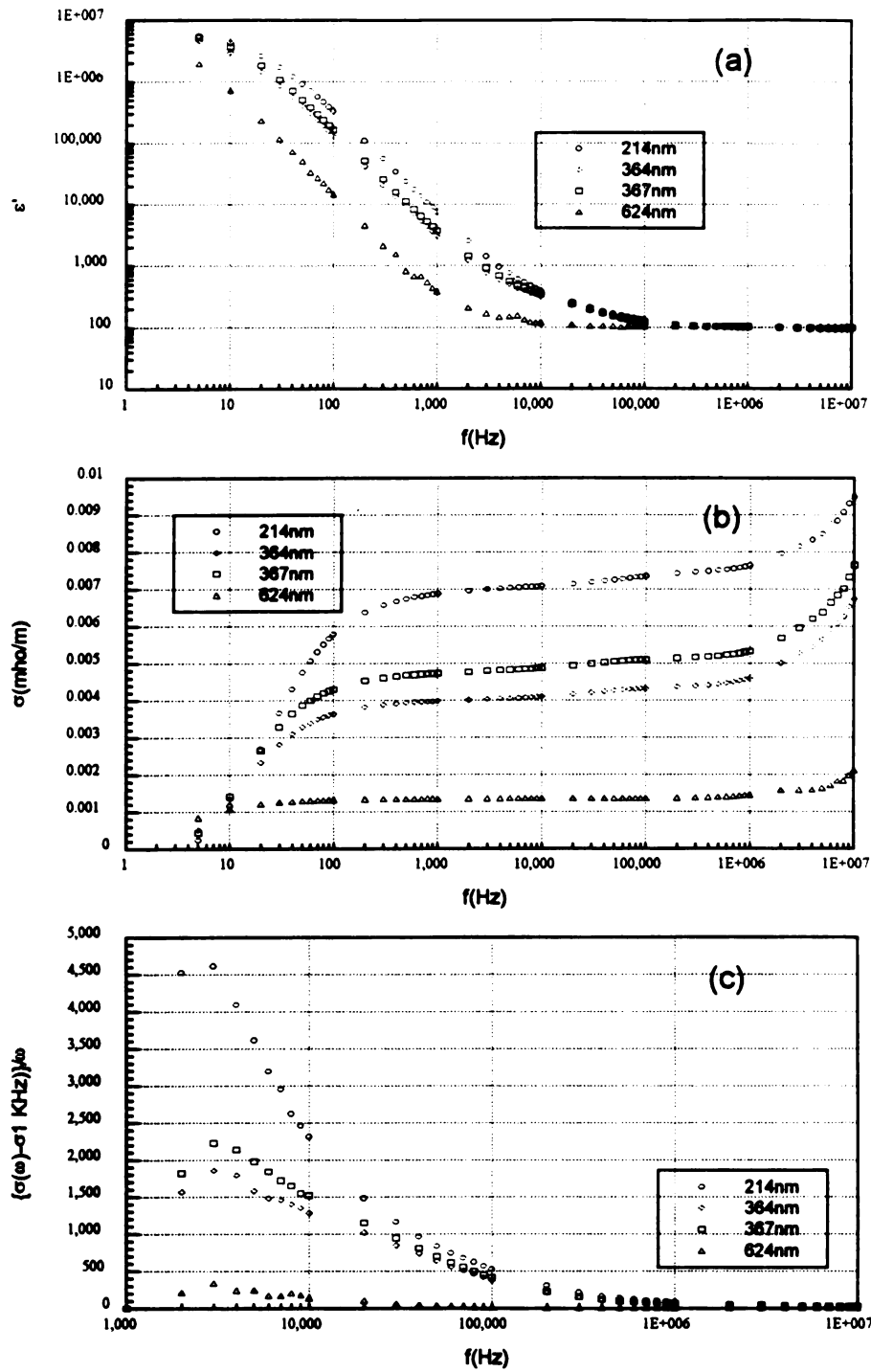


Fig.5.28: (a) Real parts , (b) conductivities and (c) imaginary parts of suspensions using sand-blasted Pt electrodes.

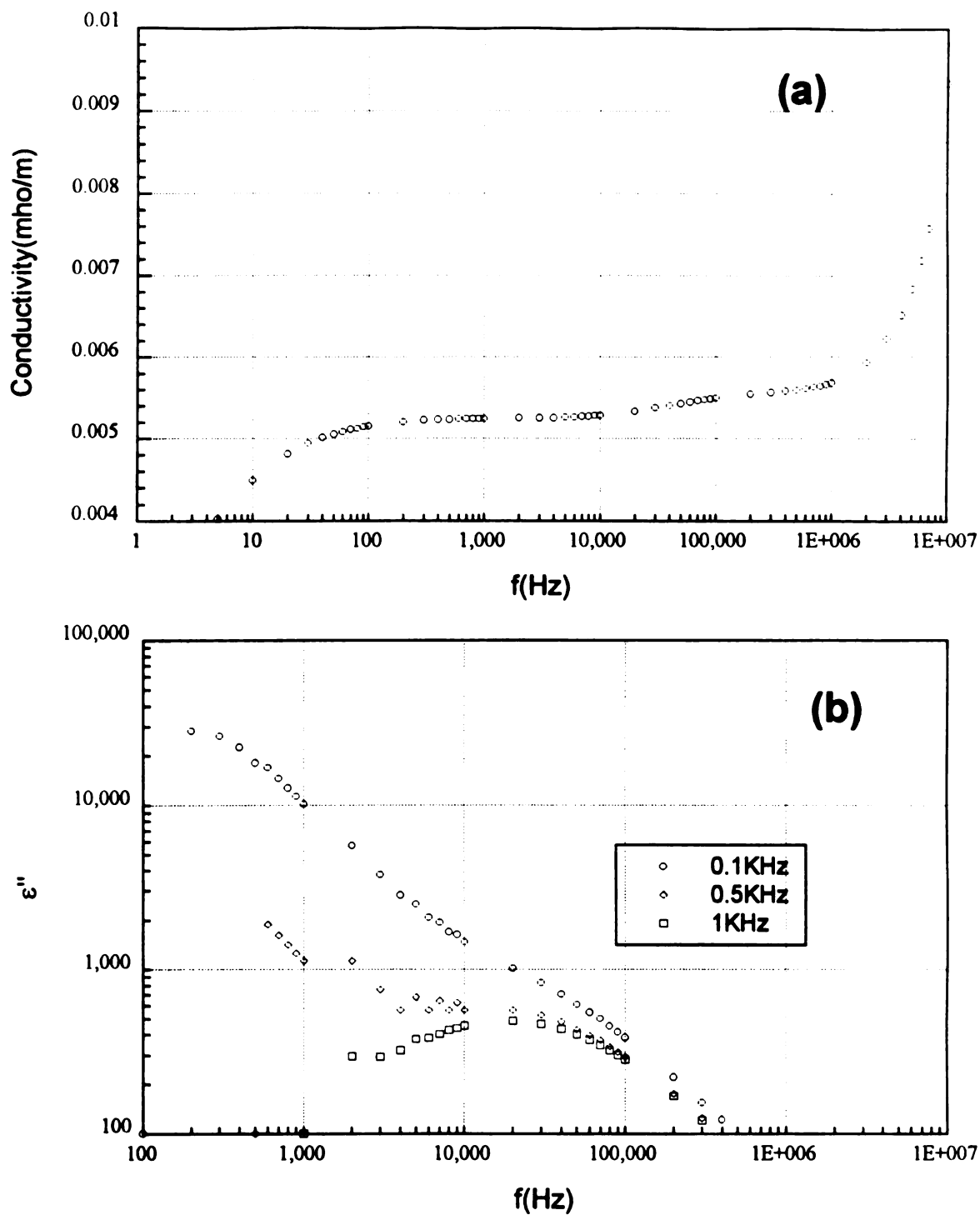


Fig.5.29: (a) The conductivity of 367.7nm suspensions vs. frequency. (b) The imaginary part of 367.7nm suspensions with choice of different DC conductivity. The numbers in the legend correspond to the frequencies where the DC conductivity was taken.

Fig.5.30 to Fig.5.33 illustrate the dielectric behavior of four different suspensions with the theoretical predictions using Sen's theory (solid lines). The data below 0.1 KHz and above 1 MHz should be rejected due to the inappropriateness of the cell and the analysis method. The fitting parameters are same as Sen used with Schwan et al.'s data except Ψ_0 and the volume fraction of balls. Ψ_0 was varied to optimize the fit of experiment to theory. $\Psi_0=4.78, 5.38, 5.5$, and 4.28 were used for 213.8nm , 364.1nm , 367.7nm , and 624.3nm suspensions respectively.

Comparing the experimental results and the theoretical predictions the imaginary parts are very close each other but there are large differences in the real parts. Especially the characteristic frequencies obey the relationship given by Sen very well. In Sen's theory the characteristic frequency depend only on the size of the particles $\omega \propto 1/a^2$. The characteristic frequency against the inverse of the square of the particle size is plotted in Fig.5.34. The linear behavior indicates that the experimental results agree with the theory. At very low frequencies dielectric constants of the experimental results are enormously large due to the electrode polarization effects. In this experimental method and interpretation the electrode effect may be reduced a little.

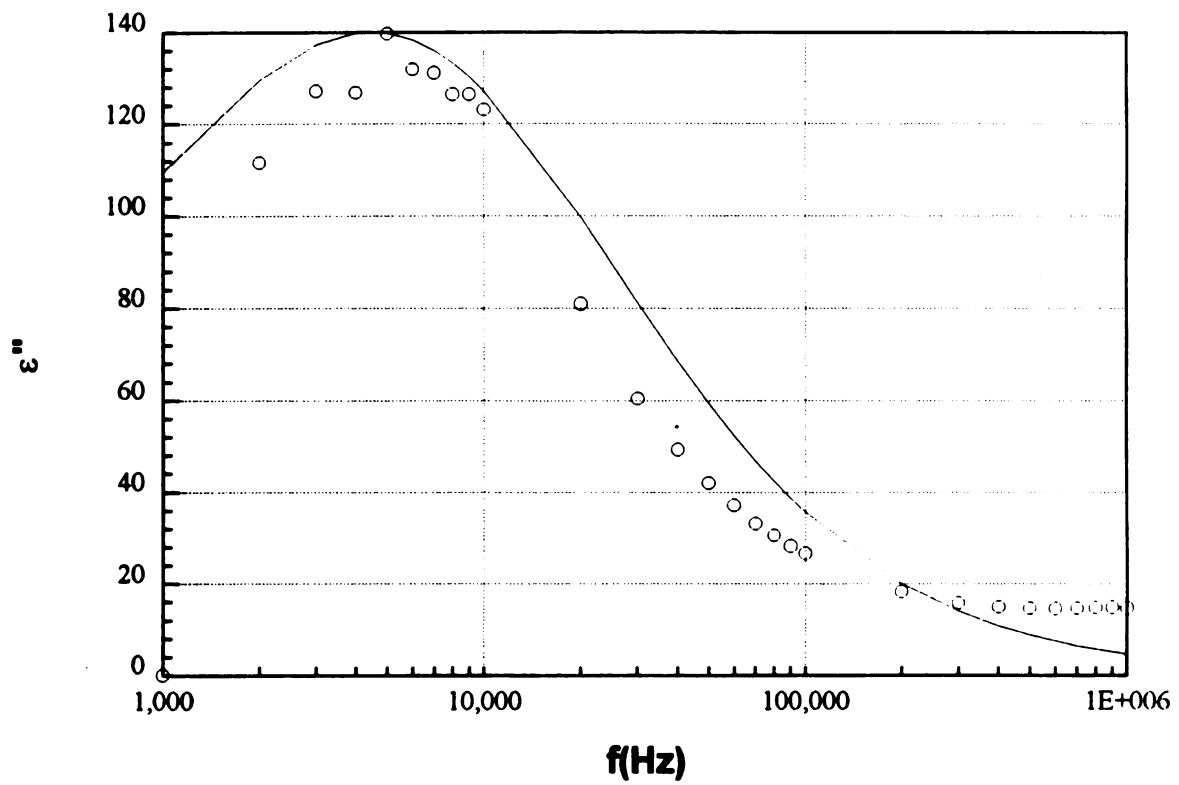
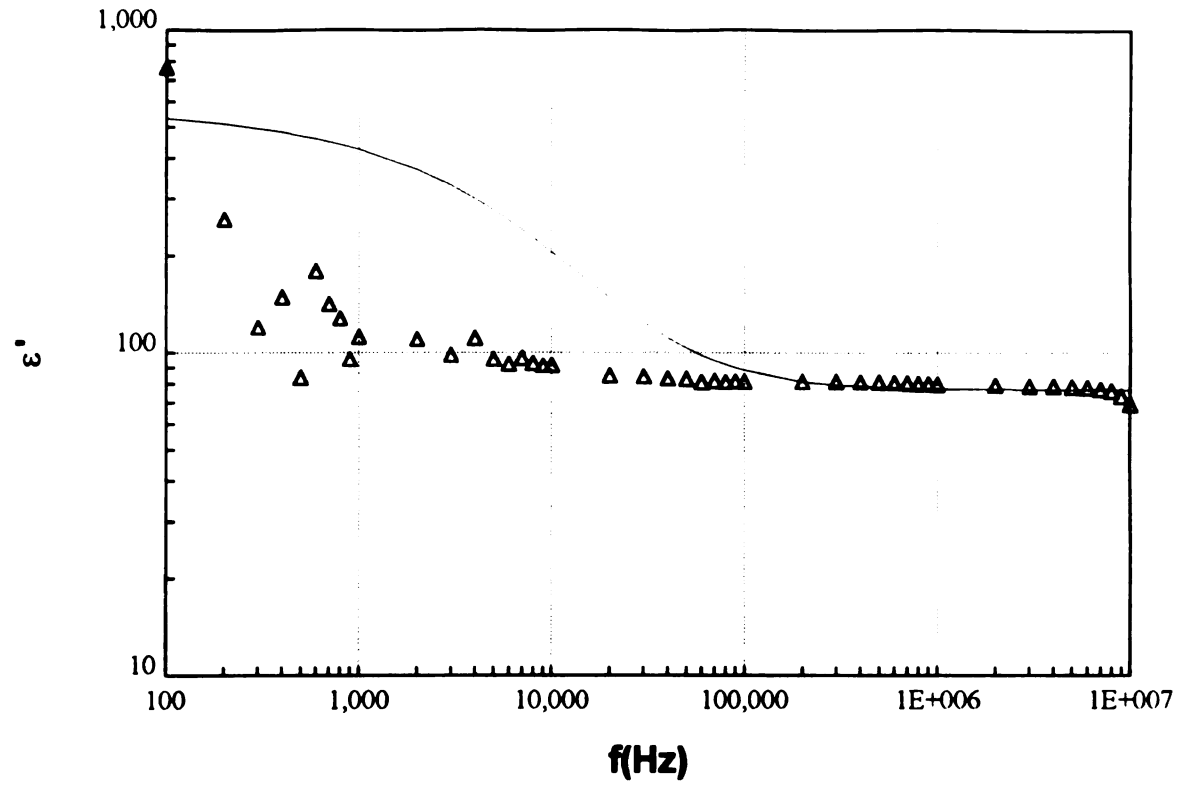


Fig.5.30: Dielectric behavior of 624.3nm suspension using small cell with Pt electrodes.

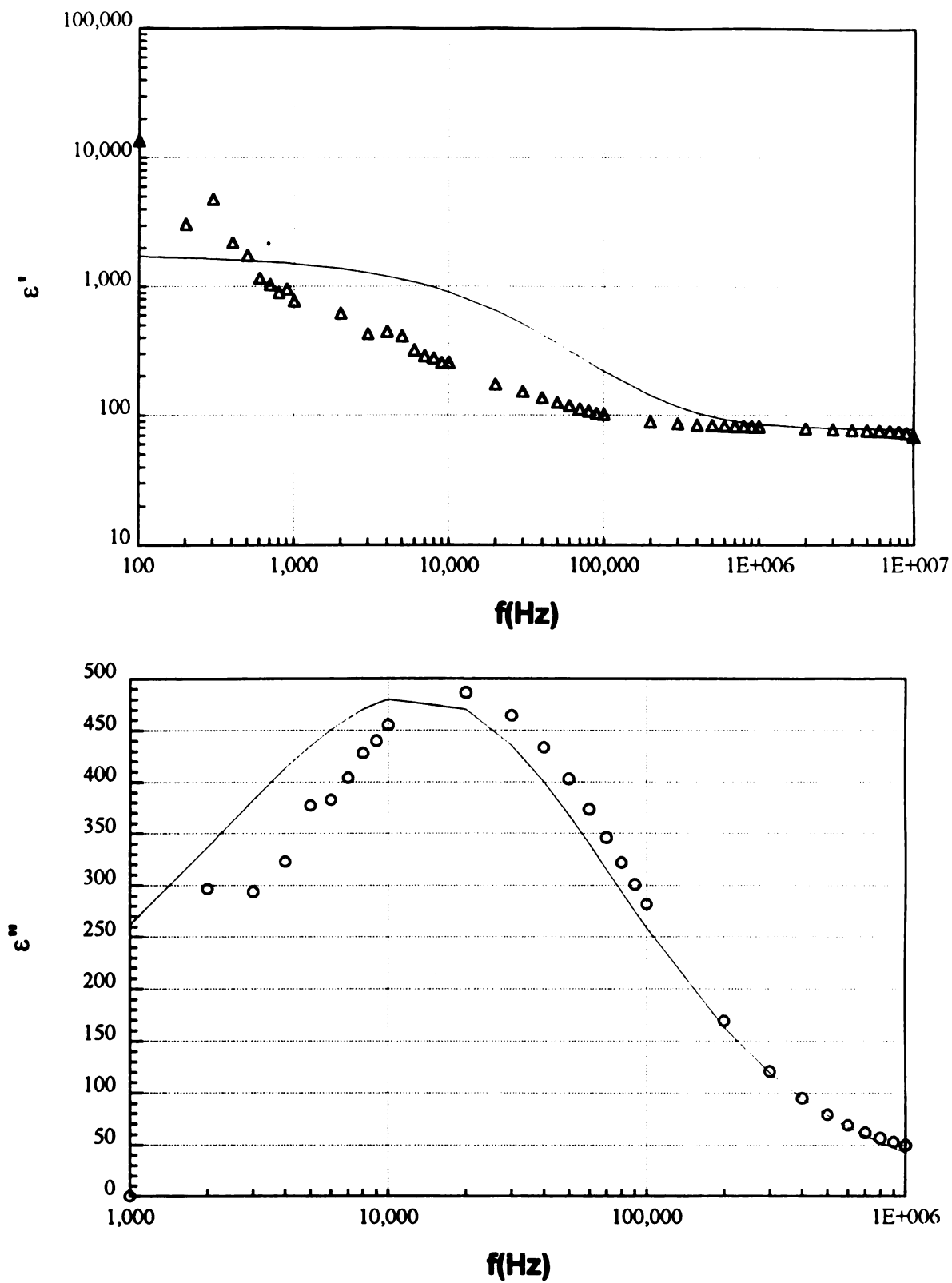


Fig.5.31: Dielectric behavior of 367.7nm suspension using small cell with Pt electrodes.

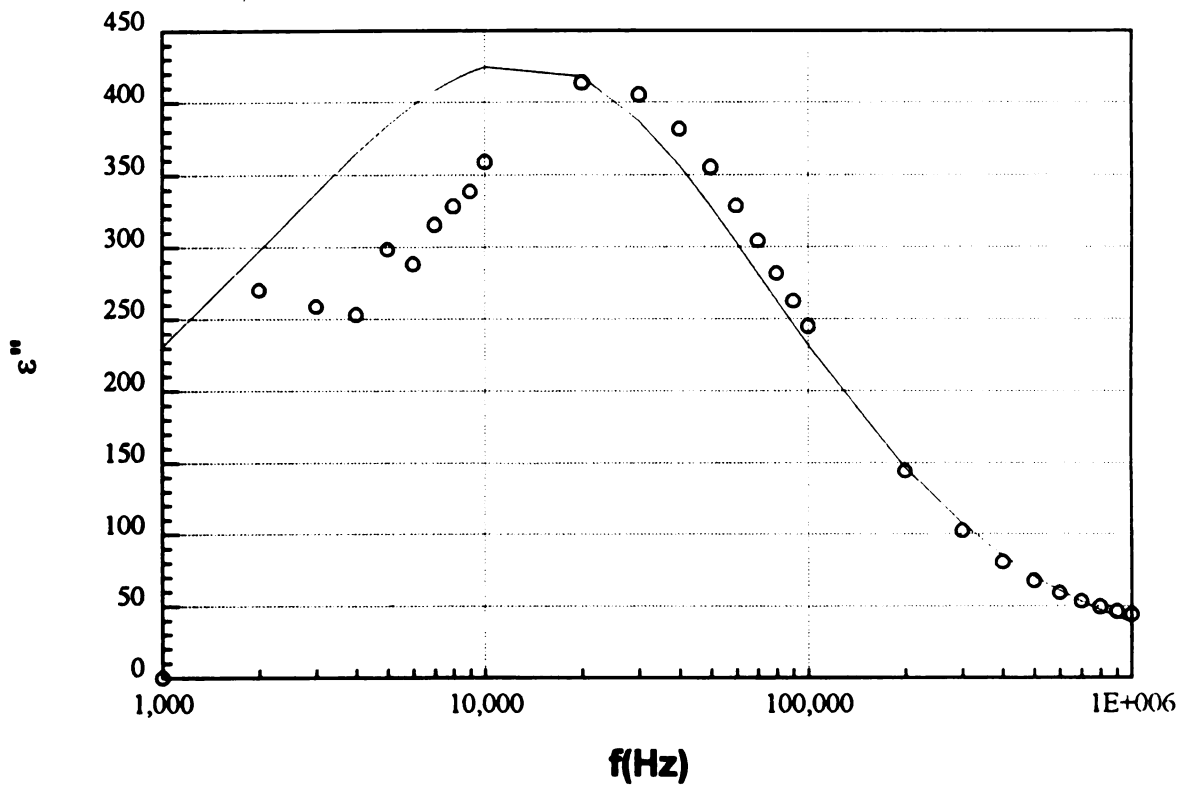
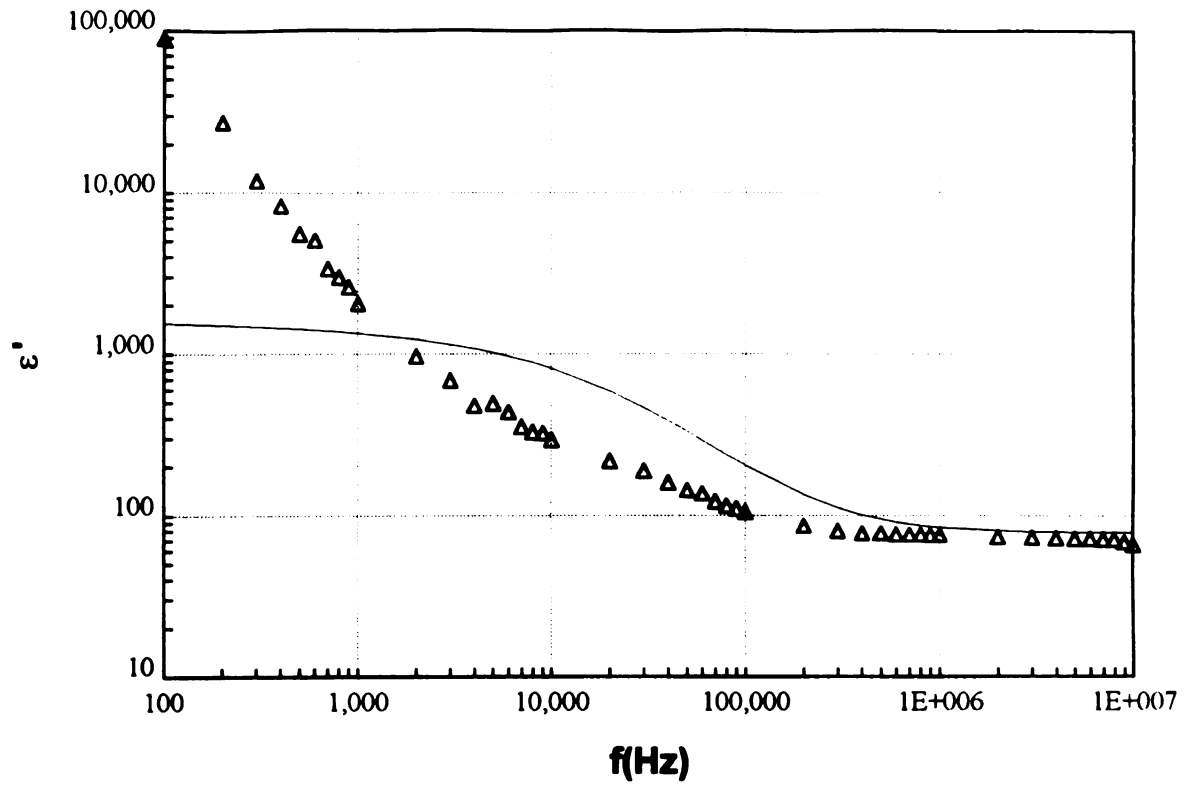


Fig.5.32: Dielectric behavior of 364.1nm suspension using small cell with Pt electrodes.

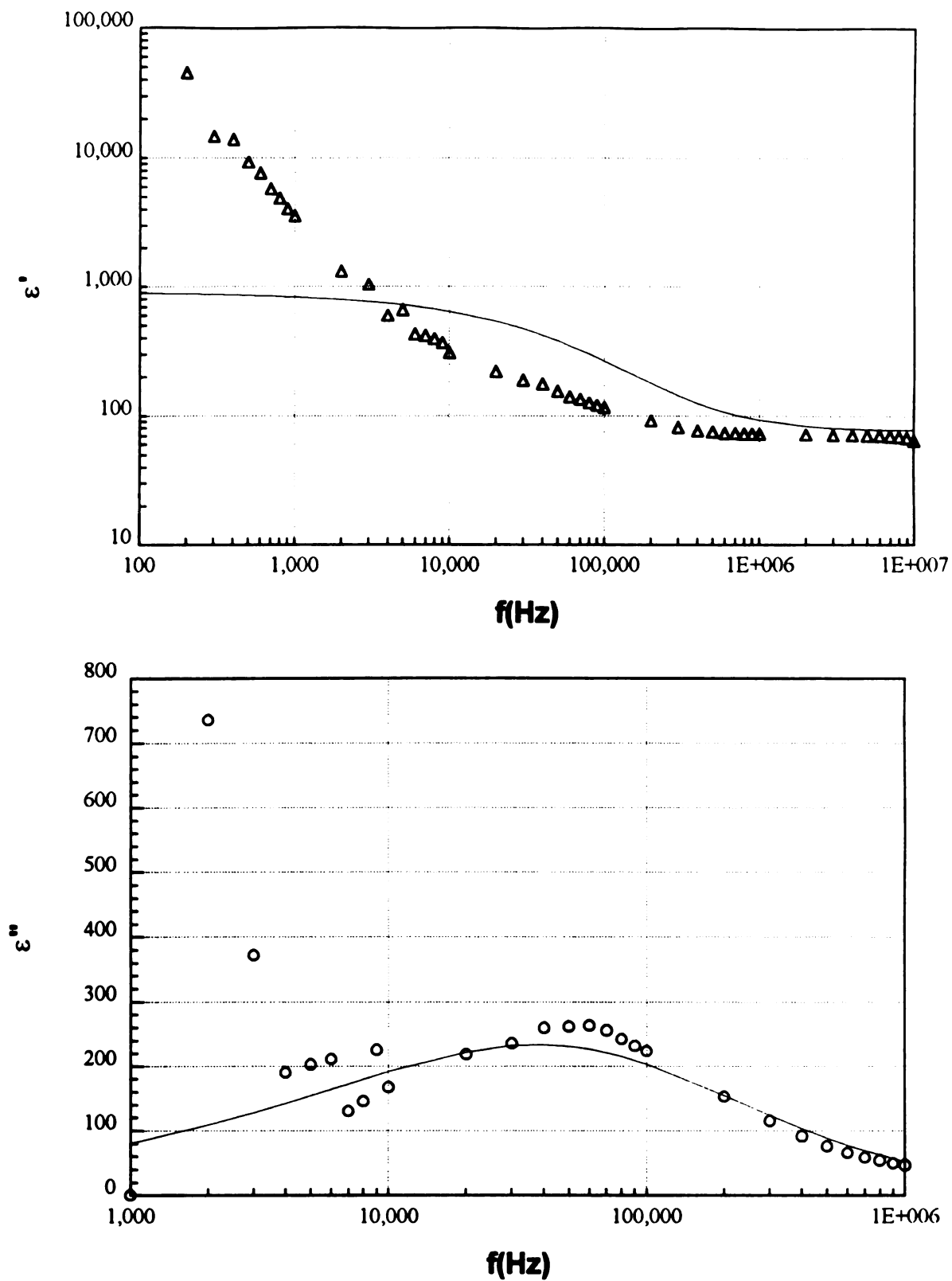


Fig.5.33: Dielectric behavior of 213.8nm suspension using small cell with Pt electrodes.

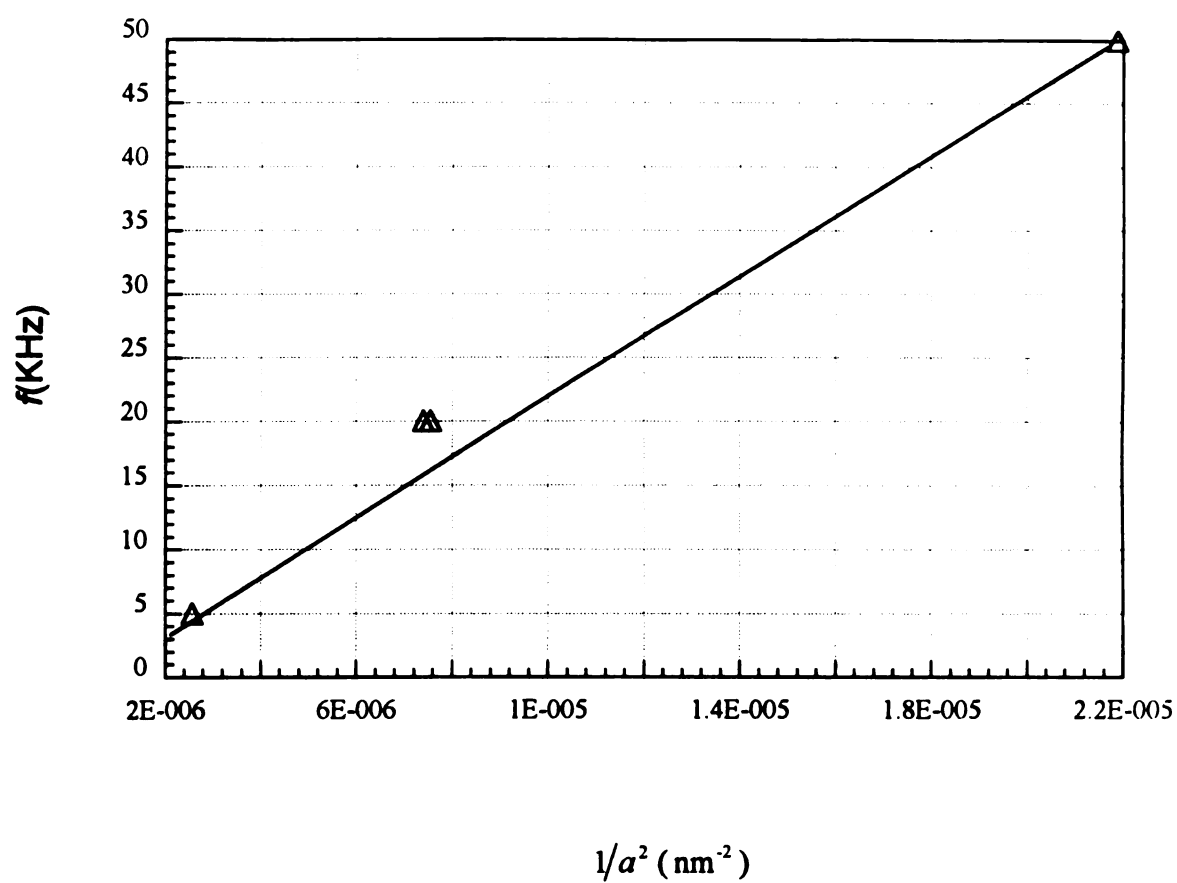


Fig.5.34: The characteristic frequencies vs. reciprocals of the square of the particle diameter.

Bibliography

1. H.P.Schwan, G.Schwarz, J.Maczuk and H.Pauly, J. Phys. Chem. **66**, 2626(1962)
2. M.M.Springer, A.Korteweg and J. Lyklema, J. Electroanal. Chem. **153**, 55(1983)
3. Kyung-hee Lim and E.I. Franses, J. Colloid Interface Sci. **110**, 201(1986)
4. D.F.Myers and D.A.Saville, J. Colloid Interface Sci. **131**, 448(1989)
5. H. Fricke and H.J.Curtis, J. Phys. Chem. **41**, 729(1937)
6. T.M.Shaw, J. Chem. Phys. **10**, 609(1942)
7. D.R.Day, T.J.Lewis, H.L.Lee and S.D.Senturia, J. Adhesion **18**,73(1985)
8. H.P.Schwan, Z. Naturforsch. **6b**, 121(1951)
9. H.P.Schwan and J.Maczuk, Rev. Sci. Instr. **31**, 50(1960)
10. J.Blom, J. Phys. E. Sci. Instrum. **12**, 889(1979)
11. J.L.Oncley, J.Am. Chem. Soc. **60**, 1115(1938)
12. C.A.Marrese, Anal. Chem. **59**, 217(1987)
13. G.T.D.Shouldice, G.A.Vandezande and A.Rudin, European Polymer Journal(To be published)
14. HP 4192A manual
15. N.C.Lockhart and J.W.Snaith, J.Phys. E. Sci. Instrum.1011(1978)
16. F. Van Der Touw, M.Mandel, D.D.Honijk and H.G.F.Verhoog, Trans. Faraday Soc. **67**, 1336(1971)
17. F.Van Der Touw and M.Mandel, Trans. Faraday Soc. **67**, 1343(1971)

Chapter 6

Summary

6.1 Capacitance and dielectric breakdown

From the experiments on paraffin wax discs containing metal particles we have deduced the following.

First, the capacitances were measured by the cell with guard ring arrangement for the sample of stainless steel and copper particles embedded in paraffin wax. For stainless steel inclusions the critical behavior was not consistent with the theoretical prediction due to their poor conductivity. On the other hand the random packing point is similar to other results. To better test the theory we need a particle with very good conductivity, uniformity in shape and ease in handling. For better conductivity we chose copper particles. For these the critical behavior was much closer to the theoretical prediction than stainless steel samples. But the critical point occurred at a much lower concentration than the random close packing point due to their irregularity in shape. The critical exponent α 's in Eq.(1.3.3) were -0.15 for stainless steel and -0.86 for copper. For a perfect conducting spherical particle it should be -1. Even though the copper is a good conductor it is very difficult to handle because it is easily oxidized.

Second, the dielectric breakdown field was determined with the samples containing stainless steel particles. The effect of conducting inclusions was enormous. The dielectric breakdown field was dramatically lowered very much even at very small particle concentrations. The behavior at low loading limit is qualitatively similar to the theoretical

prediction. The dilute limit exponent $\alpha=3/2$ was found in both experiment and numerical simulation for relatively small sample size. It is higher than the analytic prediction $1/2 < \alpha < 1$.

The difference between the behaviors of capacitance and dielectric breakdown field stems from their relationship to the local field distribution. The capacitance is related to the low moment of the local field distribution while the dielectric breakdown field is related to the extreme moment. Hence the capacitance cannot be a non-destructive probe of dielectric breakdown fields.

Since the dielectric breakdown field is related to the extreme moment of the local field distribution it does not obey the central limit theorem. The dielectric breakdown field statistics are described by the extreme distribution. We have compared the Weibull distribution and the modified Gumbel distribution with failure tests of 300 pure paraffin wax discs. It turned out that the modified Gumbel form is more appropriate than the conventional Weibull form.

6.2 Dielectric properties of polystyrene latex suspensions

We attempted to measure the dielectric properties of suspensions of polystyrene spheres. This we hoped was a simple system which would lead the way into more complex systems such as clay suspensions. The subject is of intrinsic interest and we anticipated comparing the results with the theory of Sen and Chew, as well as studying the effects of different surface groups on the polystyrene spheres.

The motivation was good, the extreme difficulties of the experiment were not anticipated. The foremost initial problem was that of electrode polarization which gives large effects in the area of interest. Traditional methods of reducing the electrode polarization or correcting for its presence did not lead to satisfactory results.

We first attempted the measurement of the capacitance of a colloidal suspension using the long cylindrical cell with Pt and Pt black electrodes similar to that used by Schwan et al. There were two major problems to get the correct sample data.

First, the analysis method was not good enough to get rid of the stray field effect which is unavoidable on using a long electrode separation. The subtraction of stray field effects did not result in the anticipated a single value at high frequencies above 100 KHz. At low frequencies below 1 KHz stray field effects were swamped by electrode polarization effects so that the stray field compensation could not be applied. On the other hand in the mid frequency range between 1 KHz and 100 KHz compensation for stray field could be made, but there were not enough data to extrapolate the electrode polarization effect.

Second, using the platinum black electrode for ostensibly reducing the electrode polarization effect caused a Maxwell-Wagner polarization effect. This additional term is dependent on the electrode separation, and therefore complicated the separation of electrode polarization from the apparent dielectric constant.

Due to these difficulties we decided to use a cell with small separation and with a guard ring setup. In this manner we could reduce the stray field effect. Bare Pt, Pt black and sand-blasted Pt electrodes were used. Again using a Pt black electrode produced a Maxwell-Wagner effect. A sand-blasted electrode was not a good substitute for Pt black electrode. Both electrodes are known as methods to reduce the electrode polarization effect but for us they were worse than Pt electrodes. Myers[1] pointed out that both electrodes are used to increase the electrode surface area and as a result the electrode impedance is decreased. He also said that these electrodes are difficult to characterize and it is impossible to predict in advance the electrode impedance which will result from their use.

With the small cell the major problem investigating the dielectric properties of colloidal suspensions is the electrode polarization. The second is the conductivity drift which has

reported by previous investigators to arise from a temperature change or a coagulation of the particles. We found that temperature effects were minimal, and the main time change arose from electrophoresis and coagulation. In the literature only the conductivity drift has been reported but we found that the capacitance also changed with time at low frequencies below 0.1 KHz.

We had four suspension samples which have 4 vol% solid with different surface charge densities. A conductometric titration was used to measure the surface charge density. Their surface charge densities were 3.34, 3.61, 4.01, and 1.03 in $\mu C/cm^2$ for 213.8nm, 364.1nm, 367.7nm and 624.3nm suspensions, respectively.

The experimental data using Pt electrode were presented and compared with the theory developed by Sen and Chew. There were still a big electrode polarization effects in the experimental data below 1 KHz. The imaginary parts were very similar to each other. The characteristic frequencies obeyed the relationship predicted by the theory, i.e., they were proportional to the inverse square of the size of particles.

6.3 Recommendations

(a) Our results for the capacitance of metallic balls in a dielectric indicate that we need a good conductor which has good sphericity and does not easily oxidize. Spherical silver balls should be better. These were not available commercially at the time but they can be produced[2]. The frequency dependence of such a dielectric material is unexpected and should be the subject of theoretical study.

(b) In the breakdown experiment the low loading limit exponent was not consistent with the analytical result probably due to finite size effect. To examine the sample size effect, various sample thickness could be used.

(c) Before we can pursue the study of dielectric properties of colloidal suspensions, the problems with electrode polarization effects at low frequencies below 1 KHz have to be

overcome. The best candidate at this time is the improvement of the four probe method used by Myers and Saville[1]. In this method current is supplied by 2 electrodes and the voltage between two separate electrodes is measured. They assume that, provided the voltage measuring device has a high input impedance, the data derived from the voltage measuring probes should be independent of electrode polarization effects. While we attempted this method, it became clear that the available equipment was not appropriate for this type of measurement. After electrode polarization is satisfactorily dealt with, the next priority is to study the time variation in detail.

Thereafter there are many interesting properties to be studied. The diversity in the published results indicates that they are strongly dependent on the parameters of the particle such as diameter, surface group, charge density and debris from the polymerization process. A complete study could be more satisfactorily attained if the samples were prepared in the premises.

Bibliography

1. D.F.Myers, Ph.D. thesis. Princeton University(1988)
2. D.M.Grannan, J.C.Garland and D.B.Tanner, Phys. Rev. Lett. **46**, 375(1981)

Appendix 1

Derivation of Eqs.(2.2.1) and (2.2.2)

In two dimensions, consider a thin ellipse with its long axis parallel to the direction of the electric field. In elliptic coordinates, ξ, η ,

$$x = c \sinh \xi \sin \eta, \quad z = c \cosh \xi \cos \eta \quad (\text{A1.1})$$

with the ellipse equation being

$$\frac{x^2}{b^2} + \frac{z^2}{a^2} = 1 \quad (\text{A1.2})$$

and

$$c^2 = a^2 - b^2.$$

The electric field applied in the z direction has amplitude E_0 far from the ellipse.

Laplace's equation is then

$$\nabla^2 \Psi = \tau^2 \left(\frac{\partial^2 \Psi}{\partial \xi^2} + \frac{\partial^2 \Psi}{\partial \eta^2} \right) = 0 \quad (\text{A1.3})$$

where $\tau = c(\sinh^2 \xi + \sin^2 \eta)^{1/2}$. This equation has elementary solutions like

$\xi, \eta, e^{\pm \xi} \cos \eta, \cosh(n\xi) \sin(n\eta)$ etc. Applying our boundary conditions which are

$$\Psi = 0 \text{ for } \xi = \xi_0 \quad (\text{A1.4a})$$

$$\Psi \rightarrow -E_0 z = -E_0 c \cosh \xi \cos \eta \text{ for } \xi \rightarrow \infty \quad (\text{A1.4b})$$

yields the electric potentials,

$$\Psi_{in} = 0 \quad (\text{A1.5a})$$

$$\Psi_{out} = -E_0 c \cosh \xi \cos \eta + A e^{-\xi} \cos \eta \quad (\text{A1.5b})$$

where

$$A = \frac{E_o a(a+b)}{c}.$$

To get A we have used $\cosh \xi_0 = a/c$ and $\sinh \xi_0 = b/c$.

The electric fields are then given by

$$\begin{aligned} E_\xi &= -\frac{1}{\tau} \frac{\partial \Psi}{\partial \xi}, \\ E_\eta &= -\frac{1}{\tau} \frac{\partial \Psi}{\partial \eta} \end{aligned} \quad (\text{A1.6})$$

Thus each component of the electric field is

$$E_\xi = -\frac{1}{\tau} \left(-E_o c \sinh \xi \cos \eta - A e^{-\xi} \cos \eta \right), \quad (\text{A1.7a})$$

$$E_\eta = -\frac{1}{\tau} \left(E_o c \cosh \xi \sin \eta - A e^{-\xi} \sin \eta \right). \quad (\text{A1.7b})$$

The electric field along the z -axis can be obtained by setting $\eta=0$.

$$E_z(\xi) = E_o \left[1 + \frac{\cosh \xi_0 e^{\xi_0 - \xi}}{\sinh \xi} \right]. \quad (\text{A1.8})$$

The electric field at the tip of the cluster is found by evaluating Eq. (A1.8) at $\xi = \xi_0$

$$E_{tp} = E_o(1 + a/b) = E_o \left(1 + \sqrt{2} (a/2\kappa)^{1/2} \right) \quad (\text{A1.9})$$

with $\kappa = b^2/a$.

Eq.(A1.8) can be written in terms of r , the distance from the tip,

$$E_z(r) = E_o \left[1 + \frac{a(a+b) \left\{ (a+r) - (r^2 + 2ar + b^2)^{1/2} \right\}}{c^2 (r^2 + 2ar + b^2)^{1/2}} \right] \quad (\text{A1.10})$$

where $r = c \cosh \xi - a$.

When r is large,

$$\begin{aligned} (r+a) / (r^2 + 2ar + b^2)^{1/2} &= (r+a) \left[(r+a)^2 - c^2 \right]^{-1/2} \\ &= 1 + \frac{1}{2} \frac{c^2}{(r+a)^2} - \dots \\ &\approx 1 + \frac{1}{2} \frac{c^2}{r^2} - \dots \end{aligned}$$

Thus $E_z(r)$ asymptotes to a dipole form,

$$E_z(r) = E_o \left(1 + \alpha_{2e}/r^2 \right) \quad (\text{A1.11})$$

with the electric dipole moment

$$\alpha_{2e} = a(a+b)/2. \quad (\text{A1.12})$$

Since the inclusion is sharp, the electric field becomes large near the cluster tip. The nature of this divergence is found from a small $-r$ expansion of Eq. (A1.8) which shows

$$E_z(r) \sim E_{np} \text{ when } r \ll \kappa/2 \quad (\text{A1.13})$$

and

$$E_z(r) \sim E_o \left\{ c_{1e} + c_{2e} (a/2r)^{1/2} \right\} \text{ when } a > r > \kappa/2 \quad (\text{A1.14})$$

with $c_{1e} = 1$ and $c_{2e} = a/(a-b)$. Note that c_{1e} and c_{2e} are $O(1)$ as $a \rightarrow \infty$ and $\kappa \rightarrow \infty$.

In three dimension we can use prolate spheroidal coordinate to get electric field around finger-like inclusion. The coordinate transformations are

$$\begin{aligned} x &= c \sinh \xi \sin \eta \cos \phi \\ y &= c \sinh \xi \sin \eta \sin \phi \\ z &= c \cosh \xi \cos \eta \end{aligned} \quad (\text{A1.15})$$

and the spheroid equation being

$$\frac{x^2}{b^2} + \frac{y^2}{b^2} + \frac{z^2}{a^2} = 1 \text{ and } c^2 = a^2 - b^2. \quad (\text{A1.16})$$

Laplace's equation is then

$$\begin{aligned} \nabla^2 \Psi &= \frac{1}{c^2 (\sinh^2 \xi + \sin^2 \eta) \sinh \xi} \frac{\partial}{\partial \xi} \left(\sinh \xi \frac{\partial \Psi}{\partial \xi} \right) + \frac{1}{c^2 (\sinh^2 \xi + \sin^2 \eta) \sin \eta} \frac{\partial}{\partial \eta} \left(\sin \eta \frac{\partial \Psi}{\partial \eta} \right) \\ &+ \frac{1}{c^2 \sinh^2 \xi \sin^2 \eta} \frac{\partial^2 \Psi}{\partial \phi^2} = 0. \end{aligned} \quad (\text{A1.17})$$

The separated equations, for $\Psi = X(\xi)H(\eta)\Phi(\phi)$, are

$$\begin{aligned} \frac{d^2 \Phi}{d\phi^2} &= -m^2 \Phi, \\ \frac{1}{\sin \eta} \frac{d}{d\eta} \left(\sin \eta \frac{dH}{d\eta} \right) + n(n+1)H - \frac{m^2}{\sin^2 \eta} H &= 0, \\ \frac{1}{\sinh \xi} \frac{d}{d\xi} \left(\sinh \xi \frac{dX}{d\xi} \right) - n(n+1)X - \frac{m^2}{\sinh^2 \xi} X &= 0, \end{aligned} \quad (\text{A1.18})$$

where m, n are zero or positive integer. The solutions of the first equation are $\cos(m\phi)$ and $\sin(m\phi)$. The second and third equations can be rewritten by

$$\frac{d}{dv} \left[(1-v^2) \frac{dH}{dv} \right] + n(n+1)H - \frac{m^2}{1-v^2} H = 0, \quad (\text{A1.19a})$$

$$\frac{d}{du} \left[(1-u^2) \frac{dX}{du} \right] + n(n+1)X - \frac{m^2}{1-u^2} X = 0. \quad (\text{A1.19b})$$

We have changed variables by introducing $u = \cosh \xi$ and $v = \cos \eta$. These equations are those solved by the spherical harmonics P_n^m and their second solutions Q_n^m . Thus the potential Ψ may be written by

$$\Psi(\xi, \eta, \phi) = \sum_{m,n} X_{mn}(\xi) H_{mn}(\eta) \Phi_m(\phi) \quad (\text{A1.20})$$

where

$$X_{mn}(\xi) = AP_n^m(\xi) + BQ_n^m(\xi)$$

$$H_{mn}(\eta) = A'P_n^m(\eta) + B'Q_n^m(\eta)$$

$$\Phi_m(\phi) = C \cos m\phi + D \sin m\phi.$$

For a conducting prolate spheroid, we set $m=0$ by azimuthal symmetry. The boundary conditions are

$$\Psi = 0 \text{ for } \xi = \xi_0 \text{ (surface of spheroid)} \quad (\text{A1.21a})$$

$$\Psi \rightarrow -E_0 c \cosh \xi \cos \eta \text{ for } \xi \rightarrow \infty \quad (\text{A1.21b})$$

which leads to the electric potentials

$$\Psi_{in} = 0 \quad (\text{A1.22a})$$

$$\Psi_{out} = -cE_0 \cosh \xi \cos \eta \left[1 - \left\{ \ln(\tanh(\xi/2)) + 1/\cosh \xi \right\} / B \right] \quad (\text{A1.22b})$$

where

$$\begin{aligned} B &= \ln[\tanh(\xi_0/2)] + 1/\cosh \xi_0 \\ &= \ln\left(\frac{b}{c+a}\right) + \frac{c}{a}. \end{aligned} \quad (\text{A1.23})$$

The electric fields are

$$E_{\xi} = \frac{E_o \cos \eta}{(\sinh^2 \xi + \sin^2 \eta)^{1/2}} \left[\sinh \xi - \left\{ \sinh \xi \ln [\tanh(\xi/2)] + \tanh \xi + \frac{1}{\cosh \xi \sinh \xi} \right\} / B \right]$$

$$E_{\eta} = \frac{E_o \cosh \xi \sin \eta}{(\sinh^2 \xi + \sin^2 \eta)^{1/2}} \left[1 - \left\{ \ln [\tanh(\xi/2)] + 1/\cosh \xi \right\} / B \right]. \quad (\text{A1.24})$$

The electric field in the z-direction(setting $\eta=0$) as a function of distance from the defect tip is then

$$E_z(\xi) = E_o - E_o \left\{ \ln [\tanh(\xi/2)] + \cosh \xi / \sinh^2 \xi \right\} / B \quad (\text{A1.25})$$

We may write this equation in terms of r , the distance from the defect tip.

$$E_z(r) = E_o - E_o \left\{ \ln \left[\frac{r+a-c}{r+a+c} \right]^{1/2} + \frac{c(r+a)}{r^2 + 2ra + b^2} \right\} / B. \quad (\text{A1.26})$$

From the Eq.(A1.25) the electric field at the defect tip is

$$E_{np} = E_o \left\{ 1 - \left(\ln [b/(c+a)] + ca/b^2 \right) / B \right\}. \quad (\text{A1.27})$$

For large a and small b

$$E_{np} \sim E_o \left\{ 1 + a^2 / [b^2 \ln(2a/b)] \right\}. \quad (\text{A1.28})$$

The far-field(large r) solution again has a dipole form

$$E_z(r) \sim E_o + \alpha_{3d} / r^3 \quad (\text{A1.29})$$

where the 3D electric dipole moment

$$\alpha_{3d} = 2c^3/3B. \quad (\text{A1.30})$$

For $\kappa < r < a$, the electric field reduces to

$$E_z(r) \sim E_o \left\{ 1 + [\ln(r/2a) + a/2r] / B \right\} \quad (\text{A1.31})$$

and for $r < \kappa$,

$$E_z(r) \sim E_{np}. \quad (\text{A1.32})$$

Appendix 2

Derivation of Equations in Section 4.4

The potential in the electrolyte solution surrounding a colloid particle is governed by the Poisson-Boltzmann equation. The interaction between particles can be neglected in the dilute limit of colloid concentration. Thus only single particle is considered and the Poisson equation to be solved is

$$\nabla^2 \Phi = -\frac{1}{\epsilon}(N_+ - N_-), \quad (\text{A2.1})$$

where ϵ is the dielectric constant of the solution, and N_+ and N_- is the charge density in the solution surrounding the sphere.

A2.1 Static case

The electrical potential Φ and the ion density N_{\pm} are related by Boltzmann distribution

$$N_{\pm} = N_0 e^{\mp e\Phi/k_b T}. \quad (\text{A2.2})$$

Here N_0 is the charge density of either + or - ions far away from the particle. k_b is Boltzmann constant. T is a temperature. Combination of Eqs.(A2.1) and (A2.2) gives the Poisson-Boltzmann equation

$$\frac{1}{r^2} \frac{d}{dr} \left(r^2 \frac{d\Psi}{dr} \right) = \frac{1}{\delta^2} \sinh \Psi, \quad (\text{A2.3})$$

where $\delta^2 = \epsilon k_b T / (2e^2 N_0)$ is the screening distance, and Ψ is a dimensionless potential which is defined as $\Psi = e\Phi/k_b T$. The boundary conditions for Eq.(A2.3) are

$$\lim_{r \rightarrow \infty} \Psi = 0$$

and

$$\Psi = \Psi_0 \text{ at } r = a.$$

Here a is the radius of the particle. If we take δ as the thickness of the double layer, we can obtain the solution of Eq.(A2.3) by matched asymptotic expansions. Using perturbation expansion the potential can be expanded

$$\Psi \sim \Psi^{(0)} + \left(\frac{\delta}{a}\right)\Psi^{(1)} + \left(\frac{\delta}{a}\right)^2\Psi^{(2)} + \dots \quad (\text{A2.4})$$

We have taken (δ/a) as the small parameter. Combining Eqs.(A2.3) and (A2.4) we get

$$\begin{aligned} & \frac{1}{r^2} \frac{\partial}{\partial r} r^2 \frac{\partial}{\partial r} \left[\Psi^{(0)} + \left(\frac{\delta}{a}\right)\Psi^{(1)} + \dots \right] \\ &= \frac{1}{\delta^2} \sinh \left[\Psi^{(0)} + \left(\frac{\delta}{a}\right)\Psi^{(1)} + \dots \right] \\ &\sim \frac{1}{\delta^2} \sinh \Psi^{(0)} + \frac{1}{a\delta} \Psi^{(1)} \cosh \Psi^{(0)} + O\left(\left(\frac{\delta}{a}\right)^2\right). \end{aligned} \quad (\text{A2.5})$$

First consider the inner region solution. By a coordinate stretching transformation

$$r = a + x\delta, \quad x\delta \ll a, \quad (\text{A2.6})$$

we can emphasize the double layer zone. The Eq.(A2.5) can then be rewritten by

$$\begin{aligned} & \left(\frac{1}{\delta^2} \frac{d^2}{dx^2} + \frac{2}{(a+x\delta)\delta} \frac{d}{dx} \right) \left[\Psi_{inn}^{(0)} + \left(\frac{\delta}{a}\right)\Psi_{inn}^{(1)} + \dots \right] \\ &\sim \frac{1}{\delta^2} \sinh \Psi_{inn}^{(0)} + \frac{1}{a\delta} \Psi_{inn}^{(1)} \cosh \Psi_{inn}^{(0)} + O\left(\left(\frac{\delta}{a}\right)^2\right). \end{aligned} \quad (\text{A2.7})$$

Collecting terms of the same power of δ on both sides gives

$$\frac{d^2}{dx^2} \Psi_{inn}^{(0)} = \sinh \Psi_{inn}^{(0)}, \quad (\text{A2.8})$$

$$\frac{d^2}{dx^2} \Psi_{inn}^{(1)} - \Psi_{inn}^{(1)} \cosh \Psi_{inn}^{(0)} = -2 \frac{d}{dx} \Psi_{inn}^{(0)}. \quad (\text{A2.9})$$

The solutions of Eqs.(A2.8) and (A2.9) are given by

$$\Psi_{inn}^{(0)}(x) = 2 \ln \left(\frac{1 + te^{-x}}{1 - te^{-x}} \right), \quad t = \tanh \left(\frac{\Psi_0}{4} \right), \quad (\text{A2.10})$$

$$\Psi_{inn}^{(1)}(x) = \frac{2te^{-x}}{(1-t^2e^{-2x})} \left[t^2(1-e^{-2x}) - 2x \right]. \quad (\text{A2.11})$$

Therefore the potential for inner region up to 1st order is

$$\begin{aligned}
\Psi_{inn}(x) &= \Psi_{inn}^{(0)} + \left(\frac{\delta}{a}\right) \Psi_{inn}^{(1)} \\
&= 2 \ln \left(\frac{1 + te^{-x}}{1 - te^{-x}} \right) + \frac{\delta 2te^{-x}}{a(1 - t^2 e^{-2x})} [t^2(1 - e^{-2x}) - 2x].
\end{aligned} \tag{A2.12}$$

As $x \rightarrow \infty$, Eq.(A2.12) gives

$$\Psi_{inn} \sim 4te^{-x} + \left(\frac{\delta}{a}\right) 2t(t^2 - 2x)e^{-x} + O\left[\left(\frac{\delta}{a}\right)^2\right]. \tag{A2.13}$$

The inner potential decreases exponentially with distance so that it is very small at large distance. Consequently the outer solution can be obtained by linearizing $\sinh \Psi \sim \Psi$. The outer potential is then

$$\Psi_{out}(r) \sim \Psi_{out}^{(0)} + \left(\frac{\delta}{a}\right) \Psi_{out}^{(1)} = \frac{Ae^{-(r-a)/\delta}}{r} + \frac{\delta Be^{-(r-a)/\delta}}{ar}. \tag{A2.14}$$

The above equation can be expressed in terms of inner variable substituting $r = a + \delta x$ so that

$$\Psi_{out} = \frac{A}{a} e^{-x} + \left(\frac{\delta}{a}\right) \left(\frac{A}{a} x e^{-x} + \frac{B}{a} e^{-x} \right) + O\left[\left(\frac{\delta}{a}\right)^2\right]. \tag{A2.15}$$

Comparing this equation with Eq.(A2.14) we get

$$A = 4at \text{ and } B = 2at^3.$$

A2.2 With an external electric field, $E = E_0 e^{-i\omega t}$

When an external electric field is introduced the charge densities and potential are perturbed from the equilibrium values. We can express the total charge densities and potential as

$$N'_\pm = N_\pm + n_\pm, \tag{A2.16a}$$

$$\Psi' = \Psi + \psi. \tag{A2.16b}$$

N_\pm and Ψ are the equilibrium charge densities and potential, and n_\pm and ψ are the perturbed charge densities and potential respectively. Here Ψ 's and ψ are normalized

potentials, related to the actual potential F through $\Psi = (e/k_b T)\Phi$. The total ionic currents are

$$j_{\pm}' = D_{\pm}(-\nabla N_{\pm}' \mp N_{\pm}' \nabla \Psi'). \quad (\text{A2.17})$$

The first term corresponds to diffusion current and the second term corresponds to conduction current. From Eqs. (A2.16) and (A2.17) we obtain

$$j_{\pm} = D_{\pm}(-\nabla n_{\pm} \mp N_{\pm} \nabla \psi \mp n_{\pm} \nabla \Psi) + O(E_0^2). \quad (\text{A2.18})$$

We have assumed that the perturbing electric field is very small so that $\nabla^2 \Psi' = -\frac{N_+' - N_-'}{2N_0\delta^2}$ can be represented by the linear function of E_0 . We have used the

fact that the ionic current is zero in the absence of the external electric field. The current and the electric field are related to each other by the continuity equation, i.e.,

$$\nabla \cdot j_{\pm} = i\omega n_{\pm}. \quad (\text{A2.19})$$

Furthermore the total charge densities, potential, and currents have to satisfy the Poisson's equation, i.e.,

$$\nabla^2 \Psi' = -\frac{N_+' - N_-'}{2N_0\delta^2}, \quad (\text{A2.20})$$

where $\delta = [\varepsilon' k_b T / (e^2 2N_0)]^{1/2}$ is the Debye screening length, ε' the real part of the dielectric constant of the ionic solution and N_0 the equilibrium ionic densities in the absence of the charged particles. From the Eqs. (A2.16), (A2.18), (A2.19) and (A2.20) we obtain

$$\nabla^2 \psi = -\frac{n_+ - n_-}{2N_0\delta^2} \quad (\text{A2.21})$$

and

$$D_{\pm} \nabla \cdot (-\nabla n_{\pm} \mp N_{\pm} \nabla \psi \mp n_{\pm} \nabla \Psi) = i\omega n_{\pm}. \quad (\text{A2.22})$$

The boundary conditions to solve the above two equations are

$$j_{\pm} \cdot \hat{r}|_{r=a} = 0, \quad (\text{A2.23a})$$

$$\psi(a^+) = \psi(a^-) \quad (\text{A2.23b})$$

and

$$\varepsilon' \frac{\partial \psi}{\partial r} \Big|_{a^+} = \varepsilon_p \frac{\partial \psi}{\partial r} \Big|_{a^-}, \quad (\text{A2.23c})$$

where ε' is the dielectric constant of the ionic solution and ε_p that of the insulating particle. The first boundary condition implies that the ions do not penetrate the insulating particle. The second and the third are the continuity of potential and displacement current at the surface of the particle respectively.

To solve the Eqs.(A2.21) and (A2.22) the perturbation method is useful. The unperturbed potential and charge densities and perturbed potential and charge densities can be expanded

$$n_{\pm} = n_{\pm}^{(0)} + \left(\frac{\delta}{a}\right) n_{\pm}^{(1)} + \left(\frac{\delta}{a}\right)^2 n_{\pm}^{(2)} + \dots, \quad (\text{A2.24a})$$

$$\psi = \psi^{(0)} + \left(\frac{\delta}{a}\right) \psi^{(1)} + \left(\frac{\delta}{a}\right)^2 \psi^{(2)} + \dots, \quad (\text{A2.24b})$$

$$N_{\pm} = N_{\pm}^{(0)} + \left(\frac{\delta}{a}\right) N_{\pm}^{(1)} + \left(\frac{\delta}{a}\right)^2 N_{\pm}^{(2)} + \dots, \quad (\text{A2.24c})$$

$$\Psi = \Psi^{(0)} + \left(\frac{\delta}{a}\right) \Psi^{(1)} + \left(\frac{\delta}{a}\right)^2 \Psi^{(2)} + \dots \quad (\text{A2.24d})$$

A2.2.1 Zeroth order solution

To find the inner solution the coordinate stretching transformation is used to emphasize the double layer region, i.e.,

$$x = \frac{(r-a)}{\delta}.$$

The gradient operator and the divergence operator can be represented in terms of the inner variable x as

$$\nabla \sim \hat{x} \frac{1}{\delta} \frac{\partial}{\partial x} + \hat{\theta} \frac{1}{a} \frac{\partial}{\partial \theta} - \frac{\delta x}{a^2} \frac{\partial}{\partial \theta} \quad \text{for } \delta \rightarrow 0, \quad (\text{A2.25})$$

and

$$\nabla \cdot \sim \left(\frac{2}{a} - \frac{2\delta}{a^2} x + \frac{1}{\delta} \frac{\partial}{\partial x} \right) \hat{x} \cdot + \frac{1}{a \sin \theta} \left(1 - \frac{\delta}{a} x \right) \frac{\partial}{\partial \theta} \sin \theta \hat{\theta} \cdot. \quad (\text{A2.26})$$

From Eqs.(A2.18) and (A2.25) we can see

$$j_{\pm} = \left(\frac{\delta}{a}\right)^{-1} j_{\pm}^{(-1)} + j_{\pm}^{(0)} + \left(\frac{\delta}{a}\right) j_{\pm}^{(1)} + \left(\frac{\delta}{a}\right)^2 j_{\pm}^{(2)} + O\left(\frac{\delta^3}{a^3}\right). \quad (\text{A2.27})$$

Since j_{\pm} have to be bounded, as $\delta/a \rightarrow 0$,

$$j_{\pm}^{(-1)}(x) = 0 \text{ for all } x.$$

Using the Eqs.(A2.24) and (A2.25) the Eq.(A2.18) can be expanded

$$\begin{aligned} j_{\pm} = & D \left\{ \frac{1}{\delta} \left[-\frac{\partial n_{\pm}^{(0)}}{\partial x} \mp N_{\pm}^{(0)} \frac{\partial \psi^{(0)}}{\partial x} \mp n_{\pm}^{(0)} \frac{\partial \Psi^{(0)}}{\partial x} \right] \hat{x} \right. \\ & + \frac{1}{a} \left[-\frac{\partial n_{\pm}^{(1)}}{\partial x} \mp N_{\pm}^{(1)} \frac{\partial \psi^{(0)}}{\partial x} \mp N_{\pm}^{(0)} \frac{\partial \psi^{(1)}}{\partial x} \mp n_{\pm}^{(0)} \frac{\partial \Psi^{(1)}}{\partial x} \mp n_{\pm}^{(1)} \frac{\partial \Psi^{(0)}}{\partial x} \right] \hat{x} \\ & + \frac{1}{a} \left[-\frac{\partial n_{\pm}^{(0)}}{\partial \theta} \mp N_{\pm}^{(0)} \frac{\partial \psi^{(0)}}{\partial \theta} \right] \hat{\theta} \\ & + \frac{1}{a} \left(\frac{\delta}{a} \right) \left[\frac{\partial n_{\pm}^{(2)}}{\partial x} \mp N_{\pm}^{(2)} \frac{\partial \psi^{(2)}}{\partial x} \mp n_{\pm}^{(2)} \frac{\partial \Psi^{(2)}}{\partial x} \mp N_{\pm}^{(1)} \frac{\partial \psi^{(1)}}{\partial x} \mp n_{\pm}^{(1)} \frac{\partial \Psi^{(1)}}{\partial x} \mp N_{\pm}^{(2)} \frac{\partial \psi^{(0)}}{\partial x} \mp n_{\pm}^{(1)} \frac{\partial \Psi^{(1)}}{\partial x} \right] \hat{x} \\ & \left. + \frac{1}{a} \left(\frac{\delta}{a} \right) \left[-\frac{\partial n_{\pm}^{(1)}}{\partial \theta} + x \frac{\partial n_{\pm}^{(0)}}{\partial \theta} \mp N_{\pm}^{(0)} \frac{\partial \psi^{(1)}}{\partial \theta} \pm N_{\pm}^{(0)} x \frac{\partial \psi^{(0)}}{\partial \theta} \mp N_{\pm}^{(1)} \frac{\partial \psi^{(0)}}{\partial \theta} \right] \hat{\theta} \right\} + \dots \quad (\text{A2.28}) \end{aligned}$$

We have omitted the derivatives of Ψ 's with respect to θ since Ψ 's are the function of x only. For the simplicity we have set $D_+ = D_-$. Therefore we have

$$j_{\pm}^{(-1)} = \frac{D}{a} \left[-\frac{\partial n_{\pm}^{(0)}}{\partial x} \mp N_{\pm}^{(0)} \frac{\partial \psi^{(0)}}{\partial x} \mp n_{\pm}^{(0)} \frac{\partial \Psi^{(0)}}{\partial x} \right] = 0. \quad (\text{A2.29})$$

The above differential equation can be easily solved by multiplying the integrating factor $e^{\pm \Psi^{(0)}}$ and we get

$$n_{\pm}^{(0)} = \mp N_{\pm}^{(0)} \left(\psi^{(0)} + C_1^{(0)} \mp C_2^{(0)} \right), \quad (\text{A2.30})$$

where $C_1^{(0)}$ and $C_2^{(0)}$ are the integration constants to be determined. In the limit $(\delta/a) \rightarrow 0$ the Laplacian operator can be approximated by

$$\nabla^2 \sim \frac{1}{\delta^2} \frac{\partial^2}{\partial x^2}. \quad (\text{A2.31})$$

Combining the Eqs.(A2.2) and (A2.10) we obtain

$$N_{\pm}^{(0)} = N_0 e^{\mp \Psi^{(0)}} = N_0 \left(\frac{1 \mp t e^{-x}}{1 \pm t e^{-x}} \right)^2, \quad t = \tanh(\Psi_0/4). \quad (\text{A2.32})$$

With the Eqs. (A2.30), (A2.31) and (A2.32) the Poisson's equation(Eq.(A2.21)) becomes

$$\frac{\partial^2}{\partial x^2} \psi^{(0)} = -\frac{1}{2N_0} (n_+^{(0)} - n_-^{(0)})$$

$$= \cosh \Psi^{(0)} (\psi^{(0)} + C_1^{(0)}) + C_2^{(0)} \sinh \Psi^{(0)}. \quad (\text{A2.33})$$

Thus the zeroth order potential in the inner region is

$$\psi^{(0)} = C_3^{(0)} \frac{(1-t^2)e^{-x}}{1-t^2e^{-2x}} + C_1^{(0)} - C_2^{(0)} \frac{t(1+2x)e^{-x}}{1-t^2e^{-2x}}. \quad (\text{A2.34})$$

We have neglected exponentially increasing solutions. Substituting the above equation to Eq. (A2.30) the zeroth order perturbed charge densities are

$$n_{\pm}^{(0)} = \mp N_{\pm}^{(0)} \left[C_3^{(0)} \frac{(1-t^2)e^{-x}}{1-t^2e^{-2x}} - C_2^{(0)} \left(\frac{t(1+2x)e^{-x}}{1-t^2e^{-2x}} \pm 1 \right) \right]. \quad (\text{A2.35})$$

Now we have to find the solutions for outer region of the double layer. The zeroth order solution implies that the surface potential is perfectly screened by the charge cloud around the particle. Thus the particle looks like neutral at outside of the double layer so that the solution of the Poisson's equation in the outer region resembles the solution for a insulating sphere in a external electric field. They are given by

$$\psi_{out}^{(0)} = -e_0 r \cos \theta - \frac{1}{2} e_0 \left(a^3 / r^2 \right) \cos \theta, \quad \delta/a \rightarrow 0. \quad (\text{A2.36})$$

for outside the particle. Here $e_0 = E_0 e / k_b T$. The potential inside the particle is given by

$$\psi_{ins}^{(0)} = -\frac{3}{2} e_0 r \cos \theta. \quad (\text{A2.37})$$

The continuity of displacement current at the surface of the particle implies that

$$\epsilon_p \left(-\frac{3}{2} e_0 \right) \cos \theta = \epsilon' \frac{1}{\delta} \frac{\partial}{\partial x} \psi^{(0)} \Big|_{x=0}. \quad (\text{A2.38})$$

In the limit $\delta \rightarrow 0$ the above equation cannot be satisfied. Hence

$$\frac{\partial}{\partial x} \psi^{(0)} \Big|_{x=0} = 0, \quad \delta \rightarrow 0. \quad (\text{A2.39})$$

or

$$-C_3^{(0)} \left(\frac{1+t^2}{1-t^2} \right) - C_2^{(0)} \frac{t(1-3t^2)}{(1-t^2)^2} = 0. \quad (\text{A2.40})$$

To get the expression for $n_{\pm}^{(0)}$ and $\psi^{(0)}$ in the outer region we have to solve the Eqs. (A2.21) and (A2.22). Outside of the particle the potential is exponentially small so that we can approximate

$N_{\pm} \sim N_0 + \text{est}$, $\Psi \sim \text{est}$ for $r - a \gg \delta$,

where est stands for exponentially small term of order $\exp[-(r-a)/\delta]$. Now the

Eqs.(A2.21) and (A2.22) can be written by

$$\nabla^2 \psi^{(0)} = -\frac{n_+^{(0)} - n_-^{(0)}}{2N_0\delta^2} \quad (\text{A2.41})$$

and

$$D\nabla \cdot (-\nabla n_{\pm}^{(0)} \mp N_0 \nabla \psi^{(0)}) = i\omega n_{\pm}. \quad (\text{A2.42})$$

Combining two equations we get

$$\nabla^2 n_{\pm}^{(0)} + (i\omega/D)n_{\pm}^{(0)} \mp (1/2\delta^2)[n_+^{(0)} - n_-^{(0)}] = 0. \quad (\text{A2.43})$$

Taking sums and differences of the above equations gives

$$\nabla^2 (n_+^{(0)} + n_-^{(0)}) + (i\omega/D)(n_+^{(0)} + n_-^{(0)}) = 0 \quad (\text{A2.44})$$

and

$$\nabla^2 (n_+^{(0)} - n_-^{(0)}) + (i\omega/D)(n_+^{(0)} - n_-^{(0)}) + (1/\delta^2)[n_+^{(0)} - n_-^{(0)}] = 0. \quad (\text{A2.45})$$

Finally we have

$$n_{\pm}^{(0)} = N_0 \hat{C}_2^{(0)} \frac{a^3 e^{-\lambda(r-a)}}{r^2} \left(\frac{1+\lambda r}{1+\lambda a} \right) \cos\theta, \quad (\text{A2.46})$$

where $\lambda = (1-i)\sqrt{\omega/2D}$. By the matching criterion

$$\lim_{r \rightarrow a} n_{\pm out}^{(0)} \sim \lim_{x \rightarrow \infty} n_{\pm inn}^{(0)},$$

we get

$$N_0 \hat{C}_2^{(0)} a \cos\theta = N_0 C_2^{(0)}. \quad (\text{A2.47})$$

By applying the matching criterion on the potentials we have

$$C_1^{(0)} = -\frac{1}{2} e_0 a \cos\theta. \quad (\text{A2.48})$$

In terms of perturbation expansions the continuity equation in the inner region can be rewritten by

$$\nabla \cdot j_{\pm} = \frac{1}{\delta} \frac{\partial j_{\pm x}^{(0)}}{\partial x} + \left\{ \left(\frac{1}{a} \frac{\partial j_{\pm x}^{(1)}}{\partial x} + \frac{2}{a} j_{\pm x}^{(0)} \right) + \frac{1}{a \sin\theta} \frac{\partial}{\partial \theta} (j_{\pm \theta}^{(0)} \sin\theta) \right\}$$

$$\begin{aligned}
& + \left(\frac{\delta}{a} \right) \left\{ \left(\frac{1}{a} \frac{\partial j_{\pm x}^{(2)}}{\partial x} + \frac{2}{a} j_{\pm x}^{(1)} - \frac{2x}{a} j_{\pm x}^{(0)} \right) + \frac{1}{a \sin \theta} \frac{\partial}{\partial \theta} \left[\left(j_{\pm \theta}^{(1)} + x j_{\pm \theta}^{(0)} \right) \sin \theta \right] \right\} + \dots \\
& = i\omega \left[n_{\pm}^{(0)} + \left(\frac{\delta}{a} \right) n_{\pm}^{(1)} + \left(\frac{\delta}{a} \right)^2 n_{\pm}^{(2)} \dots \right].
\end{aligned} \tag{A2.49}$$

From the above equation

$$\frac{\partial}{\partial x} j_{\pm x}^{(0)} = 0. \tag{A2.50}$$

And the boundary condition Eq.(A2.23a) at the surface of the insulating particle implies that

$$j_{\pm x}^{(0)}(x=0) = 0. \tag{A2.51}$$

Therefore $j_{\pm x}^{(0)}(x) = 0$ for all x . In the outer region the current due to $n_{\pm}^{(0)}$ and $\psi^{(0)}$ is

$$\begin{aligned}
j_{\pm}^{(0)} & \sim D \left(-\nabla n_{\pm}^{(0)} \mp N_{\pm}^{(0)} \psi^{(0)} \mp n_{\pm}^{(0)} \nabla \Psi^{(0)} \right) \\
& \sim D \left(-\nabla n_{\pm}^{(0)} \mp N_0 \nabla \Psi^{(0)} \right).
\end{aligned} \tag{A2.52}$$

With Eqs. (A2.36) and (A2.46) the radial current of the outer region is

$$j_{\pm r}^{(0)} = DN_0 \cos \theta \left\{ \hat{C}_2^{(0)} \frac{a^3 e^{-\lambda(r-a)}}{r^3} \frac{2 + 2\lambda r + \lambda^2 r^2}{1 + \lambda r} \mp \left(\frac{a^3}{r^3} - e_0 \right) \right\}. \tag{A2.53}$$

By the matching criterion

$$\lim_{r \rightarrow a} j_{\pm r}^{(0)} \sim j_{\pm x}^{(0)} = 0,$$

i.e.,

$$\lim_{r \rightarrow a} j_{\pm r}^{(0)} \sim DN_0 \cos \theta \hat{C}_2^{(0)} \alpha = 0, \tag{A2.54}$$

where

$$\alpha = \frac{1 + \lambda a + \lambda^2 a^2}{1 + \lambda a}.$$

Hence $\hat{C}_2^{(0)} = 0$. Consequently we can show $C_2^{(0)} = 0$ and $C_3^{(0)} = 0$ from Eqs.(A2.40) and (A2.47). It is worth while to get the solution of the tangential current in the double layer for the future. From Eq.(A2.28) the tangential component of the inner current of the zeroth order of (δ/a) is

$$j_{\pm \theta}^{(0)} = \mp DN_{\pm}^{(0)} \frac{\partial \psi^{(0)}}{\partial \theta}$$

$$= \mp DN_{\pm}^{(0)} \frac{1}{2} e_0 \sin \theta. \quad (\text{A2.55})$$

The zeroth order solutions are summarized below.

In the inner region

$$\psi_{inn}^{(0)} = -\frac{1}{2} e_0 a \cos \theta, \quad (\text{A2.56a})$$

$$n_{\pm inn}^{(0)} = 0, \quad (\text{A2.56b})$$

$$j_{\pm inn}^{(0)} = \mp \hat{\theta} DN_{\pm}^{(0)} \frac{1}{2} e_0 \sin \theta. \quad (\text{A2.56c})$$

In the outer region

$$\psi_{out}^{(0)} = -e_0 r \cos \theta - \frac{1}{2} e_0 (a^3 / r^2) \cos \theta, \quad (\text{A2.57a})$$

$$n_{\pm out}^{(0)} = 0, \quad (\text{A2.57b})$$

$$j_{\pm r}^{(0)} = \mp DN_0 \cos \theta \left(\frac{a^3}{r^3} - 1 \right) e_0. \quad (\text{A2.57c})$$

A2.2.2 First order solution

From Eq.(A2.28)

$$j_{\pm}^{(0)}(x) = \frac{D}{a} \left[-\frac{\partial}{\partial x} n_{\pm}^{(1)} \mp \left(N_{\pm}^{(0)} \frac{\partial}{\partial x} \psi^{(1)} + n_{\pm}^{(1)} \frac{\partial}{\partial x} \Psi^{(0)} \right) \right] = 0. \quad (\text{A2.58})$$

Multiplying it by the integrating factor $e^{\pm \Psi^{(0)}}$ we obtain

$$n_{\pm}^{(1)} = \mp N_{\pm}^{(0)} \left(\psi^{(0)} + C_1^{(1)} \mp C_2^{(1)} \right). \quad (\text{A2.59})$$

Furthermore the potential has to satisfy Poisson's equation, i.e.,

$$\frac{\partial^2}{\partial x^2} \psi^{(1)} = -\frac{1}{2N_0} \left[n_+^{(1)} - n_-^{(1)} \right]. \quad (\text{A2.60})$$

With Eq.(A2.59) we get

$$\frac{\partial^2}{\partial x^2} \psi^{(1)} = \cosh \Psi^{(0)} \left(\psi^{(1)} + C_1^{(1)} \right) + C_2^{(1)} \sinh \Psi^{(0)}. \quad (\text{A2.61})$$

The above equation is identical to Eq.(A2.33). Thus the solutions resemble Eqs.(A2.34)

so that

$$\psi^{(1)} = \left[C_3^{(1)} \frac{(1-t^2)e^{-x}}{1-t^2e^{-2x}} + C_1^{(1)} - C_2^{(1)} \frac{t(1-2x)e^{-x}}{1-t^2e^{-2x}} \right] a \cos \theta, \quad (\text{A2.62})$$

$$n_{\pm}^{(1)} = \mp N_{\pm}^{(0)} \left[C_3^{(1)} \frac{(1-t^2)e^{-x}}{1-t^2e^{-2x}} - C_2^{(1)} \left(\frac{t(1+2x)e^{-x}}{1-t^2e^{-2x}} \pm 1 \right) \right] a \cos \theta. \quad (\text{A2.63})$$

From Eq.(A2.49)

$$\frac{\partial}{\partial x} j_{\pm x}^{(1)} + \frac{1}{\sin \theta} \frac{\partial}{\partial \theta} (\sin \theta j_{\pm \theta}^{(0)}) = 0. \quad (\text{A2.64})$$

Substituting $j_{\pm \theta}^{(0)}$ given by the Eq.(A2.55) and solving the differential equation the first order radial current is

$$j_{\pm x}^{(1)} = \pm 3e_0 DN_0 \cos \theta \left(x \mp \frac{2t}{1 \pm t} \pm \frac{4te^{-x}}{1 \pm te^{-x}} \right) \quad (\text{A2.65a})$$

$$\sim \pm 3e_0 DN_0 \cos \theta \left[x \mp \frac{2t}{1 \pm t} \right], \quad x \rightarrow \infty. \quad (\text{A2.67b})$$

From the continuity equation

$$\nabla^2 n_{\pm}^{(1)} + (i\omega D) n_{\pm}^{(1)} \mp \left(\frac{1}{\delta} \right) [n_{+}^{(1)} - n_{-}^{(1)}] = 0. \quad (\text{A2.68})$$

This equation is identical to (A2.43) so that the solution is

$$n_{\pm}^{(1)} = N_0 C^{(1)} \frac{a^3 e^{-\lambda(r-a)}}{r^2} \frac{1 + \lambda r}{1 + \lambda a} \cos \theta. \quad (\text{A2.69})$$

This result indicate that the diffusion cloud is neutral and has a size $\sim 1/\lambda$. Therefore the

Eq.(A2.41) become

$$\nabla^2 \psi^{(1)} = 0, \quad (\text{A2.70})$$

and gives the solution

$$\psi^{(1)} = P^{(1)} e_0 \left(\frac{a^3}{r^2} \right) \cos \theta. \quad (\text{A2.71})$$

The radial current in the outer region is

$$\begin{aligned} j_{\pm r}^{(1)} &= D \left(-\nabla n_{\pm}^{(1)} \mp N_0 \nabla \psi^{(1)} \right) \\ &= DN_0 \cos \theta \left[C^{(1)} \frac{a^3 e^{-\lambda(r-a)}}{r^3} \frac{1 + \lambda r + \lambda^2 r^2}{1 + \lambda a} \pm \frac{2P^{(1)} e_0 a^3}{r^3} \right]. \end{aligned} \quad (\text{A2.72})$$

Therefore the outer normal currents are

$$\begin{aligned} j_{\pm r} &\sim j_{\pm r}^{(0)} + \left(\frac{\delta}{a} \right) j_{\pm r}^{(1)} \\ &= \pm DN_0 \cos \theta \left(-\frac{e_0 a^3}{r^3} + e_0 \right) \end{aligned}$$

$$+\left(\frac{\delta}{a}\right)DN_0\cos\theta\left[C^{(1)}\frac{a^3e^{-\lambda(r-a)}}{r^3}\frac{1+\lambda r+\lambda^2r^2}{1+\lambda r}\pm\frac{2P^{(1)}e_0a^3}{r^3}\right]. \quad (\text{A2.73})$$

In the inner region $r-a \sim \delta x$, Eq.(A2.73) in terms of inner variable can be rewritten by $j_{\pm r} \sim \pm DN_0 \cos\theta [3e_0x \pm 2C^{(1)}\alpha + 2P^{(1)}e_0]$, $r \rightarrow a$. (A2.74)

Comparing the Eqs. (A2.67b) and (A2.74) we get

$$P^{(1)} = \frac{6t^2}{1-t^2}, \quad C^{(1)} = -\frac{6e_0t}{(1-t^2)\alpha}. \quad (\text{A2.75})$$

The potential in the outer region is

$$\psi \sim \psi^{(0)} + \left(\frac{\delta}{a}\right)\psi^{(1)} = -e_0r\cos\theta + \frac{e_0a^3\cos\theta}{r^2}\left[-\frac{1}{2} + \frac{6t^2}{1-t^2}\left(\frac{\delta}{a}\right)\right]. \quad (\text{A2.76})$$

In the limit $r \rightarrow a$, Eqs.(A2.69) and (A2.76) which are the outer solutions can be written by

$$n_{\pm out} \sim (\delta/a)n_{\pm out}^{(1)} \sim \delta N_0 C^{(1)} \cos\theta, \quad (\text{A2.77})$$

$$\psi_{out} \sim \psi_{out}^{(0)} + (\delta/a)\psi_{out}^{(1)} \sim \left[-\frac{3}{2}e_0 + (\delta/a)P^{(1)}e_0\right]a\cos\theta. \quad (\text{A2.78})$$

In the limit $x \rightarrow \infty$, the inner solutions given by Eqs.(A2.62) and (A2.63) become

$$\psi_{inn}^{(1)} \sim C_1^{(1)}a\cos\theta, \quad (\text{A2.79})$$

$$n_{\pm inn}^{(1)} \sim N_0 C_2^{(1)}a\cos\theta. \quad (\text{A2.80})$$

By the matching criterion we can show that

$$C_1^{(1)} = P^{(1)}e_0 \text{ and } C_2^{(1)} = C^{(1)}. \quad (\text{A2.81})$$

The unknown $C_3^{(1)}$ can be obtained by the boundary condition of the displacement current,

i.e., the continuity of the displacement current at the surface of the particle.

$$-\frac{3}{2}e_0\frac{\epsilon_r}{\epsilon'} = -C_3^{(1)}\frac{1+t^2}{(1-t^2)^2} - C^{(1)}\frac{t(1-3t^2)}{(1-t^2)^2}. \quad (\text{A2.82})$$

The first order solutions are summarized below.

Inner region

$$n_{\pm inn}^{(1)} = \mp N_{\pm}^{(0)}\left[C_3^{(1)}\frac{(1-t^2)e^{-x}}{1-t^2e^{-2x}} - C^{(1)}\left(\frac{t(1+2x)e^{-x}}{1-t^2e^{-2x}} \pm 1\right)\right]a\cos\theta, \quad (\text{A2.83a})$$

$$\psi_{inn}^{(1)} = \left[C_3^{(1)} \frac{(1-t^2)e^{-x}}{1-t^2e^{-2x}} - C^{(1)} \frac{t(1-2x)e^{-x}}{1-t^2e^{-2x}} + P^{(1)}e_0 \right] a \cos\theta, \quad (\text{A2.83b})$$

$$j_{\pm inn}^{(1)} = \pm 3e_0 DN_0 \cos\theta \left(x \mp \frac{2t}{1 \pm t} \pm \frac{4te^{-x}}{1 \pm te^{-x}} \right). \quad (\text{A2.83c})$$

Outer region

$$n_{\pm out}^{(1)} = N_0 C^{(1)} \frac{a^3 e^{-\lambda(r-a)}}{r^3} \frac{1+\lambda r}{1+\lambda a} \cos\theta, \quad (\text{A2.84a})$$

$$\psi_{out}^{(1)} = P^{(1)} e_0 \left(\frac{a^3}{r^2} \right) \cos\theta, \quad (\text{A2.84b})$$

$$j_{\pm out}^{(1)} = DN_0 \cos\theta \left[C^{(1)} \frac{a^3 e^{-\lambda(r-a)}}{r^3} \frac{1+\lambda r + \lambda^2 r^2}{1+\lambda a} \pm \frac{2P^{(1)}e_0 a^3}{r^3} \right]. \quad (\text{A2.84c})$$

$C^{(1)}$, $C_3^{(1)}$ and $P^{(1)}$ are given by Eqs.(A2.75) and (A2.82), respectively.

A2.2.3 Higher order theory

Up to first order solutions the dielectric enhancement does not occur. The first order potential in the outer region obtained from the radial current in the double layer. Similarly $\psi^{(2)}$ can be obtained from $j_{\pm x}^{(2)}$. From Eq.(A2.49) collecting terms of the order of (δ/a)

on both sides gives

$$\frac{1}{a} \frac{\partial}{\partial x} j_{\pm x}^{(2)} = i\omega n_{\pm}^{(1)} - \frac{1}{a \sin\theta} \frac{\partial}{\partial \theta} \sin\theta (j_{\pm \theta}^{(1)} - x j_{\pm \theta}^{(0)}) - \frac{2}{a} j_{\pm x}^{(1)}. \quad (\text{A2.85})$$

$j_{\pm \theta}^{(0)}$ and $j_{\pm x}^{(1)}$ are given in Eqs. (A2.55) and (A2.65a), respectively.

$$j_{\pm \theta}^{(0)} = \mp DN_{\pm}^{(0)} \frac{1}{2} e_0 \sin\theta$$

and

$$j_{\pm x}^{(1)} = \pm 3e_0 DN_0 \cos\theta \left[x \mp \frac{4t}{1 \pm t} \pm \frac{4te^{-x}}{1 \pm te^{-x}} \right].$$

From the continuity equation which is expanded by using perturbation expansions, i.e.,

Eq.(A2.28), the first order tangential current in the double layer is given by

$$j_{\pm \theta}^{(1)} = D \frac{1}{a} \frac{\partial}{\partial \theta} \left\{ -n_{\pm}^{(1)} \mp \left[N_{\pm}^{(1)} \psi^{(0)} + N_{\pm}^{(0)} (\psi^{(1)} - x \psi^{(0)}) \right] \right\}, \quad (\text{A2.86})$$

where

$$N_{\pm}^{(1)} = \mp N_{\pm}^{(0)} \frac{2te^{-x}}{(1-t^2e^{-2x})} \left[t^2(1-e^{-2x}) - 2x \right], \quad (\text{A2.87})$$

$n_{\pm}^{(1)}$, $N_{\pm}^{(0)}$, $\psi^{(0)}$ and $\psi^{(1)}$ are given in Eqs.(A2.83a), (A2.32), (A2.56a) and (A2.83b),

respectively. Thus Eq.(A2.86) can be rewritten by

$$j_{\pm\theta}^{(1)} = DN_{\pm}^{(0)} \sin\theta \left\{ \frac{3}{2}e_0 \frac{2te^{-x}}{1-t^2e^{-2x}} \left[t^2(1-e^{-2x}) - 2x \right] + C^{(1)} \pm P^{(1)} \pm \frac{3}{2}e_0x \right\}. \quad (\text{A2.88})$$

Now $j_{\pm x}^{(2)}$ can be determined from the Eq.(A2.85)

$$\begin{aligned} j_{\pm x}^{(2)} &= i\omega N_0 a \left\{ C^{(1)}x \mp \frac{1}{(1\pm t)^2} \left[C_3^{(1)} + t(1\pm 2t)C^{(1)} \right] \right\} \cos\theta \\ &\mp \frac{DN_0}{a} \cos\theta \left[6e_0x^2 + 2x \left(P^{(1)}e_0 \pm C^{(1)} \mp \frac{12e_0t}{1\pm t} \right) \right. \\ &\quad \left. - 24e_0 \ln(1\pm t) \mp \frac{8t}{1\pm t} \left(P^{(1)}e_0 \pm C^{(1)} \right) \pm 12e_0t \right], \quad x \rightarrow \infty. \end{aligned} \quad (\text{A2.88})$$

The second order potential and charge densities are similar to the first order solutions so that the potential and the charge densities in the outer region up to second order are

$$\begin{aligned} \psi &\sim \psi^{(0)} + \left(\frac{\delta}{a} \right) \psi^{(1)} + \left(\frac{\delta}{a} \right)^2 \psi^{(2)} \\ &= \left[-\frac{r^3}{a^3} - \frac{1}{2} + \frac{\delta}{a} P^{(1)} + \left(\frac{\delta}{a} \right)^2 P^{(2)} \right] \frac{a^3 e_0}{r^2} \cos\theta, \end{aligned} \quad (\text{A2.89})$$

$$\begin{aligned} n_{\pm} &\sim \frac{\delta}{a} n_{\pm}^{(1)} + \left(\frac{\delta}{a} \right)^2 n_{\pm}^{(2)} \\ &= \delta N_0 \frac{a^2 e^{-\lambda(r-a)}}{r^2} \left(\frac{1+\lambda r}{1+\lambda a} \right) \left[C^{(1)} + \frac{\delta}{a} C^{(2)} \right]. \end{aligned} \quad (\text{A2.90})$$

The outer radial currents can be obtained by

$$\begin{aligned} j_{\pm r}^{(2)} &= D \left(-\nabla n_{\pm}^{(2)} \mp N_0 \nabla \psi^{(2)} \right) \\ &= DN_0 \cos\theta \left[C^{(2)} \frac{a^3 e^{-\lambda(r-a)}}{r^3} \frac{1+\lambda r + \lambda^2 r^2}{1+\lambda a} \pm \frac{2P^{(2)}e_0 a^3}{r^3} \right]. \end{aligned} \quad (\text{A2.91})$$

In terms of the inner variable the outer radial currents up to second order are

$$\begin{aligned} j_{\pm r} &\sim DN_0 \cos\theta \left\{ \pm \frac{\delta}{a} \left[3e_0x + 2P^{(1)}e_0 \pm 2C^{(1)}\alpha \right] \right. \\ &\quad \left. \mp \left(\frac{\delta}{a} \right)^2 \left[6e_0x^2 + 6x \left(P^{(1)}e_0 + C^{(1)}\alpha \pm \frac{1}{6}C^{(1)} \frac{\lambda^3 a^3}{1+\lambda a} \right) \right] \right\} \end{aligned}$$

$$-2P^{(2)}e_0 \mp 2C^{(2)}\alpha \Big] \Big\}, r \rightarrow a. \quad (\text{A2.92})$$

The inner radial currents can be obtained from

$$j_{\pm x} \sim \left(\frac{\delta}{a}\right) j_{\pm x}^{(1)} + \left(\frac{\delta}{a}\right)^2 j_{\pm x}^{(2)}, \quad (\text{A2.93})$$

where $j_{\pm x}^{(1)}$ and $j_{\pm x}^{(2)}$ are given by Eqs.(A2.65a) and (A2.88). Comparing Eq.(A2.92) and the result of Eq.(A2.93) we get

$$\begin{aligned} P^{(2)}e_0 \pm C^{(2)}\alpha &= 12e_0 \ln(1 \pm t) \pm \frac{4t}{1 \pm t} [P^{(1)}e_0 \pm C^{(1)}] \mp 6e_0 t \\ &\quad - \frac{i\omega a^2}{2D} \frac{1}{(1 \pm t)^2} [C_3^{(1)} + t(1 \pm 2t)C^{(1)}]. \end{aligned} \quad (\text{A2.94})$$

From the above equation we can determine $P^{(2)}$ and $C^{(2)}$ so that the total induced dipole moment to second order is

$$\begin{aligned} P &\sim -\frac{1}{2} + \left(\frac{\delta}{a}\right) \frac{6t^2}{1-t^2} \\ &\quad + \left(\frac{\delta}{a}\right)^2 \left[-\frac{3}{4} \frac{i\omega}{D} \frac{\epsilon_p}{\epsilon'} a^2 + 6 \ln(1-t^2) - \frac{24t^2}{(1-t^2)^2} \left(t^2 + \frac{1}{\alpha} \right) \right]. \end{aligned} \quad (\text{A2.95})$$

MICHIGAN STATE UNIV. LIBRARIES



31293010468597